Motion Analysis and Control Design of Underactuated Limit Cycle Locomotion Robots Using Indirect Actuation

Longchuan LI

Japan Advanced Institute of Science and Technology

Doctoral Dissertation

Motion Analysis and Control Design of Underactuated Limit Cycle Locomotion Robots Using Indirect Actuation

Longchuan LI

Supervisor: Associate Professor Fumihiko Asano

Graduate School of Advanced Science and Technology
Japan Advanced Institute of Science and Technology
Information Science

June 2019

Abstract

Nowadays, locomotion robots have been considered to play more and more important roles in industrial and agricultural production, disaster rescue, as well as space exploration. Consequently, achieving stable and efficient locomotion on complex terrains becomes the most important property for locomotion robots. Slippery road surface, which induces a changeable grounding point, is one of the most difficult terrains for locomotion robots to overcome. Many remarkable locomotion robots have been proposed and developed to address this issue. Despite the success they achieved, however, the efficiency of their robots are not well guaranteed and they are difficult to be applied to real tasks due to the complicated sensing and control systems. Moreover, most of these robots have to walk very carefully in such a condition.

With the consideration of achieving stable locomotion on slippery ground with natural and simple gait as well as avoiding intricate sensing and control systems, a novel seed-like robot has been proposed and developed recently. Unlike walking robots stepping with legs, this legless robot generates sliding locomotion on slippery downhill by means of body rotation. A substantial advantage of this robot is that it positively utilizes the sliding locomotion, which is generally considered to be harmful to the walking robot. In contrast, a fundamental issue is that such locomotion can only be generated on the slippery downhill.

Towards achieving high-speed and energy-efficient sliding locomotion on the slippery level ground, indirectly controlling mechanism is applied to this robot due to the underactuation at the grounding point. Inspired by the vibration of viscera and carrying loads in biological systems, indirectly controlling mechanism has been proposed based on entrainment effect recently. Instead of manipulating any link of the robot, an active wobbling mass is attached to a limit cycle walker. The wobbling mass is forced to oscillate periodically, the robot locomotion system is, therefore, entrained to it. The implementation of this control method is easy, however, the resultant dynamics is complicated due to the high nonlinearity of it.

To better understand this control method, investigation on nonlinear properties, *e.g.*, entrainment, chaos and hysteresis phenomenon, ought to be performed. Using a combined rimless wheel with an active wobbling mass (CRW) as a simple example, the detailed entrainment properties of such indirectly controlled limit cycle locomotion robots are characterized by Arnold tongue, where the size of it gives the range of entrained locomotion. The entrainability of the wobbling mass, therefore, can be measured by it. To observe various patterns of locomotion, quasi-periodic and chaotic gaits are observed by means of plotting the phase difference between the walker and the wobbling mass in one cycle. The sensitivity to initial conditions is analyzed by means of hysteresis phenomenon. Moreover, the basin of attraction, which estimates the stable range of the dynamics, is used to count the number of initial conditions leading to individual attractor. In view of these investigations, nonlinear properties of this indirectly controlled limit cycle walker are clarified.

To guarantee the rigorousness of this research, experimentally study is necessary to be conducted to verify the overall entrainment effect. An experimental machine is designed and produced to conduct real experiment. A tilted convey belt guarantees long time walking and the wobbling mass is controlled by EPOS2 controller for Maxon motor. The up-and-down oscillation of the wobbling mass is mapped to the rotation of motor by means of a piston crank mechanism. Most importantly, the walking period is obtained between adjacent ground collisions of one walking trial, which is measured via an accelerometer

MPU6050, inspired by the collision equation. Clean-cut Arnold tongue is obtained and the experiment results are highly consistent with numerical simulations.

Since the dynamics of the system is highly nonlinear, the equation of motion of this indirectly controlled limit cycle walker is approximated by a scalar phase equation for pursuing an optimal entrainment waveform to reduce the forcing energy. Here, the "optimal" is defined by maximizing the entrainment range with fixed energy. Since the step length of the rimless wheel is a constant, a larger entrainment range potentially leads to a higher frequency the walker could be entrained to, which consequently results in higher walking speed. To utilize the phase equation, phase response curve, which tabulates the sensitivity of the walker with respect to external disturbances, is numerically obtained by applying slight perturbations at different phases of the whole limit cycle. Afterwards, the cost function is obtained by maximizing the entrainment range with fixed forcing power. By applying calculus of variations on the cost function, the optimal entrainment waveform is analytically derived. As an ecological extension, an example of $m : 1$ entrainment waveform, which means during m cycles walking, the wobbling mass is required to make only one cycle, is numerically obtained. The analytical results are further confirmed by numerical simulations by comparing the sizes of Arnold tongues. The results show that the entrainment ranges are able to be magnified by utilizing a phase sensitive forcing function, where the specific Arnold tongue is able to be maximized accordingly.

Based on the processes above, this indirectly controlling mechanism has been well understood and can be applied to the seed-like robot to generate sliding locomotion on slippery level ground. Rather than serving as a rhythm generator only, the wobbling mass should also be able to generate enough propulsive force at the underactuated grounding point appropriately for inducing high-speed and energy-efficient sliding locomotion on level ground. The original rotatory wobbling mass is removed and an oscillatory wobbling mass is attached to a point away from the center of the body to increase the asymmetry. This indirectly controlled locomotion robot slides backward and/or forward by means of the propulsive force at the grounding point induced by the oscillation of the wobbling mass and the periodicity of the locomotion is guaranteed by the body rotation entrained to the wobbling motion. Stable and efficient sliding locomotion on slippery level ground can be generated by this underactuated robot. Nonlinear analysis shows the dependency of efficiency on the entrainment effect. Moreover, the reason for inducing the entrained, however, inefficient locomotion is analyzed through mechanical energy consumption point of view. The results show that it is due to the unconcentrated sliding direction.

To further enhance the sliding velocity, three aspects are considered: 1. To concentrate the instantaneous sliding direction instead of wandering backward and forward. 2. To strengthen the propulsive force at the grounding point for increasing the sliding distance in one rotation cycle. 3. To maximize the entrainment range with an optimal trajectory for wobbling motion to exclude inefficient locomotion. Therefore, the robot is modified into an arc-shaped base with an elastic body, which is modeled by spring and damper, indirectly controlled by the active wobbling mass. The sliding velocity is dramatically increased benefited from the facts observed from analysis on nonlinear properties and energy consumption: 1. The instantaneous sliding direction is concentrated by damping force, since part of the redundant energy that leads to backward sliding can be consumed by it. 2. The sliding distance in one rotation cycle around the grounding point is increased by the anti-phase oscillation between the wobbling mass and the spring. 3. The entrainment range is enlarged, benefited from the elasticity of the body. In this case, sine wave is the optimal entrainment waveform since the springs oscillation is sinusoidal.

Keywords: Underactuated systems, Limit cycle walking, Entrainment, Stability, Efficiency

Acknowledgments

First and foremost, I would like to express my sincere appreciation to my supervisor Associate Professor Fumihiko Asano, who has set an example of excellence as a researcher and mentor, for guiding and encouraging me over the years. It is a great honor and life-long precious memory for me to join Asano lab and it is my fortune to have the opportunity to be guided and taken good care by Asano sensei. More than a supervisor, he is also a good friend in my daily life, as well as a family member when I feel upset. I believe that my research and life would never go such smooth without his guidance and support.

Besides my supervisor, I would like to express sincere gratitude to Professor Isao Tokuda, who is the supervisor of my minor research. Tokuda sensei taught me the most important keyword "entrainment" in this thesis, and I realize that I am also "entrained" by his kind and patient guidance. Not only my way of scientific thinking, but also my philosophy of life is positively affected by him.

With a special mention to Professor Masato Akagi for taking care of both my master and Ph.D. courses as my second supervisor. Akagi sensei taught me skiing, which becomes my favorite sport, in the first year I went to Japan. I really enjoy communicating and playing with him.

I would also like to thank Professor Kunihiko Hiraishi, Associate Professor Yuji Harata and Assistant Professor Yuta Hanazawa for giving me many important comments and suggestions as my committee members.

In addition, my great appreciation goes to Professor Jianwu Dang and Associate Professor Hirokazu Tanaka for providing me the chance to study in JAIST and taking good care of my master course. Without their support, I may never have the opportunity to meet so nice people and enjoy a research life here.

Meanwhile, I would like to acknowledge Associate Professor Ho Anh-Van, Dr. Xuan Xiao, Dr. Yang Liu, Dr. Shengbei Wang, Dr. Haitao Zhang and Mr. Yanqiu Zheng for their useful discussions and suggestions.

Moreover, I would also like to express my thanks to my lab members, especially Masatsugu Nishihara, Cong Yan, Kota Matsuura and Seiya Kobayashi for experiment assisting, Lin Guo and Hengtong Zhao for illustration supporting.

Furthermore, I would like to thank Xingfeng Li, Yongwei Li, Yawen Xue, Hitoshi Sato, Jiajie Xue, Jinfeng Huang, Minghui Li, Qiukai Qi, Zhaolun Huang and all my other dear friends in JAIST.

Most importantly, I greatly appreciate my grand parents, parents and wife for their understanding, support and inclusiveness.

I dedicate this dissertation to all the people mentioned above, for their unfailing encouragements, support and patience.

Table of Contents

List of Figures

List of Tables

Acronym and Abbreviation

CoM	Center of mass
BOA	Basin of attraction
DOF	Degrees of freedom
CRW	Combined rimless wheel with an active wobbling mass
PRC	Phase response curve

Chapter 1

Introduction

1.1 Background

1.1.1 Underactuated systems

The definition of underactuated system is that the number of degrees of freedom (DOF) is higher than the number of actuators of the system [1]. As shown in Fig. 1.1 (a), the 3-link rigid body is underactuated (3-DOF VS 2 actuators), since joint torque can not be applied at the grounding point. By modifying the point contact into planar contact and fixing it on the ground, the system becomes fully-actuated (3-DOF VS 3 actuators) if slipping between the foot and the ground is successfully avoided, as shown in Fig. 1.1 (b). However, a slight movement at the grounding planar will induce an additional DOF, which makes the system return to underactuated (4-DOF VS 3 actuators), as shown in Fig. 1.1 (c). This phenomenon occurs easily in robot locomotion systems, especially when the contacting terrain is slippery, which makes achieving stable and efficient locomotion difficult. Many remarkable robots have been designed and developed to address this issue with complicated sensing and control systems [2] [3] [4] [5] [6]. In contrast, few of them consider using control methods which take the natural dynamics of the systems into account, *e.g.*, limit cycle walking.

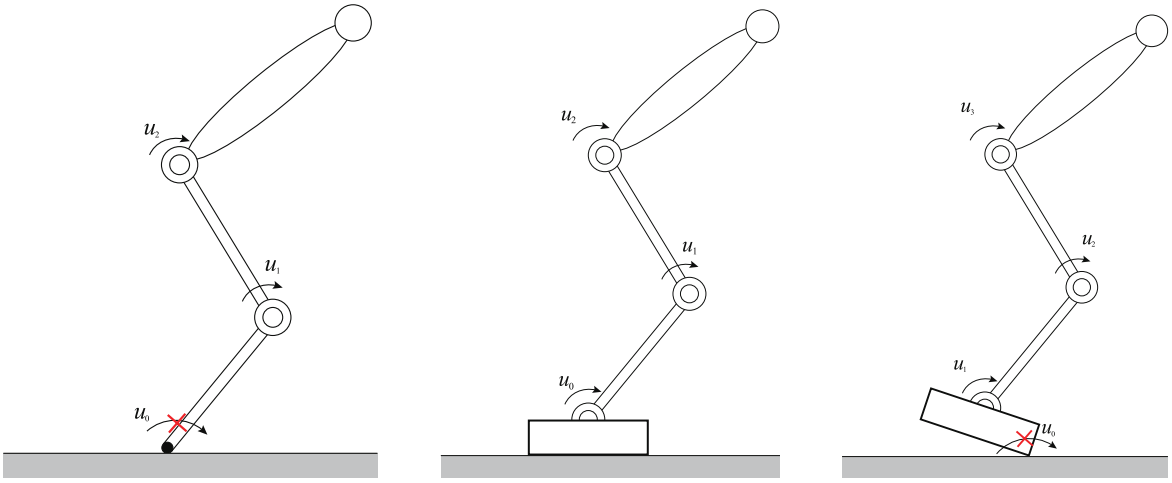

(a) Ground contacting with point foot

(b) Ground contacting with fixed planar foot

(c) Ground contacting with rotating planar foot

Figure 1.1: Underactuation induced by ground contacting

1.1.2 Limit cycle walking

As introduced by one of the greatest mathematicians in the world, Henri Poincaré, a limit cycle is a closed orbit in the phase space of a nonlinear dynamic system [7], which is mathematically represented as differential equations, owning the quality that at least one other orbit spirals into it as shown in Fig. 1.2.

Inspired by the works that the passive walkers naturally converge to periodic trajectories [8], limit cycle walking, which is initiated by Goswami, is widely used in robot locomotion control [9] [10] [11] [12], as well as modeling human walking [13]. Benefited from its inherent periodicity, limit cycle walking has been generally considered to be the most efficient and stablest gait on normal ground. On one hand, dynamic walkers can easily achieve limit cycle walking by adding torque inputs to them in the condition that the grounding point is fixed. On the other hand, the underactuation at the grounding point makes the robot difficult to guarantee stability when it is changeable, *e.g.*, locomotion on slippery ground. Since achieving stable and efficient limit cycle locomotion on the slippery ground is difficult by directly actuating the joint torques, indirectly controlling method is adopted to solve this problem in this research.

1.2 Methodology

1.2.1 Indirectly controlling mechanism

Inspired by the vibration of viscera and carrying loads, which can be widely observed in biological systems [14] [15], a novel and indirectly control method has been proposed by Asano and Tokuda recently [16]. Unlike traditional control methods which rely on manipulating multiple joint torques that potentially increases the complicity of sensing and control system, an active wobbling mass with up-and-down oscillation motion is attached to a passive dynamic walker, *i.e.*, combined rimless wheel with an active wobbling mass (CRW), in this indirectly controlled method as shown in Fig. 1.3. By enabling the wobbling mass to track a periodic trajectory, the dynamics of the walker can be indirectly controlled by oscillating the wobbling mass via the entrainment effect.

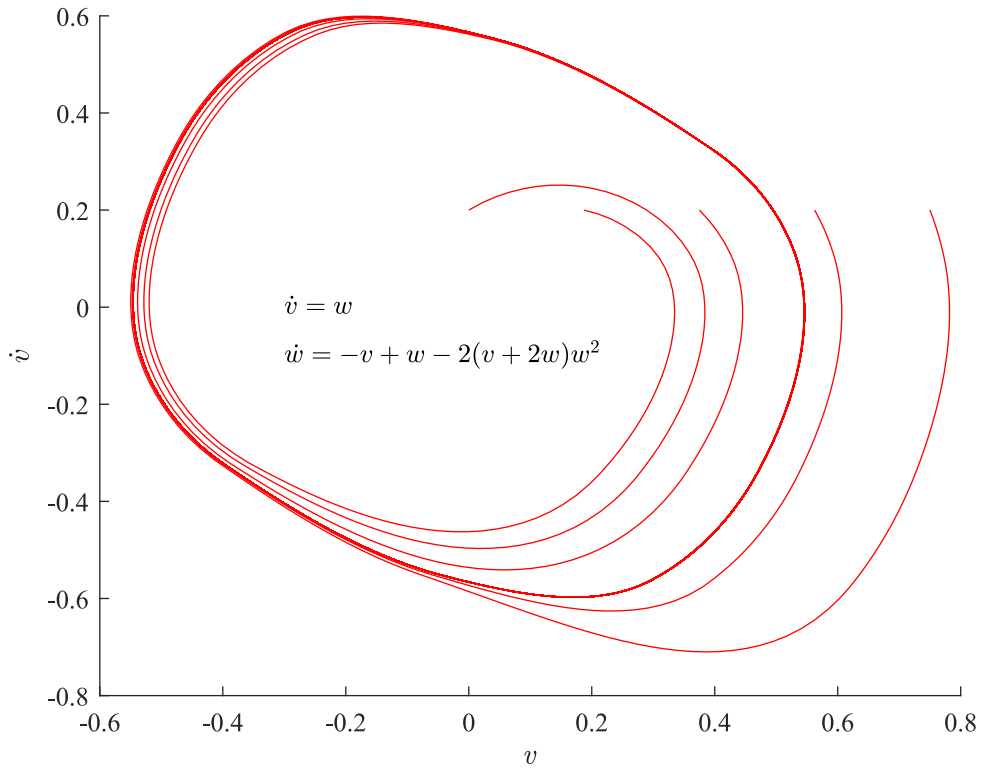

Figure 1.2: An example of limit cycle

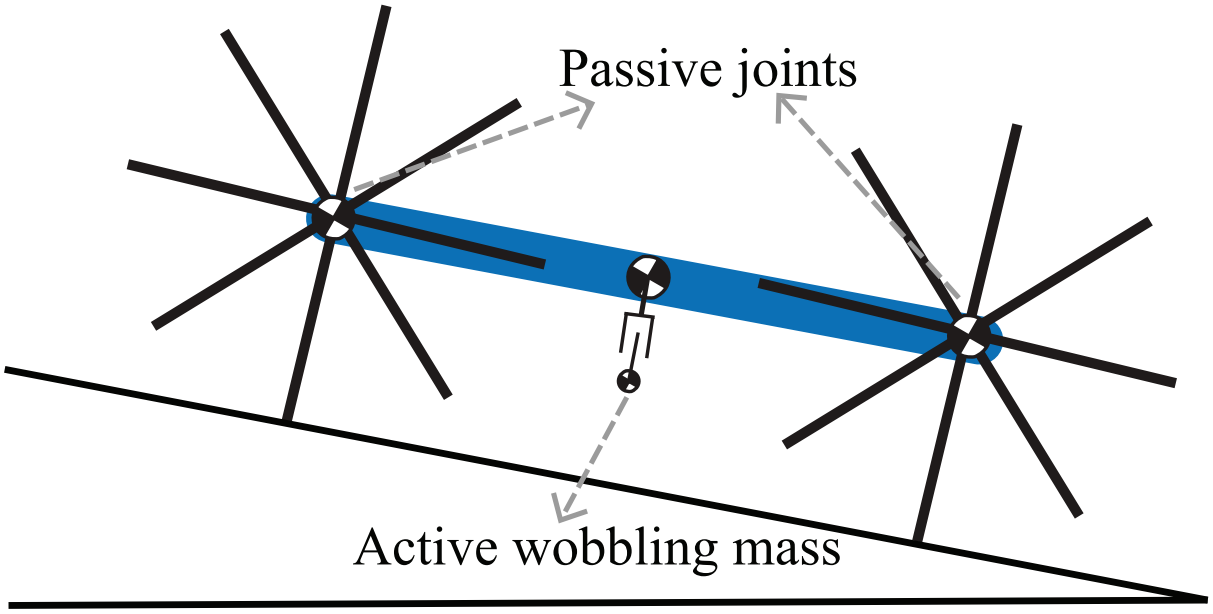

Figure 1.3: Indirectly controlled limit cycle walker

1.2.2 Entrainment effect

In mechanical engineering, the entrainment effect is the phenomenon that two (or more) coupled oscillators, which have different natural frequencies originally, gradually oscillate into the same pace via mechanical interaction [17]. More specifically, their phase difference becomes constant in each cycle. As shown in Fig. 1.4, the oscillators can be either in-phase or out-of-phase, even anti-phase. Neglect the DOF of the system, the nonlinear dynamics can be approximated using the phase reduction theory.

1.2.3 Phase reduction theory

Consider that the generalized coordinate of the robot locomotion system is $\boldsymbol{q}$. By introducing a state vector $\boldsymbol{Q} = \left[\boldsymbol{q}^{\mathrm{T}}\ \dot{\boldsymbol{q}}^{\mathrm{T}}\right]^{\mathrm{T}}$, the system dynamics can be arranged into following equation without going into the details of the equation of motion:

$$\frac{\mathrm{d}}{\mathrm{d}t}\boldsymbol{Q}(t) = \boldsymbol{\mathcal{F}}(\boldsymbol{Q}), \tag{1.1}$$

where t is time. In the condition that the locomotion converges to a limit cycle, the dynamics of the state vector $\boldsymbol{Q}$ can be simply described by the dynamics of a scalar phase θ along the orbit of the limit cycle through the mapping:

$$\theta(t) = \mathcal{G}(\boldsymbol{Q}(t)), \tag{1.2}$$

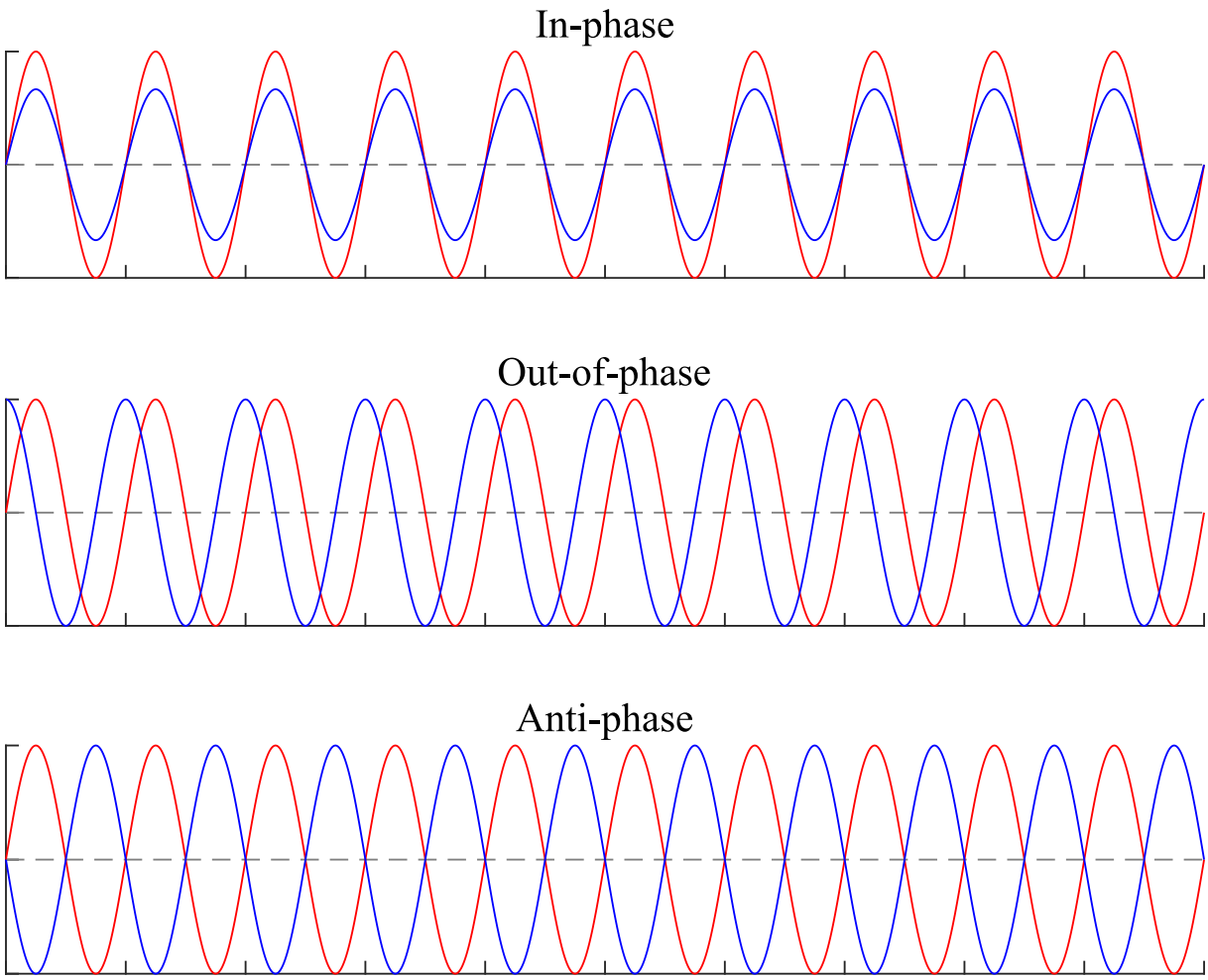

Figure 1.4: Phase coupling

where $0 \leq \theta < 2\pi$. By taking the time derivative of Eq. (1.2), we can obtain following equation via chain rule:

$$\frac{\mathrm{d}}{\mathrm{d}t}\theta(t) = \frac{\mathrm{d}}{\mathrm{d}t}\mathcal{G}(\boldsymbol{Q}(t)) = \boldsymbol{\nabla}_{\boldsymbol{Q}}\mathcal{G}\Big|_{\boldsymbol{Q}=\boldsymbol{Q}(t)} \frac{\mathrm{d}}{\mathrm{d}t}\boldsymbol{Q}(t) = \boldsymbol{\nabla}_{\boldsymbol{Q}}\mathcal{G}\Big|_{\boldsymbol{Q}=\boldsymbol{Q}(t)} \boldsymbol{\mathcal{F}}(\boldsymbol{Q}), \tag{1.3}$$

where $\boldsymbol{\nabla}_{\boldsymbol{Q}}\mathcal{G}$ is the gradient of $\mathcal{G}(\boldsymbol{Q})$ on $\boldsymbol{Q}$, or more specifically, represented as phase response curve (PRC) $\boldsymbol{Z}(\theta) = \boldsymbol{\nabla}_{\boldsymbol{Q}}\mathcal{G}$. If we define the mapping $\mathcal{G}(\boldsymbol{Q})$ that satisfies:

$$\boldsymbol{\nabla}_{\boldsymbol{Q}}\mathcal{G}\boldsymbol{\mathcal{F}}(\boldsymbol{Q}) = \boldsymbol{Z}(\theta)\boldsymbol{\mathcal{F}}(\boldsymbol{Q}) = 2\pi f_n, \tag{1.4}$$

$\theta(t)$ will vary with a constant angular frequency $2\pi f_n$ in terms of phase reduction theory [18] [19], and f_n is called the natural frequency of the phase oscillation.

In most cases, the phase response curve is difficult to be analytically derived. However, it can be numerically estimated by adding slight perturbations at different phases of the

limit cycle [20] [21] [22] [23]. Consider the case that a slight perturbation, which is represented as a slight impulse vector $\boldsymbol{I}_p$, is applied at the state $\boldsymbol{Q}_0$ with phase θ_0 on the limit cycle, the oscillator is, therefore, kicked to a new state $\boldsymbol{Q} = \boldsymbol{Q}_0(\theta_0) + \boldsymbol{I}_p$. The phase shift led by the perturbation becomes:

$$\mathcal{G}_\Delta = \mathcal{G}(\boldsymbol{Q}_0(\theta_0) + \boldsymbol{I}_p) - \mathcal{G}(\boldsymbol{Q}_0(\theta_0)). \tag{1.5}$$

The Taylor expansion of $\mathcal{G}(\boldsymbol{Q}_0(\theta) + \boldsymbol{I}_p)$ is

$$\mathcal{G}(\boldsymbol{Q}_0(\theta_0) + \boldsymbol{I}_p) = \mathcal{G}(\boldsymbol{Q}_0(\theta_0)) + \nabla_{\boldsymbol{Q}}\mathcal{G}\Big|_{\boldsymbol{Q}=\boldsymbol{Q}_0(\theta_0)} \boldsymbol{I}_p + \mathcal{O}(|\boldsymbol{I}_p|^2). \tag{1.6}$$

By subtracting $\mathcal{G}(\boldsymbol{Q}_0(\theta_0))$ from Eq. (1.6) and ignoring the infinite small part $\mathcal{O}(|\boldsymbol{I}_p|^2)$, one can understand that the phase shift approximates the gradient:

$$\mathcal{G}_\Delta \approx \nabla_{\boldsymbol{Q}}\mathcal{G}\Big|_{\boldsymbol{Q}=\boldsymbol{Q}_0(\theta_0)} \boldsymbol{I}_p. \tag{1.7}$$

It should be mentioned that the perturbation is necessary to be small enough that does not kick the oscillator outside the basin of attraction (BOA) of the limit cycle.

Since an active wobbling mass is forced to follow a desired trajectory in the indirectly controlled locomotion system, the approximated system dynamics represented in state space can be obtained by revising Eq. (1.1) to:

$$\frac{\mathrm{d}}{\mathrm{d}t}\boldsymbol{Q}(t) = \boldsymbol{\mathcal{F}}(\boldsymbol{Q}) + \boldsymbol{F}(t), \tag{1.8}$$

where $\boldsymbol{F}(t)$ is the forcing function. By multiplying $\boldsymbol{Z}(\theta)$ on each side of Eq. (1.8), the phase dynamics is expressed as:

$$\frac{\mathrm{d}}{\mathrm{d}t}\theta(t) = \boldsymbol{Z}(\theta)\boldsymbol{\mathcal{F}}(\boldsymbol{Q}) + \boldsymbol{Z}(\theta)\boldsymbol{F}(t) = 2\pi f_n + \boldsymbol{Z}(\theta)\boldsymbol{F}(t). \tag{1.9}$$

Based on this approximation, the nonlinear dynamics of the entrained systems can be analyzed and controlled by applying the phase model.

1.3 Research Goal

The main purpose of this research is to achieve stable and efficient locomotion of underactuated limit cycle robots using the indirectly controlling method by theoretically

analyzing the detailed nonlinear properties of it and optimizing the trajectory of wobbling motion based on the theory of phase oscillation. Therefore, before applying this method, nonlinear analysis, experimental verification and entrainment waveform optimization should be performed. More specifically, the goals of the dissertation are as follows:

1. Analyze the nonlinear dynamics of the indirectly controlling method with a simple example.

2. Experimentally verify the overall entrainment effect.

3. Seek an optimal entrainment waveform for the indirectly controlling method by means of phase reduction theory.

4. Achieve stable and efficient sliding locomotion on the slippery ground, where normal control methods are difficult to be applied naturally, with the indirectly controlling method.

5. Enhance the locomotion performance of the indirectly controlled sliding robot.

1.4 Organization of Dissertation

This dissertation is composed of 2 parts: The first part includes nonlinear analysis, experimental verification and entrainment waveform optimization for the indirectly controlling mechanism, which corresponds to Chapter 2,3 and 4. The second part applies indirectly controlling mechanism on achieving stable and efficient locomotion on slippery ground, which corresponds to Chapter 5 and 6. The details are shown as follows:

Chapter 2 performs typical nonlinear analyses of the indirectly controlling method using CRW as a simple example. Overall entrainment phenomenon, synchronization and chaos, as well as bistability are numerically observed and investigated.

Chapter 3 carries out an experiment with a real machine of CRW to verify the entrainment effect.

Chapter 4 analytically derives the optimal entrainment waveform for the indirectly controlling method by maximizing the entrainment range with fixed energy based on the phase reduction theory. The analytical result is also numerically verified.

Chapter 5 applies this indirectly controlling mechanism to a seed-like sliding robot for achieving stable locomotion on slippery ground. Stable forward sliding locomotion is generated and the performance is much better compared with related studies. Nonlinear analysis is performed for further optimization.

Chapter 6 improves the performance of the sliding locomotion robot via consuming the redundant energy and increasing the propulsive force at the underactuated grounding point by adding an elastic body. In addition, the entrainment effect is also enhanced benefited from the sinusoidal oscillation of the elastic body.

Chapter 7 is devoted to conclusions and future works.

Chapter 2

Nonlinear Analysis for Indirectly Controlling Method

2.1 Introduction

To deepen the investigation of the stability and efficiency of indirectly controlled limit cycle locomotion robots, analysis on nonlinear properties, such as entrainment, chaos and hysteresis phenomenon, is performed in this chapter, using combined rimless wheel with an active wobbling mass (CRW) as a simple example.

The detailed entrainment properties of forced nonlinear systems can be characterized by Arnold tongue in nonlinear dynamics [24], where the size of the Arnold tongue provides the frequency locking range, which quantifies entrainability of the oscillator. To observe various locomotion patterns, quasi-periodic and chaotic gaits can be drawn by plotting the phase difference between walker and wobbling mass in one cycle [25]. The sensitivity to initial conditions can be investigated via hysteresis phenomenon [26]. Furthermore, the basin of attraction (BOA), which measures the stable range of the dynamics, can be utilized to calculate the number of initial conditions leading to individual attractor [27].

Based on these analyses, nonlinear properties of the indirectly controlling method are clarified. The nonlinear analysis performed in this chapter contributes to deepening the understanding of the system dynamics of indirectly controlled locomotion robots, towards further optimization and generalization. This chapter is organized as follows. Section 2 introduces the simplified equation of motion and the control method. Section 3 performs

nonlinear analysis via drawing Arnold tongues, synchronized and chaotic gaits, and further investigates hysteresis phenomenon by computing the BOA. Finally, Section 4 is devoted to summary and discussions.

2.2 Modelling and Control

2.2.1 Equations of motion

As illustrated in Fig. 2.1, this indirectly controlled limit cycle walker is composed of two rimless wheels, an active wobbling mass and a body frame connects them together. The rear and fore rimless wheels' toe positions of stand legs are $(x_1,\, z_1)$, $(x_2,\, z_2)$, where their angular positions with respect to vertical are θ_1 and θ_2. The coordinate of the center of the body frame is located at $(x_3,\, z_3)$, where the angular position of it with respect to horizontal is θ_3. In addition, the lengths of the legs of the rear and fore rimless wheels are L_1 [m] and L_2 [m], and their masses are m_1 [kg] and m_2 [kg]. The length of the wobbling mass is L_c [m], which is actively controlled by control input u [N], and its mass is m_c [kg]. All of them are connected by the body frame with the length of $2L_3$ [m] and the mass of m_3 [kg].

Here, identical and symmetric 8-legged rimless wheels are adopted, therefore $2\alpha = \frac{\pi}{4}$

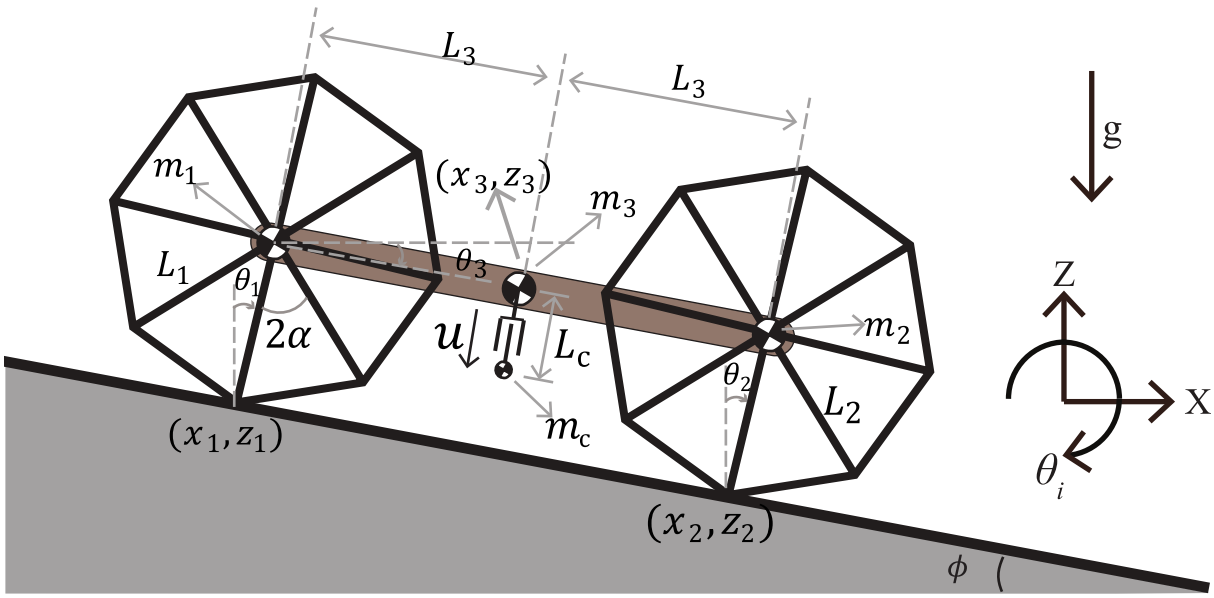

Figure 2.1: Combined rimless wheel with an active wobbling mass

[rad], which represents the inter-leg angle. This dissertation further let the two rimless wheels perfectly synchronized, in other words, $L_1 = L_2$, $m_1 = m_2$, $\theta_1 = \theta_2$. Therefore, the model is reduced to the following 2-DOF systems, where $\boldsymbol{q} = \begin{bmatrix} \theta_1 & L_c \end{bmatrix}^{\mathrm{T}}$ is the generalized coordinate, according to previous study [16]:

$$\ddot{\theta_1} = \frac{N_{\theta_1}}{D_{\theta_1}}, \quad \ddot{L_c} = \frac{N_{L_c}}{D_{L_c}}. \tag{2.1}$$

The detailed numerators and denominators are:

$$\begin{aligned} N_{\theta_1} &= (2m_w + m_c)g\sin\theta_1 - m_c g\sin(\theta_1 - 2\theta_3) \\ &\quad + m_c L\dot{\theta}_1^2 \sin(2(\theta_1 - \theta_3)) - 2\sin(\theta_1 - \theta_3)u, \end{aligned} \tag{2.2}$$

$$D_{\theta_1} = 2L(m_w + m_c\cos^2(\theta_1 - \theta_3)), \tag{2.3}$$

$$\begin{aligned} N_{L_c} &= (u + m_c(g\cos\theta_1 - L\dot{\theta_1}^2)\cos(\theta_1 - \theta_3))(m_w + m_c), \\ D_{L_c} &= m_c(m_w + m_c\cos^2(\theta_1 - \theta_3)), \end{aligned} \tag{2.4}$$

where $m_w := 2m_1 + m_3$ [kg], $L = L_1$ [m] and $\theta_3 = \phi$ (the slope angle) [rad] is a positive constant. The control input u will be introduced later.

To enable stable walking, the vertical ground reaction force λ should always be positive, which is calculated as follows [16]:

$$\lambda = -\frac{N_\lambda}{D_\lambda}, \tag{2.5}$$

where

$$\begin{aligned} N_\lambda &= \cos\theta_1(m_w(L\dot{\theta}_1^2 - g\cos\theta_1) + \cos(\theta_1 - \theta_3)u), \\ &\quad \times((m_w + m_c)L_3 - m_c L_c \tan(\theta_1 - \theta_3)) \end{aligned} \tag{2.6}$$

$$D_\lambda = 2L_3(m_w + m_c\cos^2(\theta_1 - \theta_3)). \tag{2.7}$$

2.2.2 Collision equations

Here inelastic collision model is used with the assumption that both fore and rear legs leave the ground immediately after collision. As derived in previous study [16]:

$$\dot{\theta_1}^+ = \frac{m_w\cos(2\alpha) + m_c\cos^2\alpha}{m_w + m_c\cos^2\alpha}\dot{\theta_1}^-, \tag{2.8}$$

$$\dot{L_c}^+ = \dot{L_c}^- + \frac{(m_w + m_c)L\sin(2\alpha)\cos\alpha}{m_w + m_c\cos^2\alpha}\dot{\theta_1}^-, \tag{2.9}$$

where the angular position and length of the wobbling mass is reset after collision:

$$\theta_1{}^+ = \theta_1{}^- - 2\alpha, \tag{2.10}$$

$$L_c{}^+ = L_c{}^-. \tag{2.11}$$

The superscript of "+" and "−" denotes immediately after and before collision.

2.2.3 Trajectory following control

The joints of the limit cycle walker are passive and the trajectory of the wobbling mass is actuated as follows:

$$\ddot{L}_c = A(\theta_1)u + B(\theta_1, \dot{\theta_1}), \tag{2.12}$$

where

$$A(\theta_1) = \frac{m_w + m_c}{m_c(m_w + m_c\cos^2(\theta_1 - \theta_3))}, \tag{2.13}$$

$$B(\theta_1, \dot{\theta_1}) = \frac{(m_w + m_c)(g\cos\theta_1 - L\dot{\theta_1}^2)}{m_w + m_c\cos^2(\theta_1 - \theta_3)}\cos(\theta_1 - \theta_3). \tag{2.14}$$

The control input that enables L_c to track a desired trajectory is defined as:

$$u = \frac{v - B(\theta_1, \dot{\theta_1})}{A(\theta_1)}, \tag{2.15}$$

$$v = \ddot{L}_{\mathrm{d}}(t) + K_{\mathrm{D}}(\dot{L}_{\mathrm{d}}(t) - \dot{L}_{\mathrm{c}}) + K_{\mathrm{P}}(L_{\mathrm{d}}(t) - L_{\mathrm{c}}), \tag{2.16}$$

where K_{D} [s^{-1}] and K_{P} [s^{-2}] are the PD control gains.

As an example of periodic and smooth waveform, sine wave was chosen as the desired trajectory of the wobbling mass:

$$L_{\mathrm{d}}(t) = A_m\sin(2\pi f_c t), \tag{2.17}$$

where A_m [m] and f_c [Hz] denote desired wobbling amplitude and wobbling frequency respectively. With appropriate A_m [m] and f_c [Hz], the walking frequency f_w [Hz], which is defined by the inverse of the duration between adjacent collisions, can be entrained to the up-and-down wobbling motion.

2.3 Nonlinear Analysis

2.3.1 Overall entrainment effect

To systematically analyze the entrainment property, Arnold tongues are drawn to quantify the overall locking range of this forced oscillation system. Following process is conducted by using the parameters listed in Tab. 2.1:

(A1) Set the desired wobbling amplitude A_m to 0.0005 [m].

(A2) Set the desired wobbling frequency f_c to 1.2 [Hz].

(A3) Set the initial conditions as:

$$\boldsymbol{q}(0) = \begin{bmatrix} \phi - \alpha & 0 \end{bmatrix}^{\mathrm{T}}, \dot{\boldsymbol{q}}(0) = \begin{bmatrix} 4 & 2\pi f_c A_m \end{bmatrix}^{\mathrm{T}} \tag{2.18}$$

and start the locomotion.

(A4) After 100 [s] of walking, save the walking frequency f_w for 20 steps.

(A5) Increase f_c by 0.025 [Hz] and return to (A3).

(A6) Repeat from (A3) to (A5) until $f_c = 4.5$ [Hz].

(A7) Increase A_m by 0.0005 [m] and return to (A2).

Table 2.1: Parameter settings for simulation model of CRW

$m_1(= m_2)$	1.0	kg
m_3	1.0	kg
m_c	0.1	kg
$L(= L_1 = L_2)$	0.15	m
L_3	0.20	m
ϕ	0.07	rad
g	9.81	$\mathrm{m/s^2}$
K_D	40	$\mathrm{s^{-2}}$
K_P	400	$\mathrm{s^{-1}}$

(A8) Repeat from (A2) to (A7) until $A_m = 0.03$ [m].

Therefore the f_w is obtained within the range of $A_m = 0.0005 : 0.0005 : 0.03$ [m], $f_c = 1.2 : 0.025 : 4.5$ [Hz].

As the Arnold tongues, this chapter focuses on $1:1$ and $1:2$ entrainment, which represent dominant entrainment ranges. The $1:n$ entrainment is defined by $\bar{f}_w : f_c = 1 : n$, where $n = 1, 2$ and $\bar{\cdot}$ denotes frequency averaged over 20 periods. As shown in Fig. 2.2, typical Arnold tongues are observed, where the boundaries are estimated by linear regression. The shapes of Arnold tongues are roughly triangular, *i.e.*, an increasing entrainment amplitude results in a broader locking range, which indicates that the underactuated system becomes a weakly forced oscillator entrained by the active wobbling motion. The $1:2$ Arnold tongue, which indicates that, during 2 cycles of wobbling, there is only one step of walking on average, is wider than the $1:1$ Arnold tongue. In terms of controlling efficiency, $1:1$ entrainment is more efficient than $1:2$ entrainment.

To observe the detailed structure of the gait frequencies and further examine whether the phase differences of the unentrained walking are chaotic or quasi-periodic, the amplitude is fixed and the frequency of the wobbling motion only is varied. The phase difference between the walker and wobbling mass is defined as follows:

$$\psi := \frac{2\pi(t_c - t_w)}{T}. \tag{2.19}$$

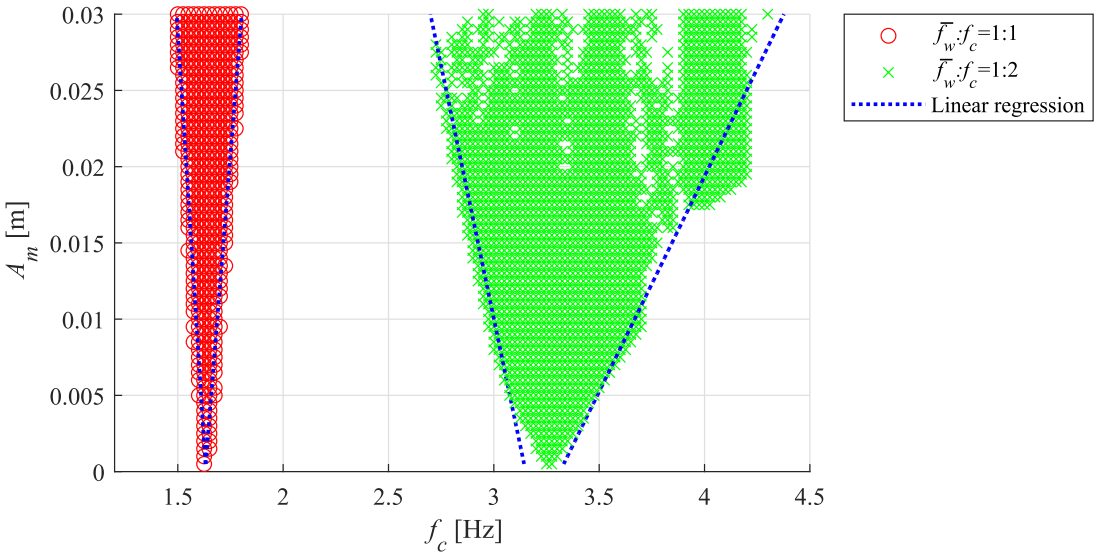

Figure 2.2: Arnold tongues with respect to wobbling frequency and amplitude

Here T [s] is the fundamental period of the wobbling motion. t_c [s] denotes the timing, at which the wobbling mass reaches local minimum, whereas t_w [s] denotes the timing, at which the center of the leg is normal to the slope.

To examine the effect of weight and oscillation amplitude of the wobbling mass on the walking pattern, two conditions are considered:

(I)$m_c = 0.1$ [kg], $A_m = 0.03$ [m].

(II)$m_c = 1$ [kg], $A_m = 0.05$ [m].

The numerical simulation is conducted according to the following process:

(B1) Set the desired wobbling frequency f_c to 0 [Hz].

(B2) Set the initial conditions to the values of Eq. (2.18) and start the locomotion.

(B3) After 100 [s] of walking, save the walking period f_w and calculate phase ψ for 100 steps.

(B4) Increase f_c by 0.01 [Hz] and return to (B2).

(B5) Repeat from (B2) to (B4) until $f_c = 5$ [Hz].

A variety of entrained walking patterns are shown in Fig. 2.3, where the dot-lines represent $1:1$ and $1:2$ synchronizations. At the beginning of $1:2$ synchronization, period-2 walking is observed. In contrast, the heavy and strong wobbling mass is entrained only to $1:1$ synchronization as shown in Fig. 2.4. The range where f_w has no value means failure of the gait, due to incapability of overcoming the potential barrier or unsatisfied holonomic constraint (negative λ exists in the locomotion).

The phase differences of condition (I) appear chaotic as shown in Fig. 2.5, whereas the phase differences of condition (II) appear mostly quasi-periodic as shown in Fig. 2.6. The results indicate that chaotic gaits are more often induced by lighter and weaker wobbling mass.

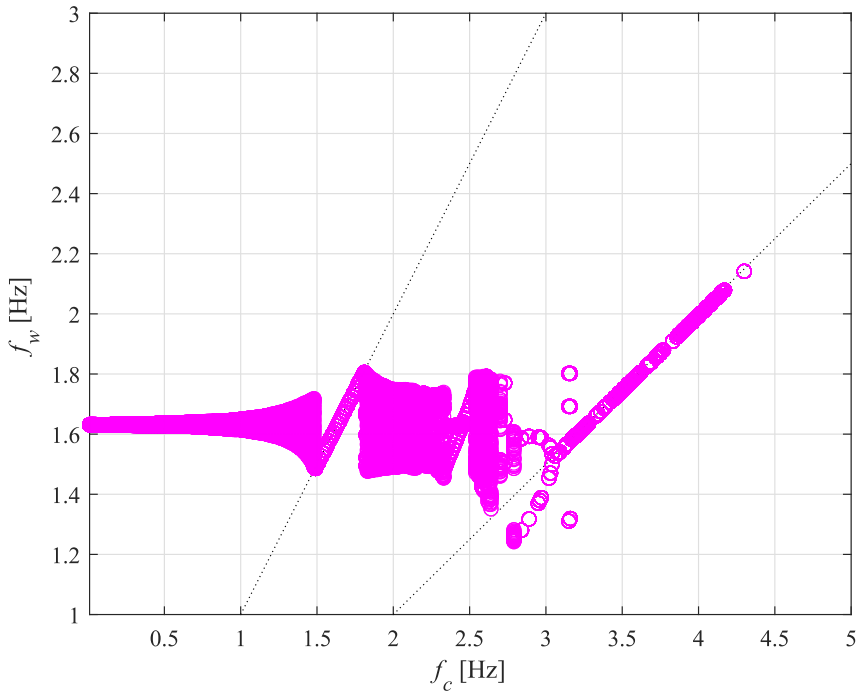

Figure 2.3: Walking frequency with respect to wobbling frequency of a light and weak wobbling mass

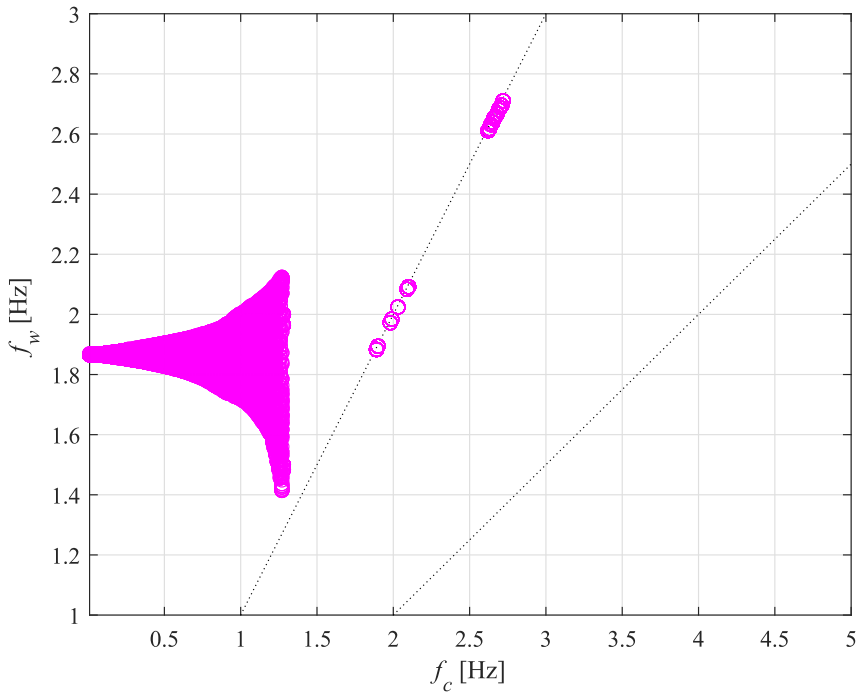

Figure 2.4: Walking frequency with respect to wobbling frequency of a heavy and strong wobbling mass

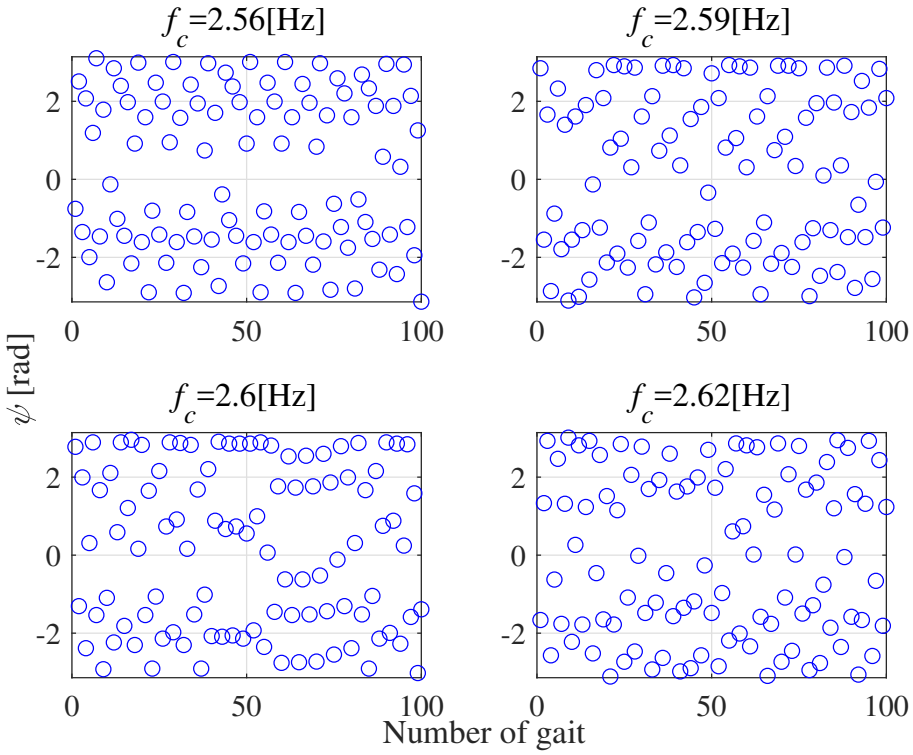

Figure 2.5: Variation of phase differences of a light and weak wobbling mass

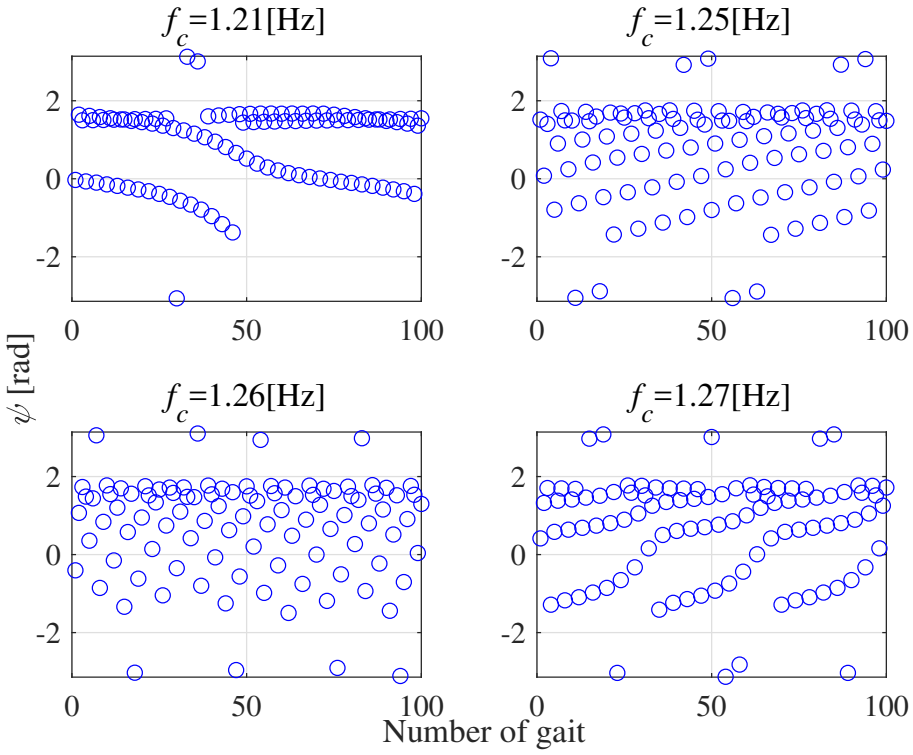

Figure 2.6: Variation of phase differences of a heavy and strong wobbling mass

2.3.2 Hysteresis phenomenon

To observe hysteresis phenomenon induced by the existence of bistable gaits in the same parameter space, a light wobbling mass ($m_c = 0.01$ [kg]) with weak entrainment amplitude ($A_m = 0.01$ [m]) is used. The numerical simulation is conducted as follows.

(C1) Set $f_c = 1$ (or 20) [Hz] and the initial conditions to the values of Eq. (2.18) and start the locomotion.

(C2) After 100 [s] of locomotion, save f_w for 20 periods and the final state immediately after collision.

(C3) Increase (or decrease) f_c by 0.05 [Hz] and run the next simulation by using the final state of (C2) as the initial state and return to (C2).

(C4) Repeat from (C2) to (C3) until $f_c = 20$ (or 1) [Hz].

As shown in Fig. 2.7, within the range of A: $f_c \in [11.6, 12.05]$ [Hz], and B: $f_c \in [12.85, 13.55]$ [Hz], the existence of steady gaits with different synchronization ratios are observed. $1:7$ and $1:8$ synchronizations coexist in the range A, whereas $1:8$ and $1:9$ synchronizations coexist in the range B. To clarify which of the two attractor dominates the BOA, the ratio between the number of initial conditions attracted to each attractor is calculated.

2.3.3 Basin of attraction

The Poincaré section is chosen as the instance immediately after the feet collision in walking robots [28], according to the generalized coordinate, the remaining state vector becomes $\tilde{\boldsymbol{X}} = \begin{bmatrix} L_c & \dot{\theta}_1 & \dot{L}_c \end{bmatrix}^{\mathrm{T}}$. The analysis of the bistability based on the calculation of the BOA requires an autonomous system, *i.e.*, a system not explicitly dependent on time. The controller, however, makes the system non-autonomous since time t is in the expression for the desired trajectory of the wobbling mass in Eq. (2.17). We therefore convert it to an autonomous system by simply extending $\tilde{\boldsymbol{X}}$ to an augment state vector $\bar{\boldsymbol{X}} = \begin{bmatrix} L_c & \dot{\theta}_1 & \dot{L}_c & L_{\mathrm{d}} \end{bmatrix}^{\mathrm{T}}$, which is updated at the Poincaré section in each step:

$$\bar{\boldsymbol{X}}(n+1) = \boldsymbol{P}(\bar{\boldsymbol{X}}(n)), \tag{2.20}$$

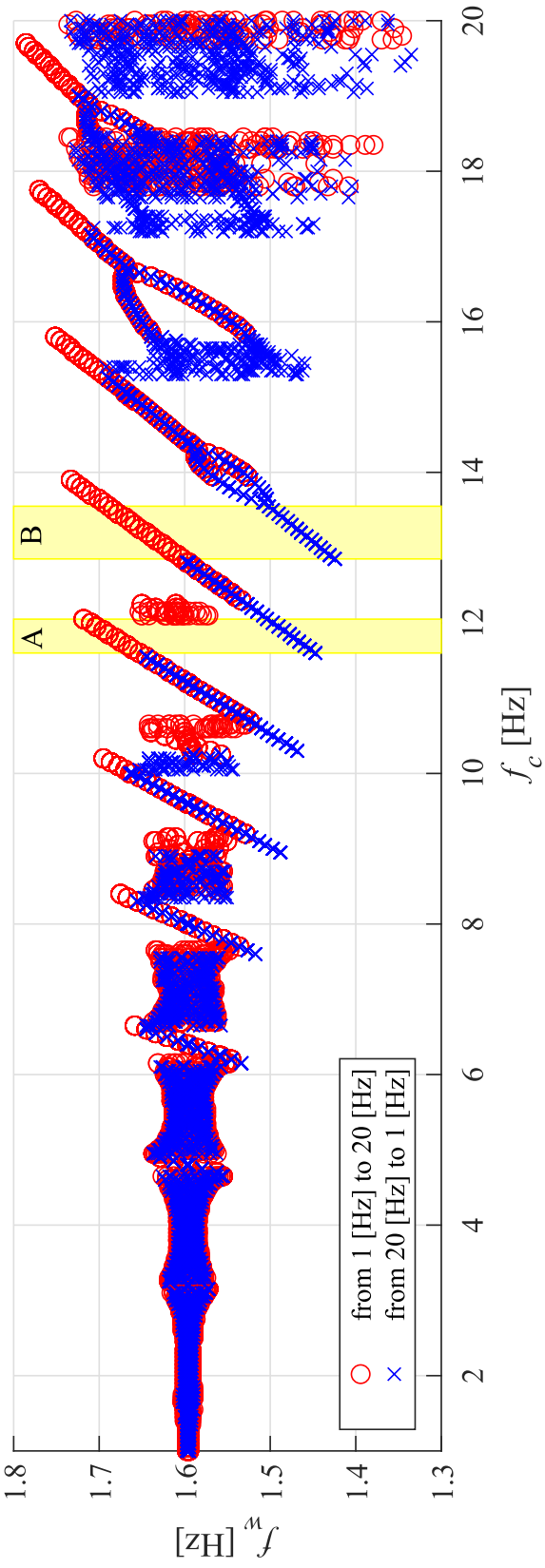

Figure 2.7: Hysteresis phenomenon in walking frequency

where n is the step number and $\boldsymbol{P}$ is the Poincaré map. An initial condition is attracted to the following steady state, which is invariant with respect to the Poincaré map:

$$\bar{\boldsymbol{X}}^* = \boldsymbol{P}(\bar{\boldsymbol{X}}^*). \tag{2.21}$$

It is considered that this steady state is asymptotically stable in the sense that the locomotion converges to it by free running from various initial conditions.

The range of initial conditions for the states are chosen as follows:

(D1) $L_c \in [-A_m, A_m]$ [m].

(D2) $\dot{\theta}_1 \in [2.6, 2.7]$ [rad/s].

(D3) $\dot{L}_c \in [-2\pi f_c A_m, 2\pi f_c A_m]$ [m/s].

(D4) $t_0 \in [0, \frac{10}{11} \cdot \frac{1}{f_c}]$ [s], where t_0 denotes the beginning of the locomotion.

Since each range is equally discretized to 10 intervals, 11 samples are generated. For each f_c, the number of total initial conditions is therefore $11^4 = 14641$. The ratio between the number of initial conditions attracted to different entrainment states is defined in logarithmic scale as:

$$\gamma = \log_{10} \frac{n_a}{n_b}, \tag{2.22}$$

where n_a and n_b denote numbers of initial conditions attracted to two entrainment states. The ratio is calculate over the range of f_c in Section 2.3.2 (A: $f_c \in [11.6, 12.05]$ [Hz], and B: $f_c \in [12.85, 13.55]$ [Hz]).

The result of Fig. 2.8 shows that γ varies from positive to negative in the range A, indicating that the dominant attractor changes. Note that, on the dashed line ($\gamma = 0$), size of the BOA becomes the same for the two entrainment states. To explain this phenomenon, an amplified view around range A of hysteresis plot is shown in Fig. 2.10. The gait of 1 : 7 synchronization remains stable below the lower boundary of the range, where the gait of 1 : 8 synchronization vanishes. In contrast, the gait of 1 : 8 synchronization remains stable above the upper boundary of the range, where the gait of 1 : 7 synchronization vanishes. The result implies that the increasing of wobbling frequency enhances the stability of 1 : 8 synchronization and weakens the stability of 1 : 7 synchronization,

which is considered as the reason of the change in dominant attractor with respect to wobbling frequency.

On the other hand, Fig. 2.9 shows that γ is always positive in the range B, indicating that the dominant attractor remains unchanged. As shown in Fig. 2.11, the gait of $1:8$ synchronization remains stable both below and above the boundaries of range B, where the gait of $1:9$ synchronization vanishes. The result implies that the stability of $1:9$ synchronization is weaker than that of $1:8$ synchronization, which is considered as the reason why the dominant attractor remains the same.

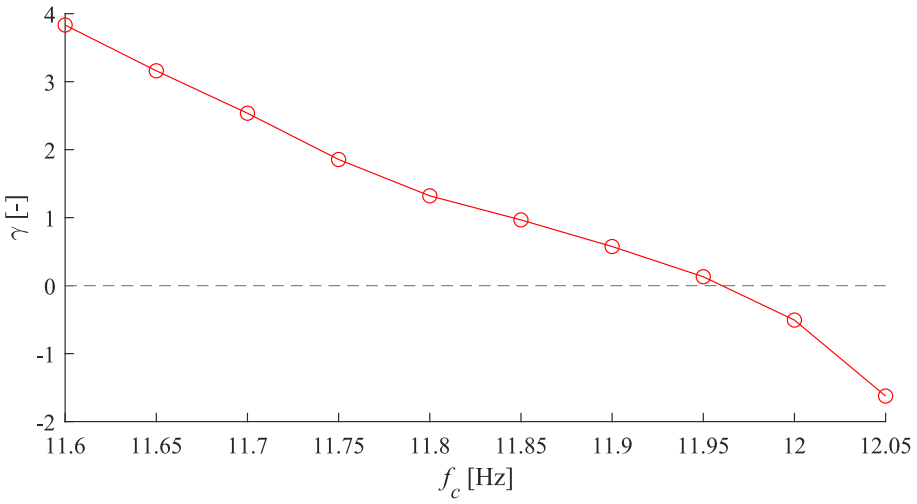

Figure 2.8: Attraction ratio with respect to wobbling frequency in range A

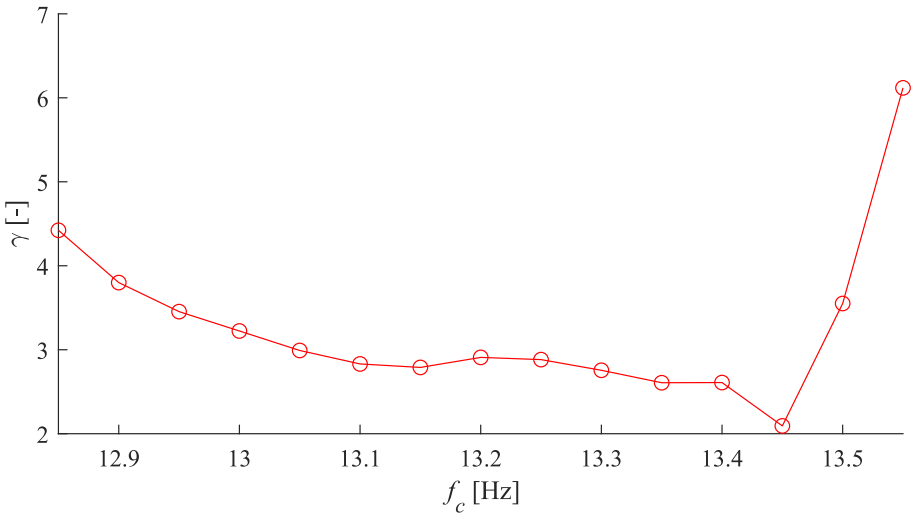

Figure 2.9: Attraction ratio with respect to wobbling frequency in range B

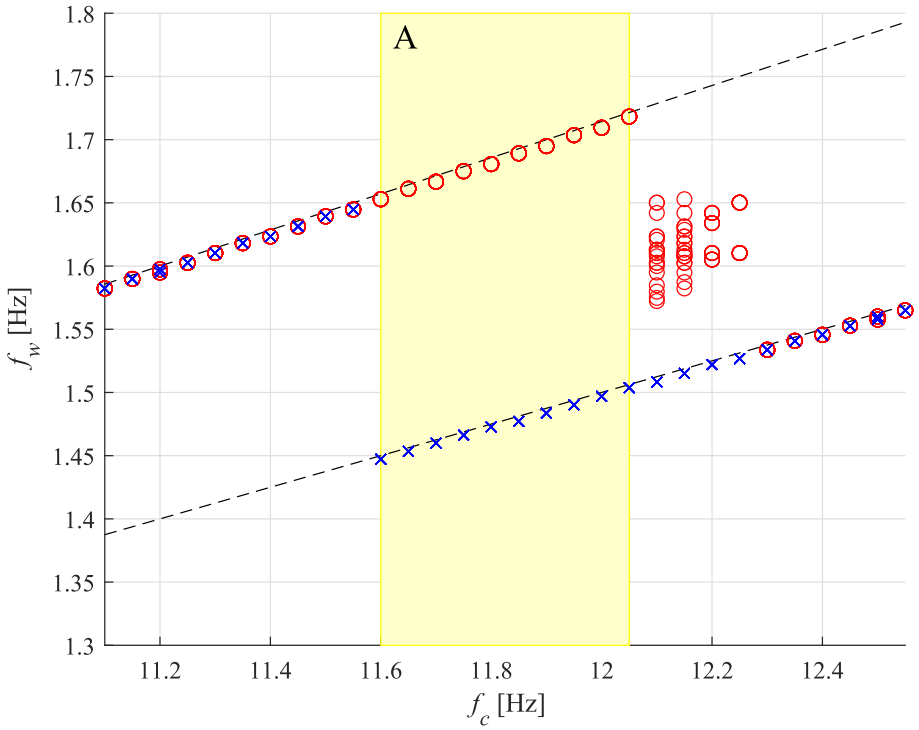

Figure 2.10: Amplified view of range A in hysteresis plot

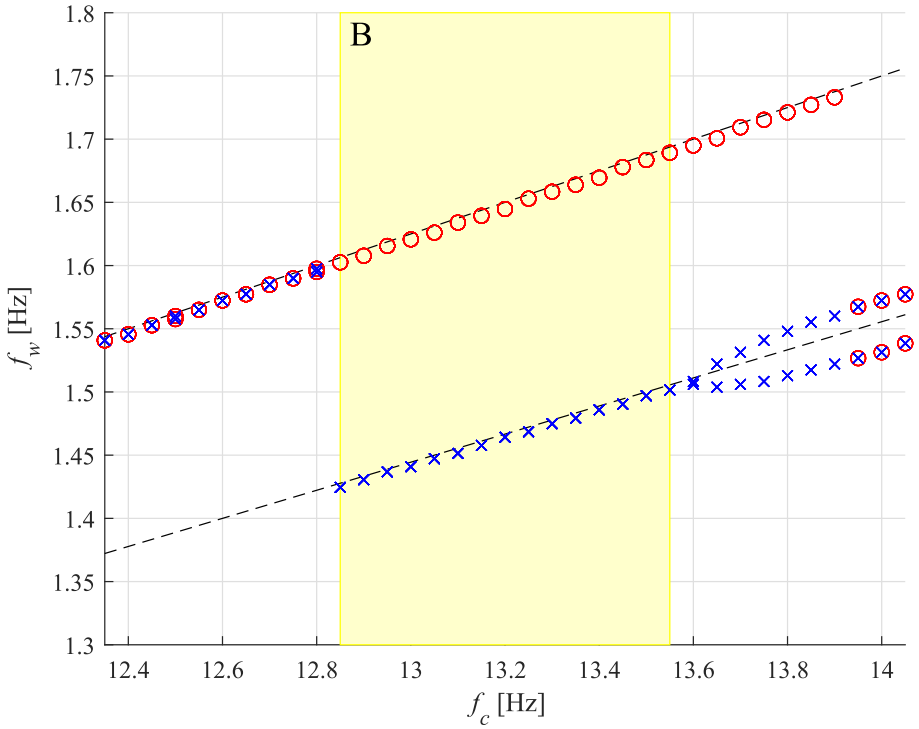

Figure 2.11: Amplified view of range B in hysteresis plot

2.4 Summary and Discussions

To understand the mechanism of indirectly controlled limit cycle locomotion robots, nonlinear analysis has been performed using CRW as a simple example. It has been found that the frequency locking range has a positive correlation with the entrainment amplitude. The results also showed that lighter wobbling mass with smaller wobbling amplitude shows more complicated characteristics in synchronization as well as in chaotic gaits. Computation of the BOA clarified that, in some parameter range, two different entrainment states coexist, giving rise to hysteresis phenomena. In such parameter range, desired locomotion with an energy efficient attractor should dominate the initial conditions. Enlarging the BOA for such ideal attractor is therefore necessary.

Before seeking an optimal entrainment waveform for the indirectly controlled robot by taking into account the frequency locking range [29] as well as the BOA into account, experimentally verification of the overall entrainment effect using a real machine is also important to bridge a gap between simulation and experiment.

Chapter 3

Experimental Verification of Entrainment Effect for Indirectly Controlling Method

3.1 Introduction

In Chap. 2, nonlinear analysis of indirectly controlled locomotion robots is conducted using CRW as an example. The overall entrainment effect, which is the central issue in this method, is experimentally verified in this chapter. In previous research [16], experimental study of entrainment effect of this walker is observed by means of walking velocity due to the fact that the foot collision is not measured. This method, however, highly depends on one assumption, *i.e.*, the robot is walking with restrict planar motion, which is difficult to be guaranteed in real experiment. Moreover, the Arnold tongue, which interprets detailed entrainment properties, has not been experimentally obtained.

To measure the step period, a novel method is proposed to detected foot collision via the accelerometer MPU6050 [30], inspired by the original mathematical model of collision equation. In addition, the Arnold tongue is obtained by changing the amplitude of wobbling motion. The experimental obtained Arnold tongue suggests that there is no doubt that the walker is entrained to the wobbling mass, which is consistent with the numerical results.

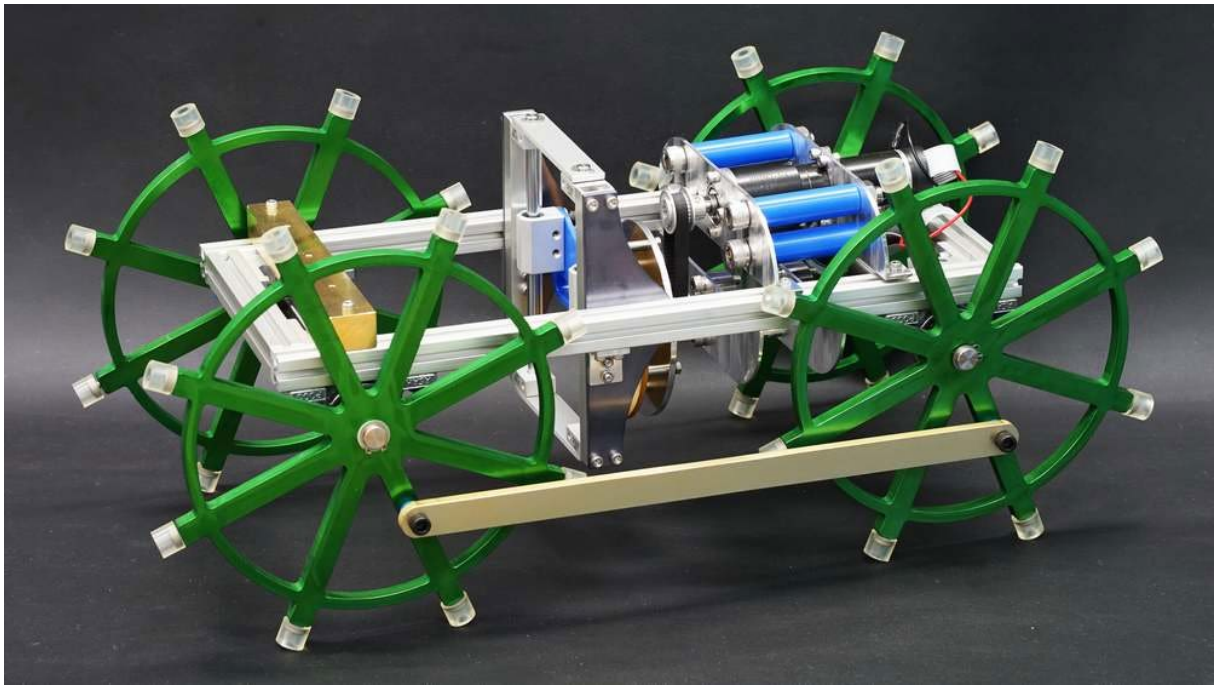

Figure 3.1: Experimental machine of combined rimless wheel with an active wobbling mass

3.2 Experimental Study

3.2.1 System design

An overview of the prototype experimental machine with the drive unit and the wobbling mass is shown in Fig. 3.1. The wobbling unit can carry one weight plate and moves up-and-down along the guide rail according to the piston crank mechanism driven by a Maxon DC motor [31] controlled by EPOS2. The motor driver controls the DC motor in speed-control mode so that it rotates at a constant rotating speed since the desired trajectory for wobbling mass is the sine waveform. The fore and rear rimless wheels are connected by rigid rods on each side. The amplitude of the motion can be adjusted by changing the mounting position of the crankshaft.

Instead of using the simplified collision equations introduced in Chap. 2, the original state transition is specified as:

$$\boldsymbol{M}(\boldsymbol{q})\dot{\boldsymbol{q}}^{+} = \boldsymbol{M}(\boldsymbol{q})\dot{\boldsymbol{q}}^{-} + \boldsymbol{J}_I(\boldsymbol{q})^{\mathrm{T}}\boldsymbol{\lambda}_I, \tag{3.1}$$

$$\boldsymbol{J}_I(\boldsymbol{q})\dot{\boldsymbol{q}}^{+} = \boldsymbol{0}_{8\times 1}, \tag{3.2}$$

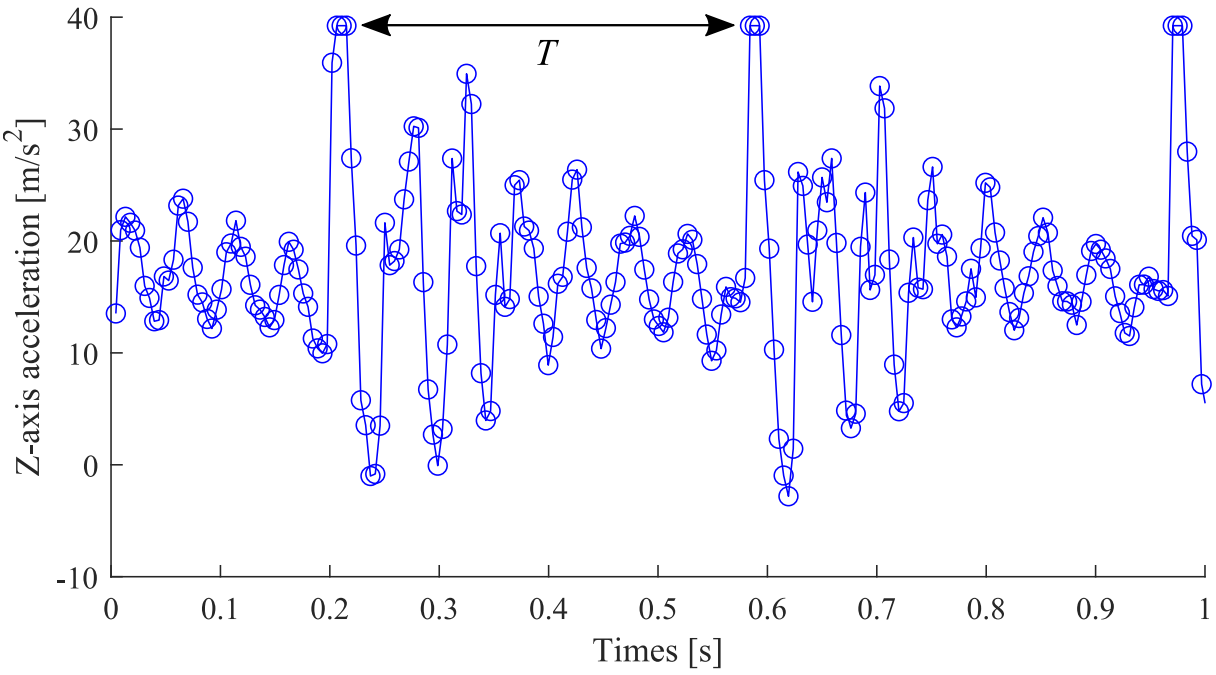

Figure 3.2: Measurement of ground collision

where $\boldsymbol{M}(\boldsymbol{q})$ is the inertial matrix, and $\boldsymbol{\lambda}_I$ represents the collision ground reaction force. Since the second element of $\boldsymbol{\lambda}_I$ is an impulse force towards vertical direction, a suddenly change in the acceleration of vertical direction at the collision timing can be expected. The detection of step, therefore, is equivalent to finding the maxima of the vertical acceleration in the experiment.

Based on the assumption above, the ground collisions are measured by the accelerometer MPU6050 via detecting the maxima of the vertical acceleration as shown in Fig. 3.2, where the signal has been denoised by passing through the Kalman filter [32]. In addition, the experimental system is shown as Fig. 3.3.

3.2.2 Frequency locking

The experiment is conducted using the parameters in Table 3.1 under two conditions:

(I) $\phi = 4.1$[deg]

(II) $\phi = 3.6$[deg]

The mean and variance of walking frequency with respect to the wobbling frequency is shown in Fig. 3.4 and 3.5. Each walking frequency is obtained by averaging over 1 trial of

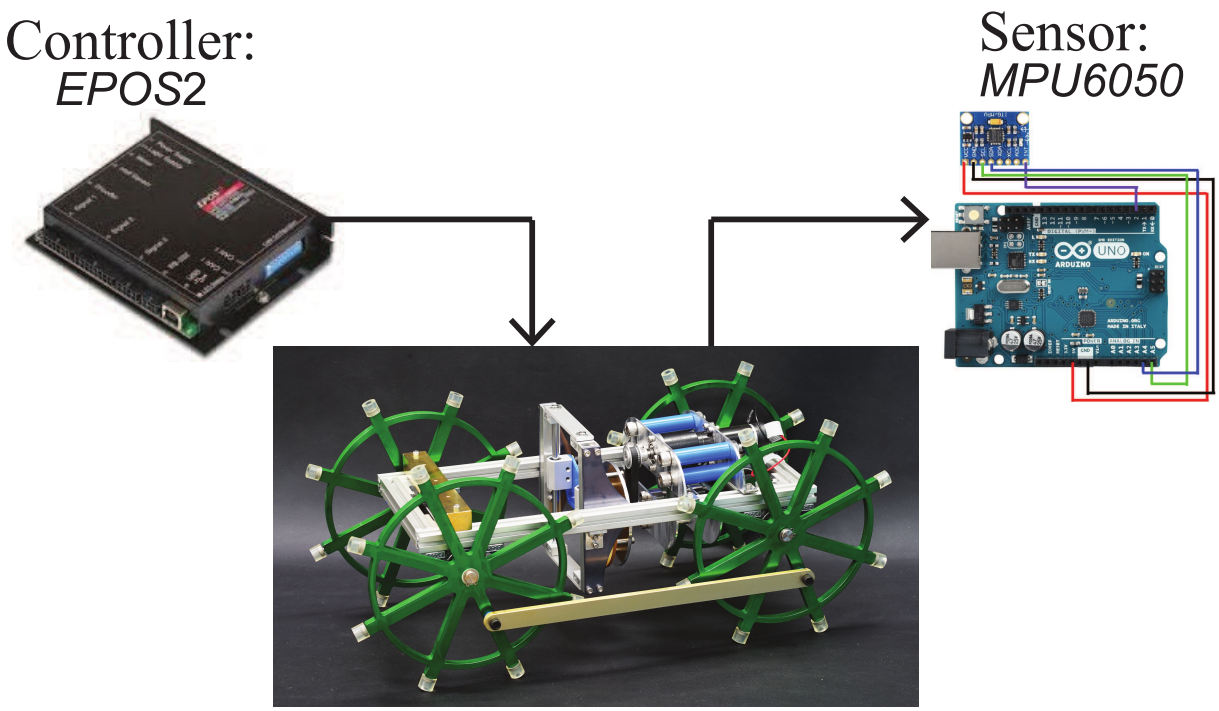

Figure 3.3: Experimental system

Table 3.1: Physical parameters of experimental CRW machine

$m_1(=m_2)$	0.455	kg
m_3	2.4	kg
m_c	0.186	kg
$L(=L_1=L_2)$	0.1	m
L_3	0.27	m
g	9.81	m/s^2
A_m	0.042	m

more than 40 gaits after enough transient. The results indicate that the frequency locking range becomes wider with a gentler slope. By considering the walker and wobbling mass as two oscillators, the steeper the slope, the stronger the dynamics of the walker becomes, the effect of wobbling, therefore, becomes slighter. The natural frequencies of these two conditions are roughly estimated as the center of frequency locking ranges, $f_{n1} \approx 3.0$ [Hz], $f_{n2} \approx 2.5$ [Hz].

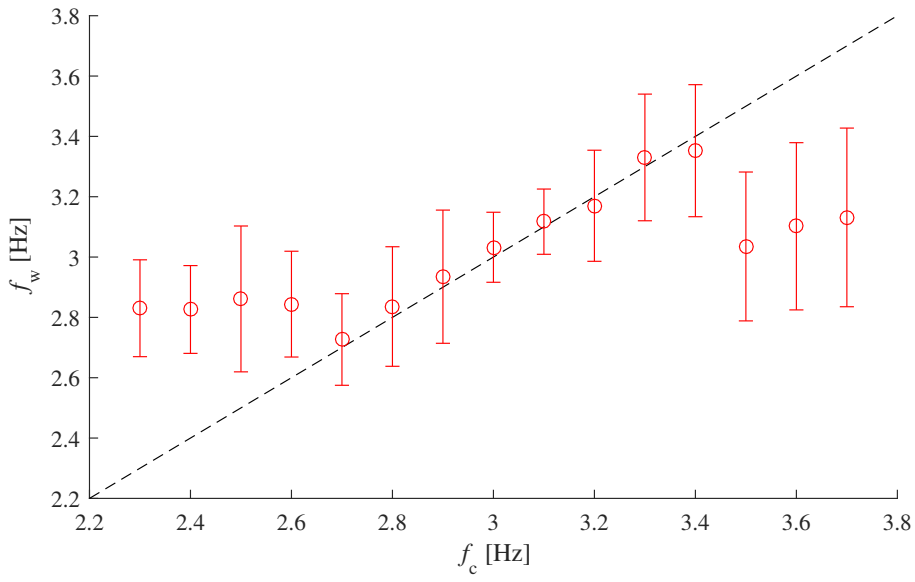

Figure 3.4: Walking frequency with respect to wobbling frequency on a steep slop

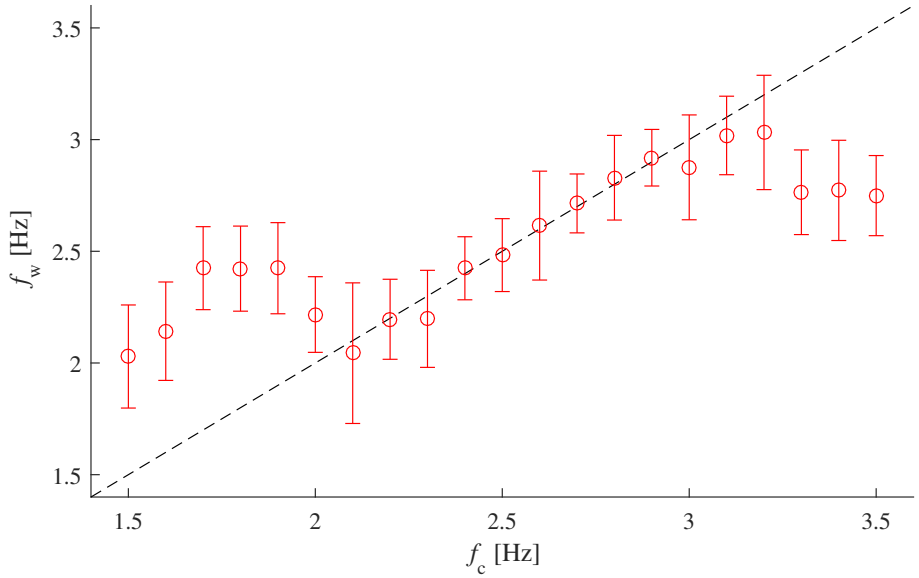

Figure 3.5: Walking frequency with respect to wobbling frequency on a gentle slop

3.2.3 Arnold tongue

To observe the whole structure of entrainment phenomenon, a rough Arnold tongue is obtained by setting $\phi = 3.6$ [deg] with conducting following process:

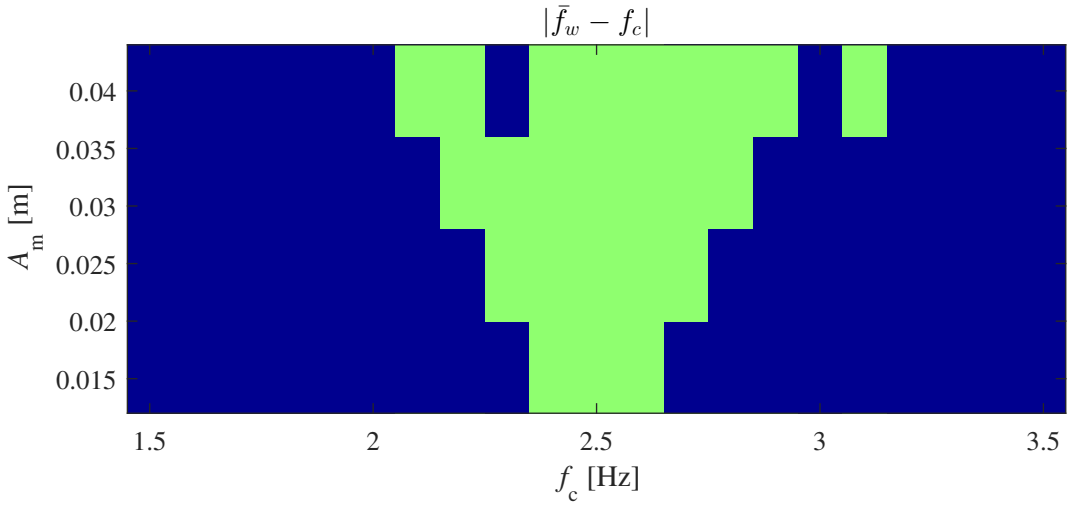

Figure 3.6: Experimentally obtained Arnold tongue

(A1) Set the desired wobbling amplitude A_m to 0.016 [m].

(A2) Set the desired wobbling frequency f_c to 1.5 [Hz].

(A3) Start the locomotion and obtain the acceleration signal for enough time (more than 2 minutes).

(A4) Increase f_c by 0.1 [Hz] and return to (A3).

(A5) Repeat from (A3) to (A4) until $f_c = 3.5$ [Hz].

(A6) Increase A_m by 0.008 [m] and return to (A2).

(A7) Repeat from (A2) to (A6) until $A_m = 0.042$ [m].

The transient gaits are deleted and the original Arnold tongue is shown in Fig. 3.6, where the entrainment phenomenon is defined as $|\bar{f}_w - f_c| < 0.1$ [Hz]. The walker is entrained to the wobbling mass around its natural frequency, since typical Arnold tongue is observed. As the amplitude of the wobbling motion is increased, the entrained frequency range also increases. Fig. 3.7 shows the Arnold tongue obtained by using Matlab's "contourf" function. The frequency difference increases if the wobbling frequency deviates the natural frequency.

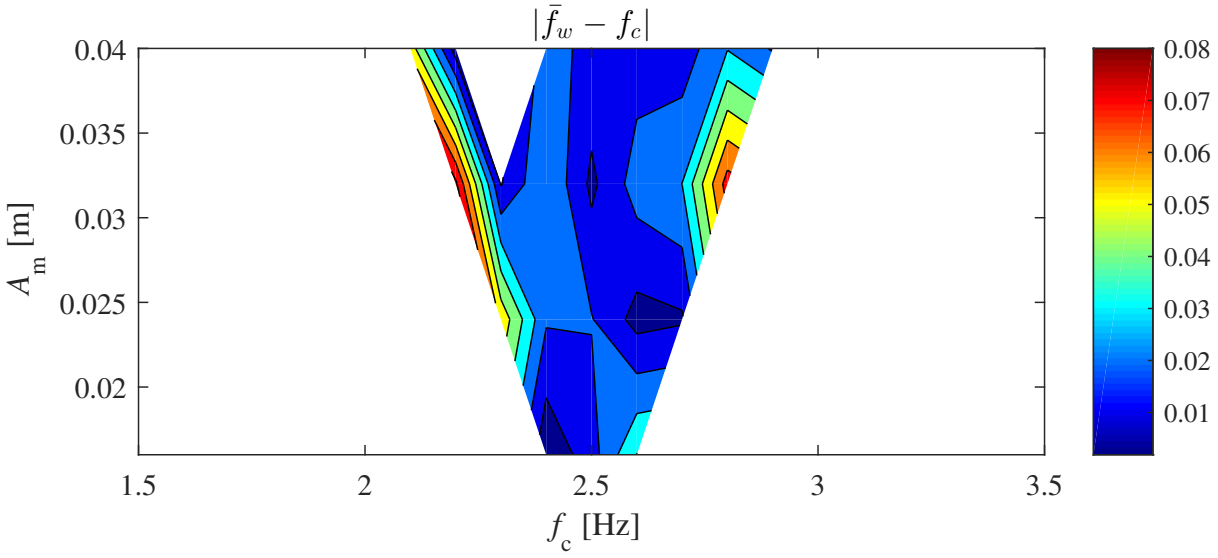

Figure 3.7: Contour plotted Arnold tongue

3.3 Summary and Discussions

The entrainment effect of the indirectly controlled limit cycle walker is experimentally verified via frequency locking and Arnold tongue in this chapter, and the results are consistent with the numerical simulations. In the real experiment, however, the variance of walking frequency is included due to the existence of the system noise. More detailed analysis, *e.g.*, phase difference, can be further conducted by obtaining the signals of motor and rimless wheel rotation with encoder and additional sensors.

With these verification, one can safely believe the entrainment effect occurred in this indirectly controlled locomotion system, and an optimal waveform for entrainment is expected.

Chapter 4

Optimal Entrainment Waveform for Indirectly Controlled Method

4.1 Introduction

In this chapter, an optimal entrainment waveform for the indirectly controlled locomotion robots is derived to reduce the forcing energy using CRW as a simple example. Since the overall entrainability is measured by the width of the Arnold tongue, *i.e.*, the entrainment range [17]. The wider the Arnold tongue is, the broader the range of walking frequencies, to which the walker could be locked into, becomes. Therefore, the optimization is always defined as the maximization of the entrainment range [29]. Consequently, the optimal input waveform is derived by maximizing the frequency entrainment range based on the theory of phase oscillators. The analytical method is further confirmed by numerical simulations.

This chapter is organized as follows. Section 2 obtains the phase response curve (PRC) numerically by applying perturbations at different phases of the walker's gait interval and calculating the deviations from the unperturbed. Section 3 analytically derives an optimal entrainment waveform for the wobbling mass to entrain the combined rimless wheel based on the PRC. As an ecological extension, an ideal entrainment waveform for $m : 1$ entrainment was further generated. Section 4 analysis typical walking gait with the obtained optimal entrainment waveform. Section 5 evaluates the proposed method by entrainment range of the Arnold tongues. Finally, Section 6 is devoted to summary

and discussions. The results show that the optimal entrainment waveform derived in this chapter achieves the best performance for $1:1$ entrainment among all the candidates. One of the strongest advantages of this method is the easiness of its implementation, prompting its applicability to a wide variety of locomotion systems.

4.2 Phase Response Curve

Nonlinear analysis performed in Chap. 2 showed the complicated dynamics of indirectly controlled locomotion robots, although it was reduced to 2-DOF. Fortunately, as introduced in Chap. 1, these robots can be analyzed and controlled via phase model. Here we can rewrite the phase dynamics Eq. (1.9) (in Chap. 1) to following equation since the wobbling motion is periodic:

$$\dot{\theta} = 2\pi f_n + \boldsymbol{Z}(\theta)\boldsymbol{F}(2\pi f_c t). \tag{4.1}$$

In addition, due to the fact that the indirectly controlled locomotion robots introduced in this dissertation use single wobbling mass only, the forcing function is, therefore, a scalar, and Eq. (4.1) is reduced to:

$$\dot{\theta} = 2\pi f_n + Z(\theta)F(2\pi f_c t). \tag{4.2}$$

The natural frequency f_n can be obtained by fixing the wobbling mass on the beam and start the locomotion until it converges. The periodic forcing function is equivalent to the desired trajectory L_{d} (introduced in Chap. 2) of wobbling mass. The phase dynamics equation can be, therefore, applied if the PRC $Z(\theta)$ is obtained. According to the perturbation method introduced in Chap. 1, the PRC of the indirectly controlled combined rimless wheel is numerically achieved as follows:

(A1) Set $L_{\mathrm{d}} = 0$ [m] and utilize the parameters listed in Tab. 2.1 with the initial conditions:

$$\boldsymbol{q}(0) = \begin{bmatrix} \phi - \alpha & 0 \end{bmatrix}^{\mathrm{T}}, \qquad \dot{\boldsymbol{q}}(0) = \begin{bmatrix} 4 & 0 \end{bmatrix}^{\mathrm{T}}. \tag{4.3}$$

(A2) Start the dynamic locomotion until stable and obtain the natural frequency f_n [Hz].

(A3) Repeat (A1). In addition, change L_{d} to 0.02 [m] from d_0 [s] to d_f [s]. The reaction forces of dropping and raising the wobbling mass result in perturbations to the

system. Here the perturbation onset d_0 [s] equals the first collision timing after 100 [s] walking, and

$$\begin{aligned} d_f &= d_0 + d_\Delta, \\ d_\Delta &= \frac{T_n}{200}, \end{aligned} \tag{4.4}$$

where T_n [s] is the reciprocal of f_n [Hz].

(A4) As soon as the disturbed gait reconverge to stable, the phase shift ψ_s [rad] is computed as:

$$\psi_s = \frac{2\pi(t_p - t_n)}{T_n}, \tag{4.5}$$

where t_p [s] and t_n [s] denote collision timing in perturbation and natural conditions respectively.

(A5) Increase d_0 by d_Δ [s].

(A6) Repeat from (A3) to (A5) for 200 steps.

As shown in Fig. 4.1, the disturbed gait reconverges to stable after few steps. Despite the fact that L_c is also slightly disturbed by the foot collision, the perturbation applied leads to a phase shift between natural and typical gaits. Therefore the PRC is obtained numerically with 200 sample points in one cycle, which is normalized to $[0, 2\pi)$. As shown in Fig. 4.2, the indirectly controlled limit cycle walker is only sensitive to the perturbations soon before collision timings.

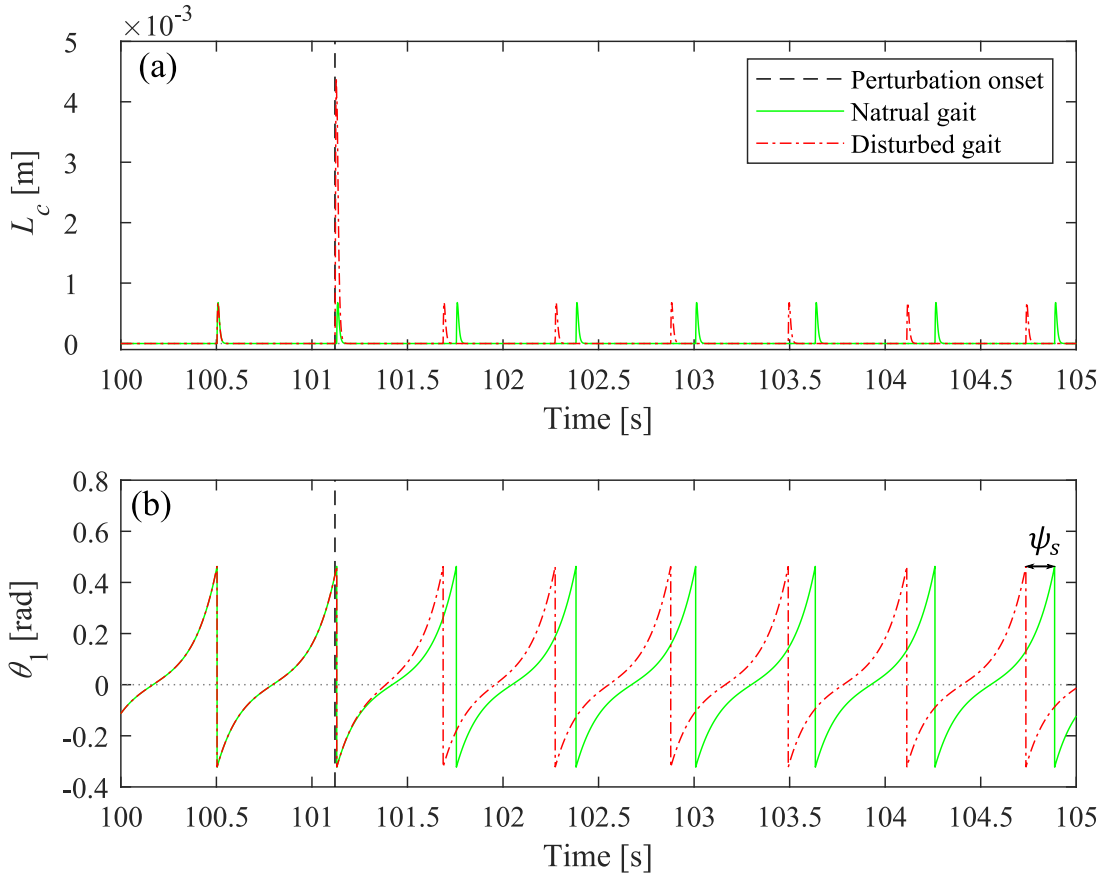

Figure 4.1: Perturbation and phase shift

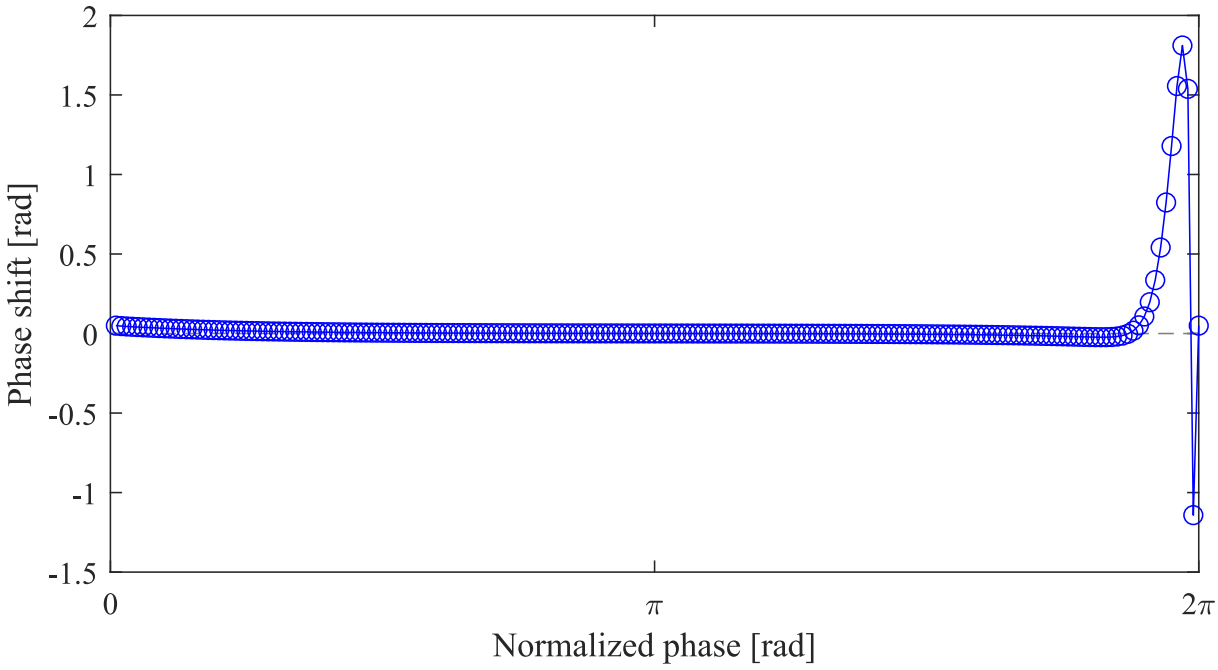

Figure 4.2: Phase response curve

4.3 Entrainment Waveform Optimization

4.3.1 Entrainment range maximization

The basic formulas for maximizing the entrainment range with a given PRC have been introduced in [29]. Here, the formulas are applied to this indirectly controlled limit cycle walker.

With the definition of $\Phi := \theta - 2\pi f_c t$ and $f_\Delta := f_n - f_c$, where Φ and f_Δ denote the phase difference and frequency difference between the limit cycle walker and the wobbling mass respectively, Eq. (4.2) is simplified as:

$$\dot{\Phi} = 2\pi f_\Delta + \Gamma(\Phi), \tag{4.6}$$

$$\Gamma(\Phi) = \langle Z(\Theta + \Phi)F(\Theta)\rangle, \tag{4.7}$$

where $\Theta := 2\pi f_c t$ and $\langle\cdot\rangle$ denotes averaging by Θ over 2π. The entrainment effect occurs when the phase difference is a constant, *i.e.*, $\dot{\Phi} = 0$. The entrainment range $R_f[F]$ is therefore equivalent to the difference between $\Gamma(\Phi_{\max})$ and $\Gamma(\Phi_{\min})$:

$$R_f[F] = \Gamma(\Phi_{\max}) - \Gamma(\Phi_{\min}). \tag{4.8}$$

By introducing a constraint that the total power $E_f = \langle F(\Theta)^2\rangle$ takes a constant value, this chapter seeks for the optimal entrainment waveform F_r^* which maximizes the following cost function:

$$\Sigma[F] = R_f[F] - \sigma(\langle F^2\rangle - E_f), \tag{4.9}$$

where σ is the Lagrange multiplier. With the maximized entrainment range, the F_r^*, which is capable of entraining the walker to a higher frequency, has the best performance among all possible forcing functions. Since the step length is constant, *i.e.*, the walking frequency is proportional to velocity. By ensuring that the first variation $\delta\Sigma$ vanishes and the second variation $\delta^2\Sigma$ is negative, the F_r^* emerges as:

$$F_r^*(\Theta) = (2\sigma)^{-1}\{Z(\Theta + \Phi_{\max}) - Z(\Theta + \Phi_{\min})\}. \tag{4.10}$$

To obtain F_r^*, the phases, $\Phi_{\max}$ and $\Phi_{\min}$, that maximize/minimize Γ, have to be determined. Define

$$Q_z := \langle\{Z(\Theta + \Phi_{\max}) - Z(\Theta + \Phi_{\min})\}^2\rangle, \tag{4.11}$$

and note that the optimal entrainment waveform has zero average, *i.e.*, $\langle F_r^* \rangle = 0$:

$$\Gamma(\Phi) = \sqrt{\frac{E_f}{Q_z}} \langle Z(\Theta + \Phi)\{Z(\Theta + \Phi_{\max}) - Z(\Theta + \Phi_{\min})\}\rangle. \tag{4.12}$$

The conditions for the maximum and minimum of Γ therefore become:

$$\Gamma'(\Phi_{\max,\min}) = 0, \quad \Gamma''(\Phi_{\max}) < 0, \quad \Gamma''(\Phi_{\min}) > 0, \tag{4.13}$$

where the solution for the first condition combined with Eq. (4.12) gives:

$$\langle Z'(\Theta + \Phi_{\max}) Z(\Theta + \Phi_{\min})\rangle = \langle Z'(\Theta + \Phi_\Delta) Z(\Theta)\rangle = 0, \tag{4.14}$$

where $\Phi_\Delta = \Phi_{\max} - \Phi_{\min}$, and $Z'(\Theta)$ is the first order derivative of $Z(\Theta)$ obtained numerically:

$$Z'(\Theta) = \frac{Z(\Theta + \Theta_\Delta) - Z(\Theta)}{\Theta_\Delta}, \tag{4.15}$$

where Θ_Δ is a small increment of the phase. Therefore, the Φ_Δ can be obtained by finding the zero-crossing points of Eq. (4.14), and the optimal entrainment waveform $F_r^*(\Theta)$ is achieved accordingly as shown in Fig. 4.3.

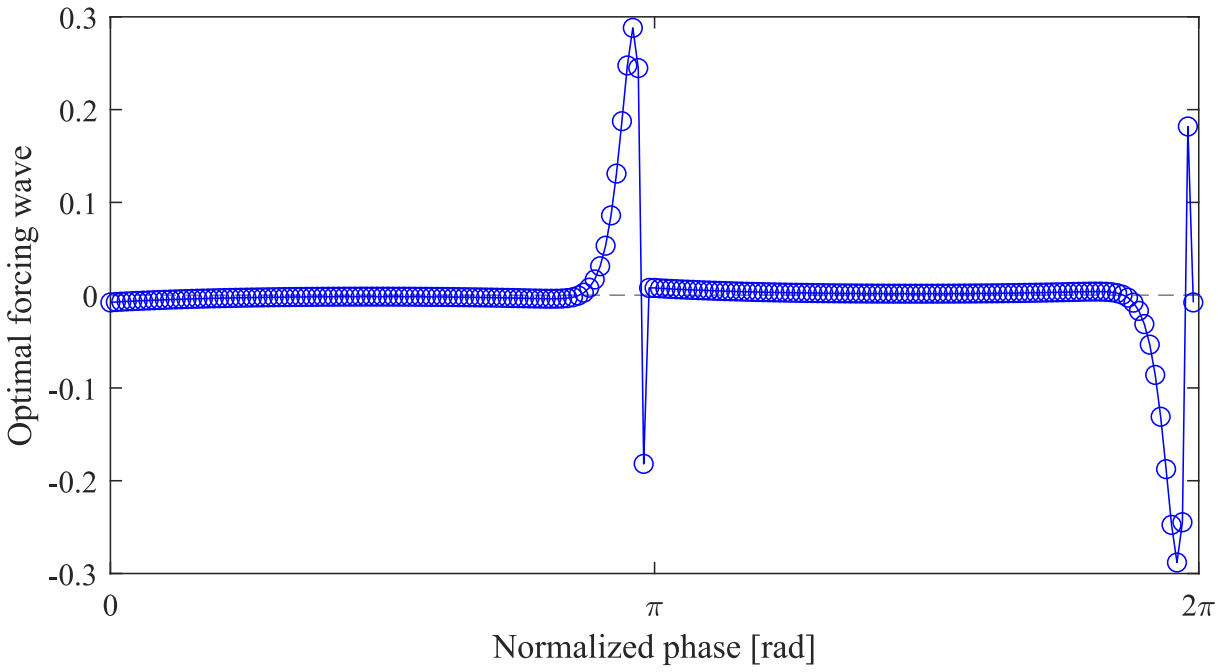

Figure 4.3: Optimal waveform for entrainment

4.3.2 Extension to $m:1$ entrainment

The obtained optimal entrainment waveform is the desired input which maximized the entrainment range of $1:1$ entrainment. One important extension which entrains the locomotion with smaller forcing energy is $m:n$ entrainment where $m \geq 2, n = 1$, *i.e.*, during m cycles walking, the wobbling mass makes only one cycle.

An ideal solution can be achieved by making m copies of the optimal entrainment waveform F_r^* and adding a slight perturbation to the m copies F_r^* which makes it become $F_{r(m:1)}^*$, the generated $F_{r(m:1)}^*$ therefore has only one period. The $F_{r(m:1)}^*$ will become the optimal entrainment waveform for $m:1$ entrainment if the condition $\langle {F_{r(m:1)}^*}^2 \rangle = E_f$ is satisfied. An example of generating $F_{r(2:1)}^*$ is shown in Fig. 4.4, the perturbation here is simply defined as amplifying the first half part 5/4 times and compressing the second half part 4/5 times.

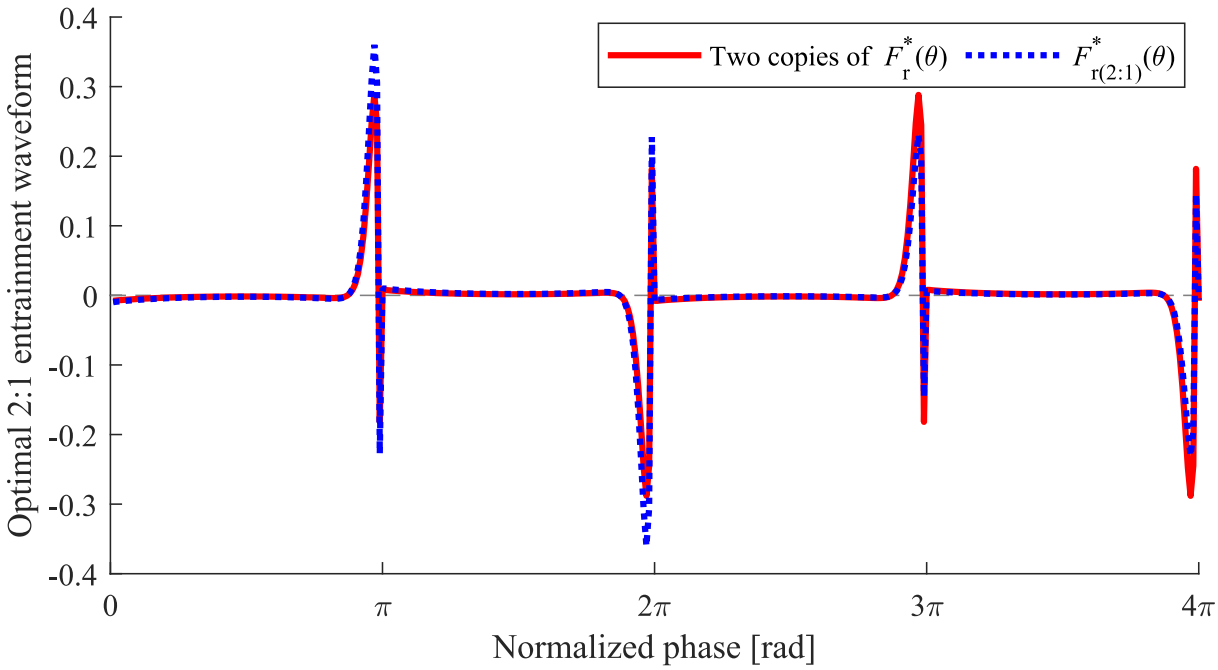

Figure 4.4: Optimal waveform for 2:1 entrainment

Table 4.1: Two cases for PD gains of CRW

	K_{D} [s^{-1}]	K_{P} [s^{-2}]
Case 1	60	900
Case 2	200	10000

4.4 Typical Gait Analysis

Here, the typical gait of the CRW indirectly controlled by setting the desired wobbling trajectory L_{d} to the optimal entrainment waveform F_r^* is observed. The parameters listed in Tab. 2.1 (in Chap. 2) were used for simulation, and Eq. (4.3) were used as the initial condition. In addition, the wobbling amplitude and wobbling frequency are set to $A_m = 0.01$ [m] and $f_c = 1.65$ [Hz]. Since the obtained F_r^* is unsmooth, different PD control gains may lead to different results. Therefore two cases of PD control gains are applied from Tab. 4.1 and the results are shown in Fig. 4.5 and Fig. 4.6 respectively.

As shown in Fig. 4.5, the low PD control gains do not enable L_c to pursue L_{d} accurately (there is a discrepancy between the shape in Fig. 4.5(a) and Fig. 4.3) , therefore L_c becomes a relative smoothed waveform. In Fig. 4.5(c), the vertical ground reaction force varies dramatically, nevertheless satisfies the holonomic constraint (λ_2 is always positive), benefit from the smoothness of L_c.

In contrast with Fig. 4.5, as shown in Fig. 4.6, the high PD control gains achieve $L_c \to L_{\mathrm{d}}$ (the shape in Fig. 4.6(a) and Fig. 4.3 are consistent), results in a sharp waveform, whereas the holonomic constraint is unsatisfied due to the violent L_c shown in Fig. 4.6(c).

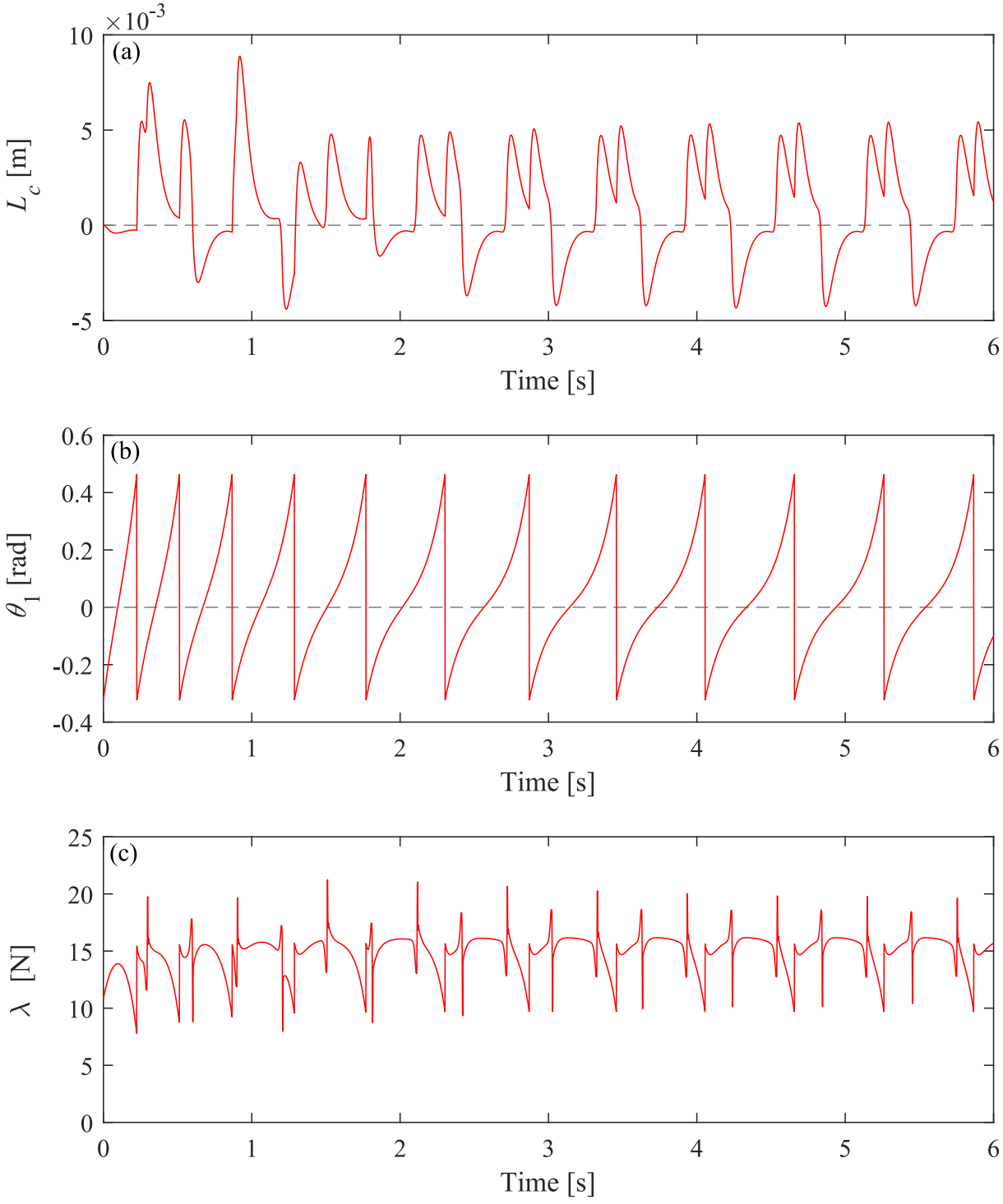

Figure 4.5: Typical gait with low PD gains

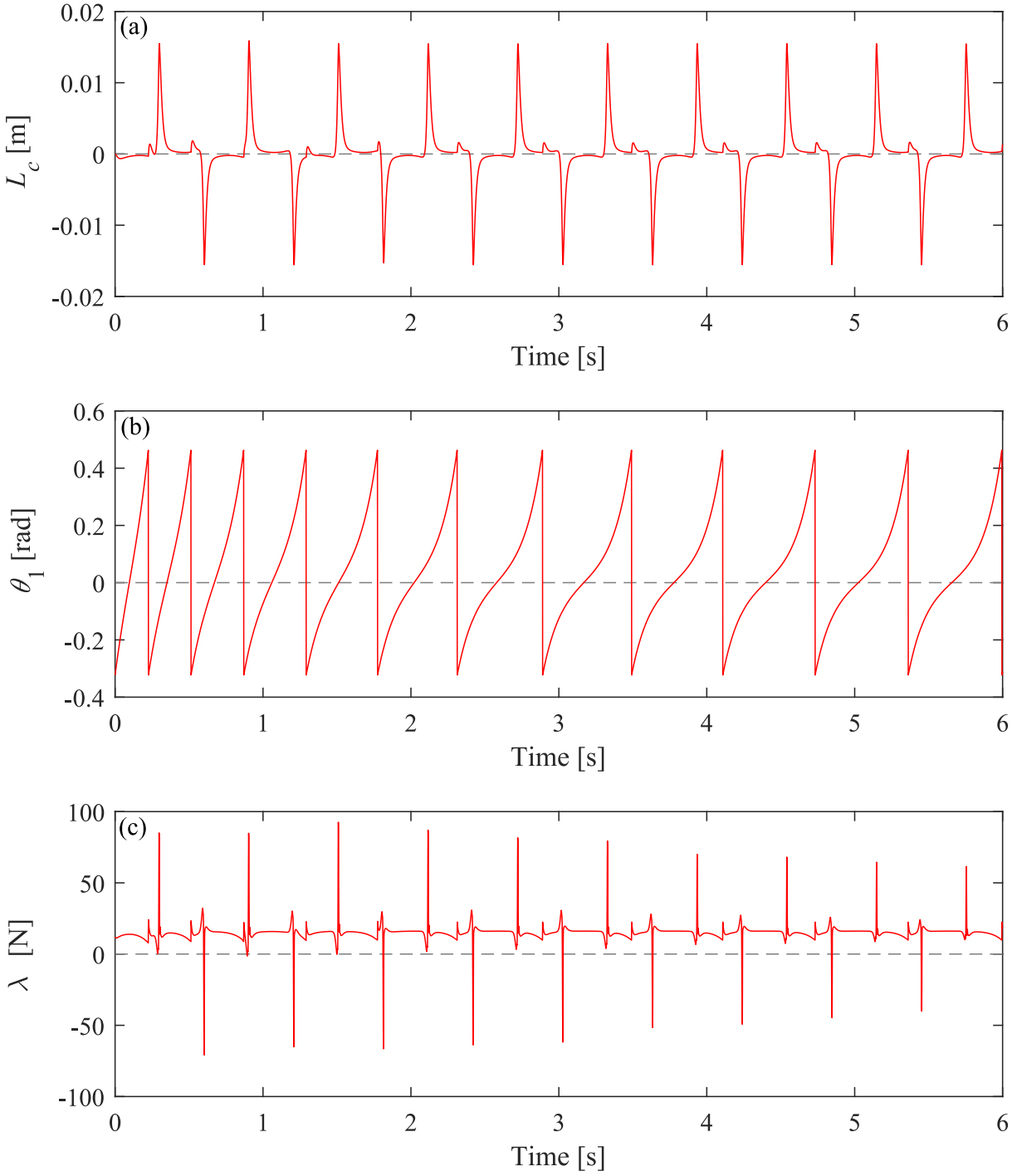

Figure 4.6: Typical gait with high PD gains

4.5 Evaluation

To evaluate the entrainability, Arnold tongue is obtained to compare the entrainment ranges. The entrainability of Z, F_r^*, $F_{r(2:1)}^*$ with sine wave function $F_{\sin}$ are compared. To make easy evaluation, This chapter focuses on $1:1$ and $2:1$ entrainments of Arnold tongues.

To make fair comparison, a convenient practical way is set to:

$$\langle {F_{\sin}}^2 \rangle = \langle Z^2 \rangle = \langle {F_{r(2:1)}^*}^2 \rangle = \langle {F_{r(2:1)}^*}^2 \rangle. \tag{4.16}$$

Therefore the power of the 4 kinds of entrainment waveform are normalized to equal, the amplitude of Z, F_r^* and $F_{r(2:1)}^*$ can be calculated from $F_{\sin}$.

Then the parameters listed in Tab. 2.1 (in Chap. 2), and the low PD control gains listed in Tab. 4.1 are used to conduct the following simulations. In the case of Z, F_r^* and $F_{r(2:1)}^*$, the Eq. (4.3) was used as the initial state, whereas in the case of $F_{\sin}$, following initial state were used to avoid excessive initial control input at the beginning of walking.

$$\boldsymbol{q}(0) = \begin{bmatrix} \phi - \alpha & 0 \end{bmatrix}^{\mathrm{T}}, \qquad \dot{\boldsymbol{q}}(0) = \begin{bmatrix} 4 & 2\pi f_c A_m \end{bmatrix}^{\mathrm{T}} \tag{4.17}$$

To stabilize the gait, an empirical method is adjusting the wobbling frequency both forward and backward starting from the natural frequency of the walker, and use the last state of the previous succeed gait as the initial state of the following trial. Then the simulation is conducted as follows:

(B1) Set the desired wobbling amplitude A_m to 0.00025 [m].

(B2) Set the desired wobbling frequency f_c to the natural frequency f_n obtained in section III (about 1.63 [Hz]).

(B3) Set the initial state as Eq. (4.3) or Eq. (2.18) (in Chap. 2) in the case of Z, F_r^*, $F_{r(2:1)}^*$ or $F_{\sin}$ respectively, and start dynamic walking.

(B4) After 100 [s] of walking, save f_w for 20 steps.

(B5) For the forward process, increase f_c by 0.005 [Hz]. If the gait succeeds, use the last state as the initial state and return to (B4), otherwise return to (B3). On the other hand, for the backward process, decrease f_c by 0.005 [Hz] and update the initial state similarly.

(B6) Repeat from (B3) to (B5) until $f_c = 2$ [Hz] in forward process and $f_c = 0.6$ [Hz] in backward process.

(B7) Increase A_m by 0.00025 [m] and return to (B2).

(B8) Repeat from (B2) to (B7) until $A_m = 0.01$ [m].

(B9) Combine the results obtained from forward and backward process.

The f_w is therefore obtained within the range of $A_m = 0.00025 : 0.00025 : 0.01$ [m], $f_c = 0.6 : 0.005 : 2$ [Hz] through a relative stable parameter adjusting process.

Typical Arnold tongues are shown in Fig. 4.7-4.10, and the boundaries of them are estimated via linear regression by using the outermost points of them. To further quantify the entrainability, the entrain rate defined as follows is obtained:

$$\gamma_{\mathrm{er}} = \frac{p_{\mathrm{e}}}{p_{\mathrm{t}}}, \tag{4.18}$$

where p_{e} and p_{t} denote the total entrained points on the accordingly Arnold tongue and the total simulation trials. The calculated rate is shown in Fig. 4.11.

In the case of the walker with the wobbling trajectory as $F_{\sin}$, the entrainment ranges of both $1:1$ and $2:1$ entrainment are very narrow. In the case of the walker with the entrainment waveform as F_r^*, the entrainment range of $1:1$ entrainment becomes the widest among the 4 entrainment waveform. In the case of the walker with the entrainment waveform as $F_{r(2:1)}^*$, the entrainment range of $1:1$ entrainment becomes a little narrower, whereas the entrainment range of $2:1$ entrainment becomes the widest among the 4 entrainment waveform. It is worth mentioning that in the case of walker with the entrainment waveform as Z, which becomes a suboptimal policy for both $1:1$ and $2:1$ Arnold tongues. The results indicate that the entrainment range can be magnified by applying a phase dependent forcing function, and the specific Arnold tongue can be maximized by manipulating the PRC accordingly.

Notice that the derivation of the optimal entrainment waveform does not take some physical constraints, *e.g.*, positive vertical ground reaction force, into account. Therefore the Arnold tongues are already narrowed by the constraints. Reducing the weight of the wobbling mass will improve the stability of the entrainment range.

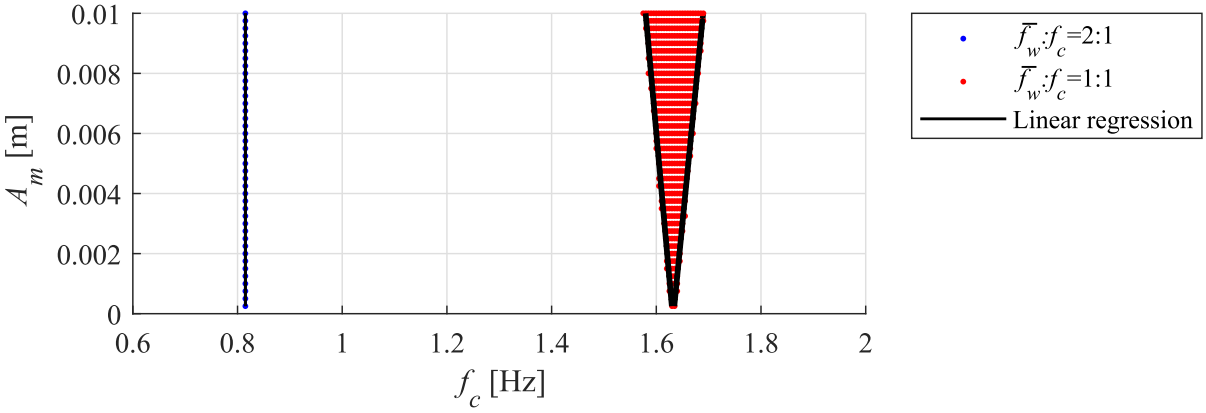

Figure 4.7: Arnold tongue of sine wave input

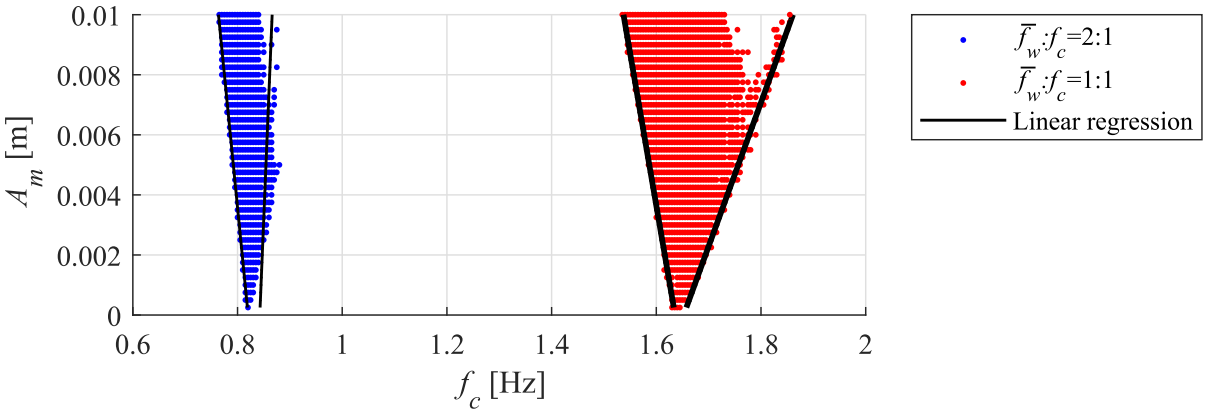

Figure 4.8: Arnold tongue of phase response curve

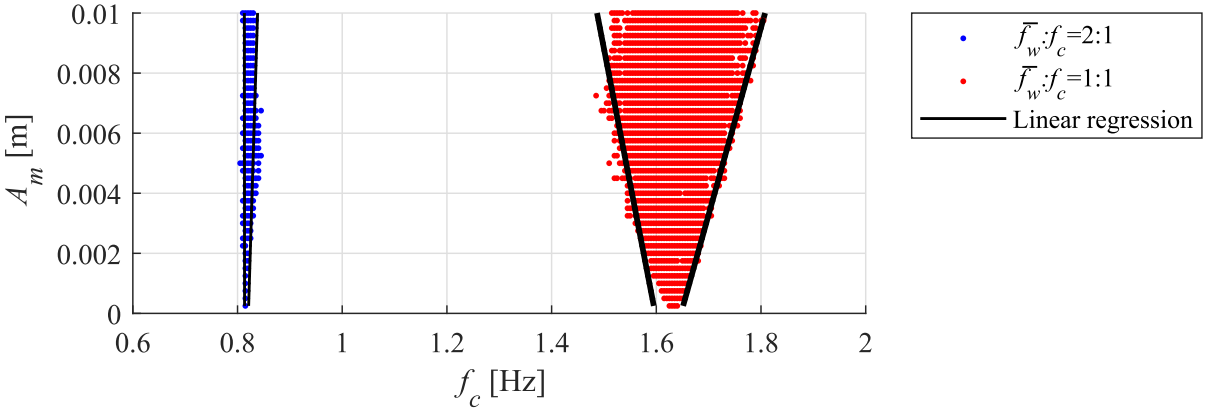

Figure 4.9: Arnold tongue of F_r^*

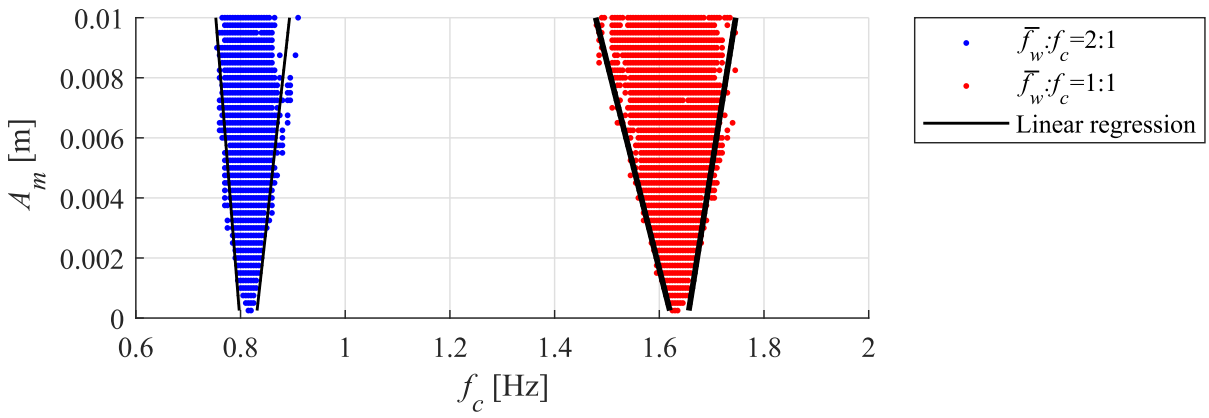

Figure 4.10: Arnold tongue of $F^*_{r(2:1)}$

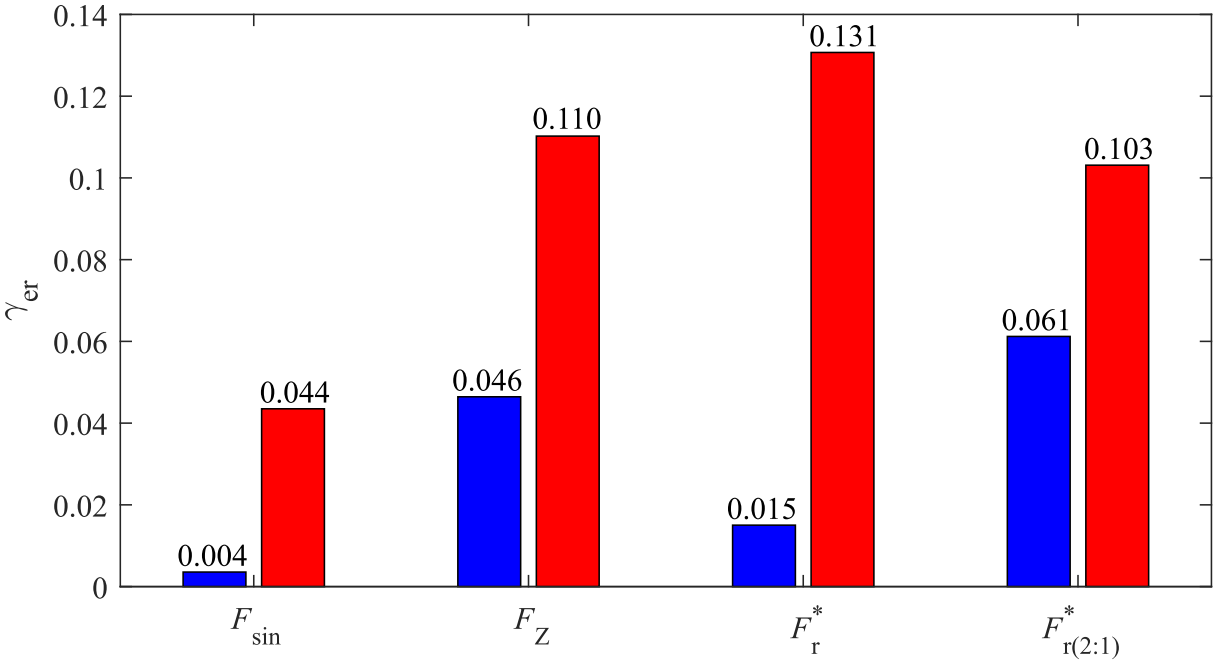

Figure 4.11: Entrain rate

4.6 Summary and Discussions

In this chapter, an optimal entrainment waveform for the indirectly controlled locomotion robots is derived using CRW as a simple example under the criterion of maximizing the entrainment range with fixed energy, based on the phase reduction theory. As an extension, an example of $m : 1$ entrainment is further obtained. The method can be not only extended to active walking on level ground [33] [34], but also applied to more complicated underactuated robots.

Chapter 5

Locomotion Generation and Analysis of an Indirectly Controlled Sliding Locomotion Robot

5.1 Introduction

Theoretical analysis and experimental verification of indirectly controlling mechanism have been conducted using CRW as a simple example. Moreover, the optimal waveform, which maximizes the entrainment range with fixed energy is obtained, has been derived to reduce the forcing energy. On the other hand, the ground condition assumed in the previous chapters is the most simple condition for locomotion, *i.e.*, the friction coefficient of the ground contacting is large enough to avoid slipping during the locomotion. To show the advantage of the indirectly controlling method, this dissertation aims to achieve stable and efficient locomotion on the slippery surface, which is one of the most difficult terrains for locomotion robots to overcome, using this control method.

Instead of using walking robots stepping with legs, this dissertation applies indirectly controlling mechanism on a novel seed-like robot proposed in previous study [35]. This underactuated robot generates sliding locomotion on slippery downhill by means of body rotation, benefited from its arc-shaped configuration, which facilitates the periodicity and stability of the locomotion [36] [37]. A substantial advantage of this robot is that it positively utilizes the sliding locomotion, which is generally considered to be harmful to

the walking robots. To extend this sliding locomotion on level ground, an active wobbling mass with up and down motion is attached to the robot body in this chapter. This indirectly controlled robot not only achieves stable and efficient sliding locomotion on level ground, but also has a great tendency to adapt to more hostile environments by combination or cooperating with other robots.

This chapter is organized as follows. First, the equations of dynamics and control is derived in Section 2. Second, typical sliding locomotion is numerically simulated in Section 3. In addition, parametric study is conducted to see the whole structure. Third, Section 4 performs nonlinear analysis to investigate the relationship between achieving efficient locomotion and being entrained. Moreover, synchronization phenomenon is analyzed via hysteresis plot to further interpret the unusual shapes of the Arnold tongues. Fourth, an analysis from the mechanical energy dissipation point of view is conducted in Section 5. Finally, Section 6 is devoted to summary and discussions.

5.2 Dynamics and Control

5.2.1 Equation of motion

The indirectly controlled sliding locomotion robot is illustrated in Fig. 5.1. This underactuated robot consists of two identical arc-shaped body frames whose radius is R [m] and an actively controlled wobbling mass. Here, $(x,\ z)$ is the position of the center of the bottom, θ_1 is the angular position of the body regard to vertical. θ_{c}, which is a constant, denotes the angular position of the wobbling mass regard to vertical midline of the robot. In addition, l_0 [m] is the length between the center of mass (CoM) and the center of the bottom, l_2 [m] is the length of the wobbling mass and l_1 [m] is the distance between the origin of wobbling mass (when $l_2 = 0$) and CoM. Moreover, the mass is of the main body is m_1 [kg] and the inertial moment about it is I_1 [$\mathrm{kg \cdot m^2}$], the wobbling mass is m_2 [kg] and its inertia moment is I_2 [$\mathrm{kg \cdot m^2}$].

Let $\boldsymbol{q} = \begin{bmatrix} x\ z\ \theta_1\ l_2 \end{bmatrix}^{\mathrm{T}}$ be the generalized coordinate vector. The robot equation of motion then becomes:

$$\boldsymbol{M}\ddot{\boldsymbol{q}} + \boldsymbol{h} = \boldsymbol{J}^{\mathrm{T}}\lambda + \boldsymbol{J}_{\mu}^{\mathrm{T}}\lambda + \boldsymbol{S}u, \tag{5.1}$$

where $\boldsymbol{M}$ represents the inertia matrix, $\boldsymbol{h}$ represents the combination of centrifugal force,

Coriolis force and gravity terms.

On the right-hand side, $\boldsymbol{J}^{\mathrm{T}}\lambda$ is the holonomic constraint, $\boldsymbol{J}_{\mu}^{\mathrm{T}}\lambda$ is the friction force term. In addition, u is the control input which raises and drops the wobbling mass, and

$$\boldsymbol{S} = \begin{bmatrix} 0 & 0 & 0 & 1 \end{bmatrix}^{\mathrm{T}}, \tag{5.2}$$

is the driving vector respectively.

The grounding point of the robot is:

$$\begin{bmatrix} x_{\mathrm{c}} \\ z_{\mathrm{c}} \end{bmatrix} = \begin{bmatrix} x + R\sin\theta_1 \\ z + R(\cos\theta_1 - 1) \end{bmatrix}, \tag{5.3}$$

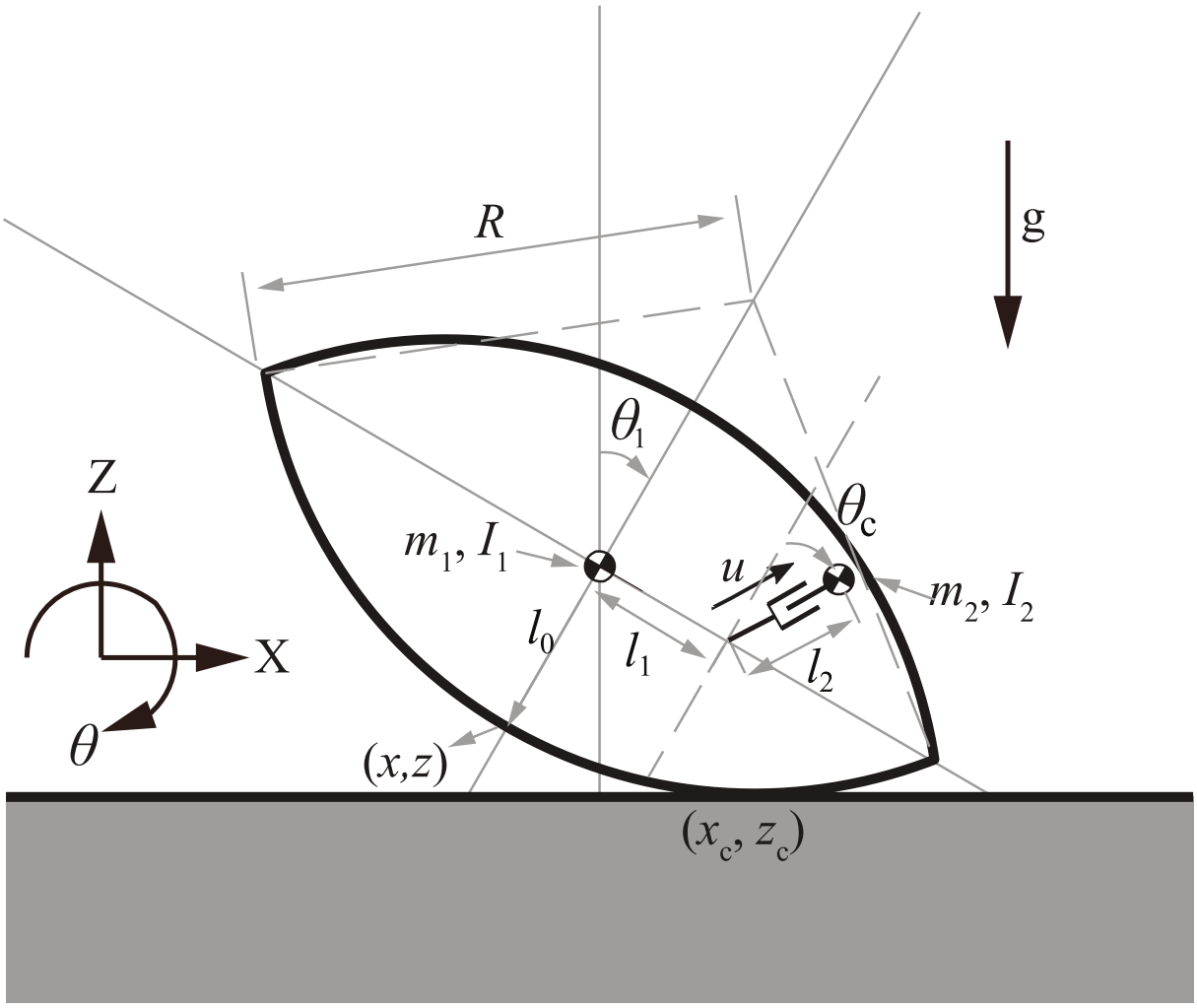

Figure 5.1: Indirectly controlled sliding locomotion robot model

where the time derivative becomes:

$$\frac{\mathrm{d}}{\mathrm{d}t}\begin{bmatrix} x_\mathrm{c} \\ z_\mathrm{c} \end{bmatrix} = \begin{bmatrix} \dot{x} + R\dot{\theta_1}\cos\theta_1 \\ \dot{z} - R\dot{\theta_1}\sin\theta_1 \end{bmatrix}. \tag{5.4}$$

To guarantee the horizontal sliding locomotion, the following velocity constraint should be satisfied:

$$\dot{z_\mathrm{c}} = \dot{z} - R\dot{\theta_1}\sin\theta_1 = 0, \tag{5.5}$$

therefore,

$$\begin{bmatrix} 0 & 1 & -R\sin\theta_1 & 0 \end{bmatrix}\dot{\boldsymbol{q}} = \boldsymbol{J}\dot{\boldsymbol{q}} = 0. \tag{5.6}$$

When the angular position increases to $\theta_{\max}$ (or decreases to $-\theta_{\max}$) as shown in Fig. 5.2, the edge constraint will no longer be satisfied, where $\theta_{\max}$ is calculated as follows:

$$\theta_{\max} = \arccos\frac{R - l_0}{R}, \tag{5.7}$$

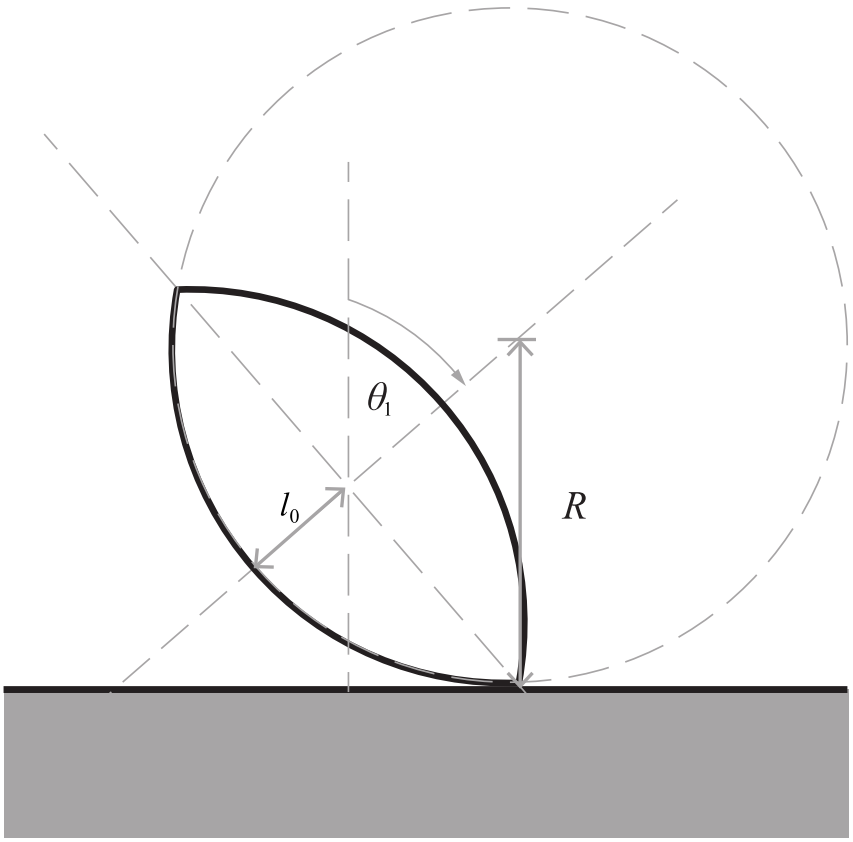

Figure 5.2: Edge constraint

5.2.2 Ground reaction force

The ground reaction force λ [N] is the simultaneous solution of Eqs. (5.1) and (5.6):

$$\begin{aligned} \lambda &= -X^{-1}\left(\boldsymbol{J}\boldsymbol{M}^{-1}(\boldsymbol{S}u-\boldsymbol{h})+\dot{\boldsymbol{J}}\dot{\boldsymbol{q}}\right), \\ X &:= \boldsymbol{J}\boldsymbol{M}^{-1}\hat{\boldsymbol{J}}^{\mathrm{T}},\ \hat{\boldsymbol{J}} := \boldsymbol{J}+\boldsymbol{J}_{\mu}. \end{aligned} \tag{5.8}$$

Positive ground reaction force is required to generate stable sliding locomotion. By substituting Eq. (5.8) into Eq. (5.1), following equations can be obtained:

$$\begin{aligned} \ddot{\boldsymbol{q}} &= \boldsymbol{M}^{-1}(\boldsymbol{Y}(\boldsymbol{S}u-\boldsymbol{h})-\hat{\boldsymbol{J}}^{\mathrm{T}}X^{-1}\dot{\boldsymbol{J}}\dot{\boldsymbol{q}}), \\ \boldsymbol{Y} &:= \boldsymbol{I}_4-\hat{\boldsymbol{J}}^{\mathrm{T}}X^{-1}\boldsymbol{J}\boldsymbol{M}^{-1}, \end{aligned} \tag{5.9}$$

where $\boldsymbol{I}_4$ is the identity matrix of order 4.

5.2.3 Coulomb friction force

Coulomb friction force, defined correspond to the λ, is assumed between the robot and the surface ground, which is opposite to the direction of sliding velocity. Define μ as the frictional coefficient, the sliding frictional force vector becomes $\begin{bmatrix}\mu & 0 & 0 & 0\end{bmatrix}^{\mathrm{T}}\lambda$, the rotational moment generated by the friction force is calculated as the following outer product:

$$\begin{bmatrix} x_{\mathrm{c}}-x \\ y_{\mathrm{c}}-y \\ z_{\mathrm{c}}-z \end{bmatrix} \times \begin{bmatrix} \mu \\ 0 \\ 0 \end{bmatrix} \lambda = \begin{bmatrix} 0 \\ \mu R(\cos\theta_1-1) \\ 0 \end{bmatrix} \lambda. \tag{5.10}$$

The second component on right-hand side is the rotational moment for the θ_1, therefore, the Coulomb friction force becomes:

$$\boldsymbol{J}_{\mu}^{\mathrm{T}}\lambda = \begin{bmatrix}\mu & 0 & \mu R(\cos\theta_1-1) & 0\end{bmatrix}^{\mathrm{T}}\lambda. \tag{5.11}$$

The frictional coefficient μ determined by the grounding point velocity is defined as:

$$\mu = -\mu_0\mathrm{sign}(\dot{x_{\mathrm{c}}}-R\dot{\theta_1}) = -\mu_0\mathrm{sign}(\dot{x}+R\dot{\theta_1}(\cos\theta_1-1)), \tag{5.12}$$

where μ_0 is a positive constant which determined by material property. To avoid chattering about $\mu = 0 \Longleftrightarrow \dot{x} = R\dot{\theta_1}(1 - \cos\theta_1)$, Eq. (5.12) is smoothed by tanh function

$$\mu = -\mu_0 \tanh(s(\dot{x} + R\dot{\theta_1}(\cos\theta_1 - 1))), \tag{5.13}$$

where s is a positive constant adjusts the sharpness of tanh.

5.2.4 Output tracking control

Let $l_2 = \boldsymbol{S}^{\mathrm{T}}\boldsymbol{q}$ be the control output. The second order derivative of l_2 with respect to time becomes

$$\ddot{l_2} = \boldsymbol{S}^{\mathrm{T}}\ddot{\boldsymbol{q}} = \boldsymbol{S}^{\mathrm{T}}\boldsymbol{M}^{-1}\left(\boldsymbol{Y}(\boldsymbol{S}u - \boldsymbol{h}) - \hat{\boldsymbol{J}}^{\mathrm{T}}X^{-1}\dot{\boldsymbol{J}}\dot{\boldsymbol{q}}\right) = Au - B, \tag{5.14}$$

where

$$\begin{aligned} A &:= \boldsymbol{S}^{\mathrm{T}}\boldsymbol{M}^{-1}\boldsymbol{Y}\boldsymbol{S}, \\ B &:= \boldsymbol{S}^{\mathrm{T}}\boldsymbol{M}^{-1}\left(\boldsymbol{Y}\boldsymbol{h} + \hat{\boldsymbol{J}}^{\mathrm{T}}X^{-1}\dot{\boldsymbol{J}}\dot{\boldsymbol{q}}\right). \end{aligned}$$

To enable a periodic and smooth forcing waveform, the desired trajectory of the wobbling mass is set to

$$l_{2\mathrm{d}}(t) = A_m \sin(2\pi f_c t), \tag{5.15}$$

where A_m [m] and f_c [Hz] are the desired wobbling amplitude and frequency. Consequently, the control input for enabling l_2 to track $l_{2\mathrm{d}}(t)$ is defined as

$$u = A^{-1}(v + B), \tag{5.16}$$

$$v = \ddot{l}_{2\mathrm{d}}(t) + K_{\mathrm{D}}(\dot{l}_{2\mathrm{d}}(t) - \dot{l}_2) + K_{\mathrm{P}}(l_{2\mathrm{d}}(t) - l_2), \tag{5.17}$$

where K_{D} [s^{-1}] and K_{P} [s^{-2}] are the PD control gains.

Table 5.1: Physical and control parameters for seed-like sliding locomotion robot

m_1	1.0	kg
m_2	0.5	kg
I_1	0.10	kg·m^2
I_2	0.00	kg·m^2
l_0	0.3	m
R	0.8	m
l_1	0.4	m

θ_c	$\pi/6$	rad
g	9.81	m/s^2
K_D	40	s^{-2}
K_P	400	s^{-1}
μ_0	0.1	
s	20000	
A_m	0.01	m
f_c	2.5	Hz

5.3 Gait Analysis of Indirectly Controlled Sliding Locomotion Robot

5.3.1 Typical gait

Numerical simulation of the sliding locomotion is conducted using the parameters listed in Table 5.1, and the initial conditions are set to

$$\boldsymbol{q}(0) = \begin{bmatrix} 0 & 0 & 0 & 0 \end{bmatrix}^{\mathrm{T}}, \qquad \dot{\boldsymbol{q}}(0) = \begin{bmatrix} 0 & 0 & 0 & 2\pi A_m f_c \end{bmatrix}^{\mathrm{T}}. \tag{5.18}$$

Fig. 5.3 shows the simulation results of indirectly controlled sliding locomotion on slippery level road surface. From Fig. 5.3(a), we can see that forward sliding locomotion is generated successfully. The rotation angle of the robot in Fig. 5.3(b) keeps positive, indicates that the grounding point is always on the right bottom of the body. Fig. 5.3(c) shows that the trajectory of the active wobbling mass follows the desired sinusoidal wave. The instantaneous horizontal velocity varies between negative and positive as shown in Fig. 5.3(d), a concentrated sliding direction is expected to improve the performance. Moreover, positive ground reaction force is guaranteed during the sliding locomotion as shown in Fig. 5.3(e). Fig. 5.4 shows the stick diagram of the locomotion, we can observe that the robot slides gradually, indirectly controlled by the active wobbling mass.

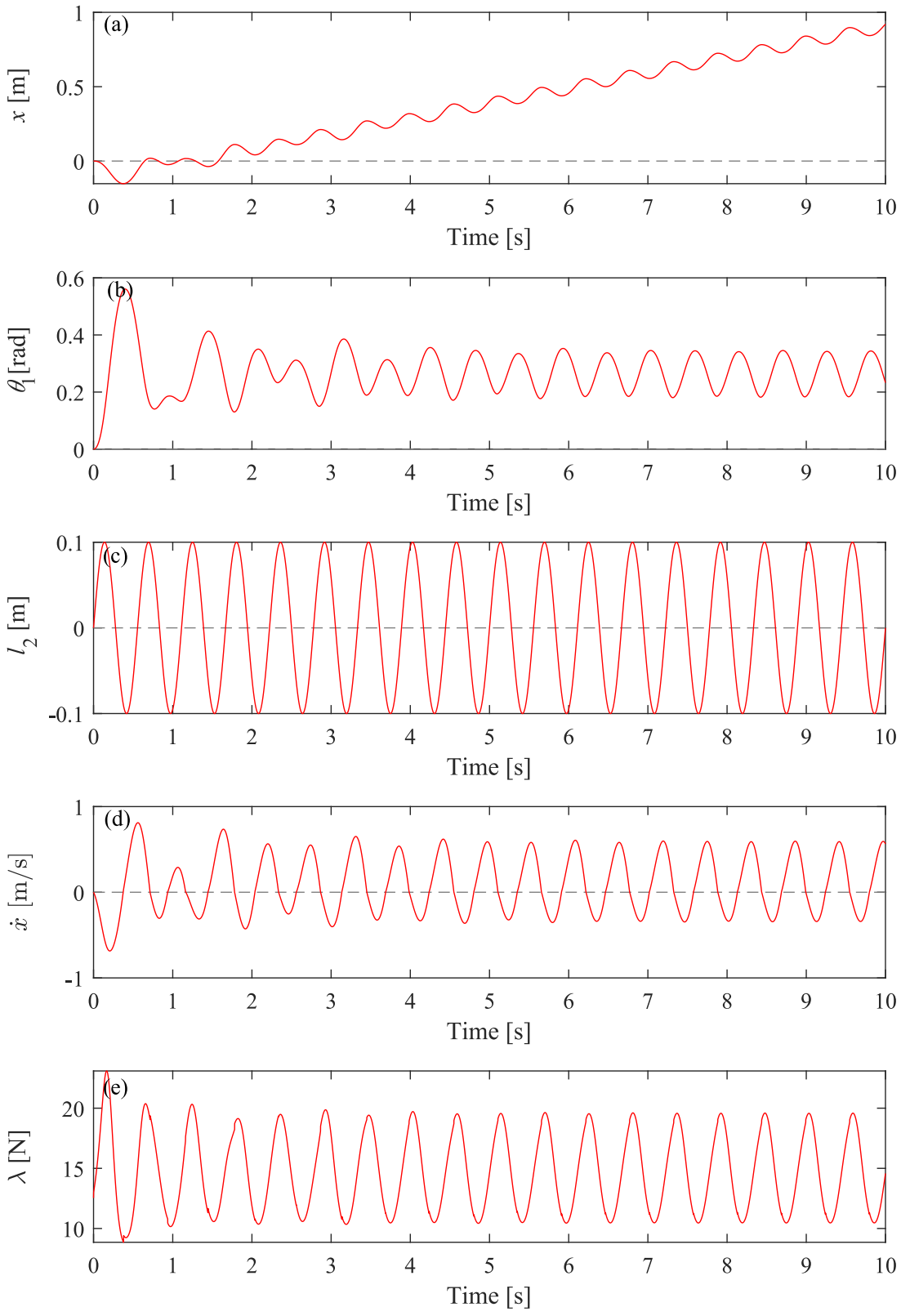

Figure 5.3: Typical locomotion of indirectly controlled sliding locomotion robot

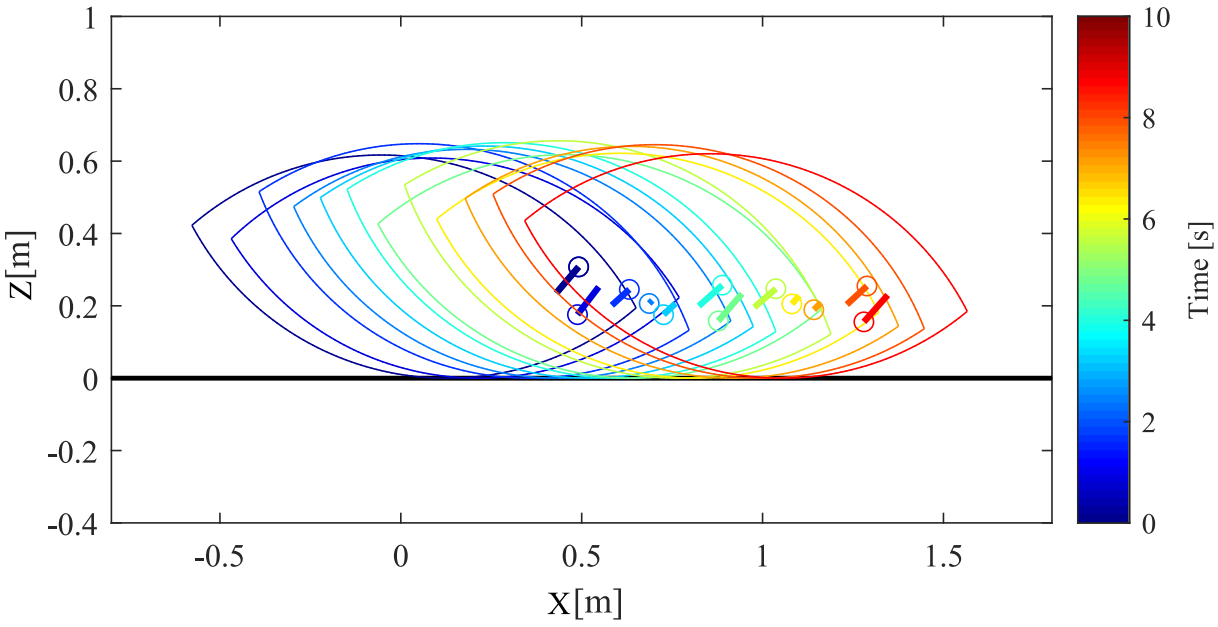

Figure 5.4: Stick diagram of indirectly controlled sliding locomotion on slippery surface

5.3.2 Parametric study

To observe the whole performance of the indirectly controlled sliding locomotion robot on the slippery surface, the horizontal velocity of the sliding locomotion and energy efficiency are evaluated though averaged velocity and specific resistance defined as follows:

$$V_x := \frac{f_c}{20} \int_{100}^{100+20/f_c} \dot{x}\ \mathrm{d}t, \tag{5.19}$$

$$\mathrm{SR} := \frac{p}{mg|V_x|}, \tag{5.20}$$

where

$$p := \frac{f_c}{20} \int_{100}^{100+20/f_c} |\dot{l_2}u| \mathrm{d}t, \qquad m := m_1 + m_2.$$

Therefore, V_x [m/s] and SR [-] denote the averaged horizontal velocity and specific resistance averaged in 20 wobbling periods respectively, and the physical meaning of SR is the required energy for 1 [kg] mass moves 1 [m].

Parameters listed in Table. 5.1 are used to conduct following process.

(A1) Set the wobbling amplitude $A_m = 0.005$[m].

(A2) Set the wobbling frequency $f_c = 0.5$ [Hz].

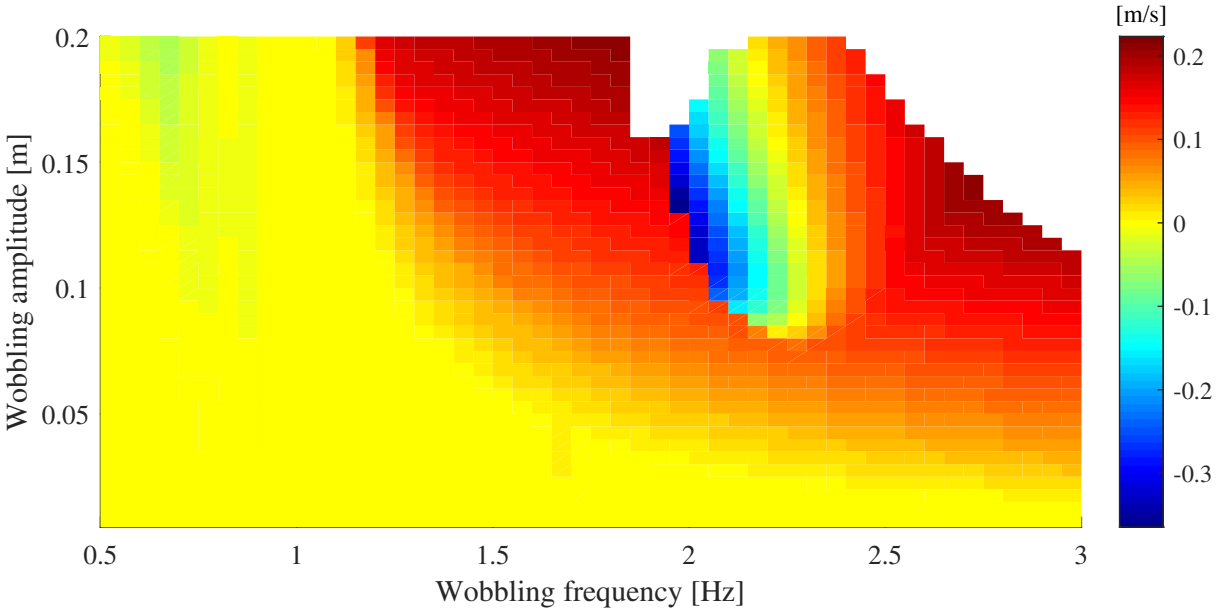

Figure 5.5: Horizontal velocity with respect to wobbling frequency and amplitude

(A3) Set the initial conditions to Eq. (5.18).

(A4) After 100 [s] of locomotion, average the horizontal velocity and specific resistance in 20 periods.

(A5) Increase f_c by 0.05 [Hz]and run the next simulation.

(A6) Repeat from (A3) to (A5) until $f_c = 3$ [Hz].

(A7) Increase A_m by 0.005 [m] and return to (A2).

(A8) Repeat from (A2) to (A7) until $A_m = 0.2$ [m].

Since the performance of SR traverse a large range, the value is normalized in the logarithmic scale. Consequently, the V_x and $\log_{10}\mathrm{SR}$ are obtained within the range of $A_m = 0.005 : 0.005 : 0.2$ [m], $f_c = 0.5 : 0.05 : 3$ [Hz].

The results are shown in Fig. 5.5 and Fig. 5.6. The white ranges imply the ground reaction force is negative or the edge constraint is unsatisfied. The high speed and energy efficient locomotion concentrate in certain parametric space except that the left small triangle is clean-cut in Fig. 5.6 whereas blur in Fig. 5.5. The rainbow-like part in Fig. 5.5 indicates variation in the direction of sliding locomotion, *i.e.*, backward and forward. The details are investigated in the following sections.

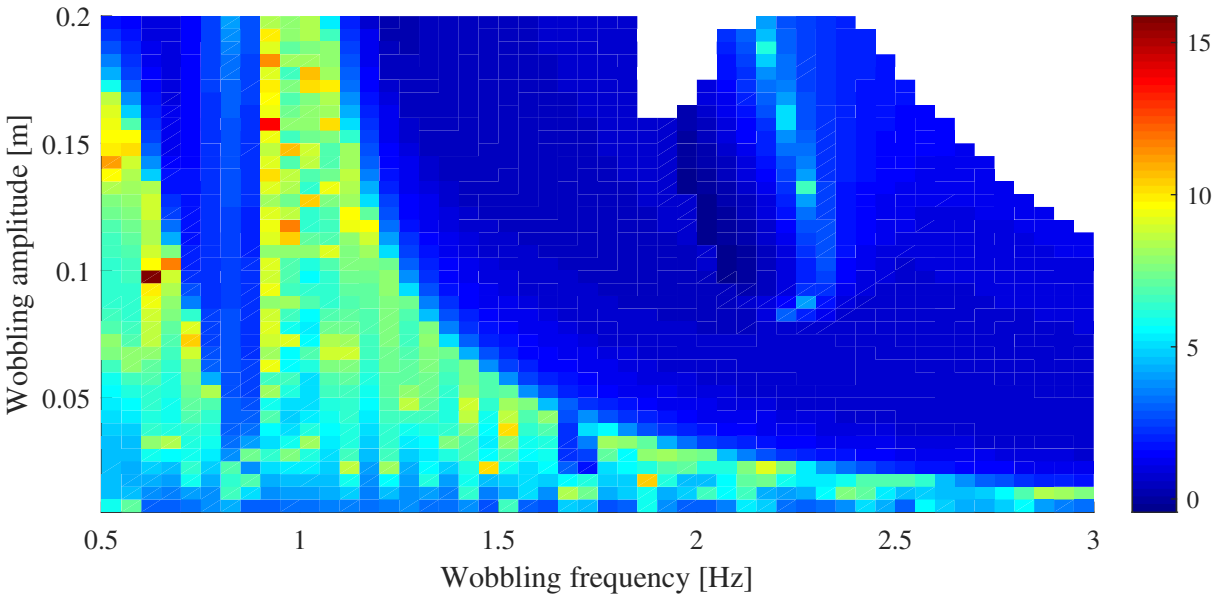

Figure 5.6: Logarithmic scaled specific resistance with respect to wobbling frequency and amplitude

5.4 Nonlinear Analysis

5.4.1 Arnold tongues

Since the overall entrained ranges can be shown by Arnold tongue. Numerical process is therefore conducted similar as obtaining the V_x and SR, except modifying (A4) to:
(B4) After 100 [s] of locomotion, save the rotation frequency f_r for 20 periods, where f_r is calculated by taking the inverse of the rotation period T_r. In addition, T_r is defined by the duration between the adjacent local minima of the angular position θ_1.

The Arnold tongues here focus on $1:1$ and $1:2$ entrainment which are dominant entrained ranges. The $1:n$ entrainment is defined by $\bar{f}_r : f_c = 1 : n$, where $n = 1, 2$ and $\bar{\cdot}$ denotes averaged over 20 periods.

The shapes of Arnold tongues (shown in Fig. 5.7) are highly consistent with the contour plot of horizontal velocity (shown in Fig. 5.5) and logarithmic scaled specific resistance (shown in Fig. 5.6). The results show the high dependency of the indirectly controlling sliding on the entrainment effect, since the unentrained ranges hardly generate horizontal locomotion, result in high specific resistance. On the other hand, it is worth noting that, unlike general cases, multiple Arnold tongues of the same entrainment ratio

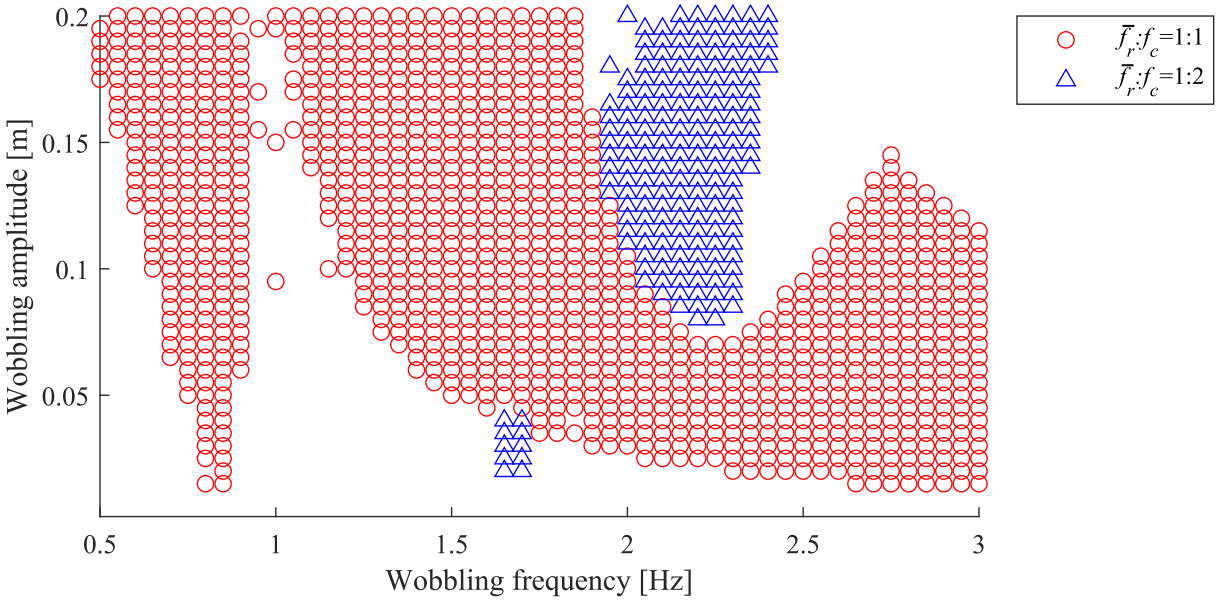

Figure 5.7: Arnold tongues with respect to wobbling frequency and amplitude

exist. The left 1 : 1 Arnold tongue, whose tip is around the natural frequency, is a typical Arnold tongue. In contrast, the typical 1 : 2 Arnold tongue, whose tip is around twice of the natural frequency is merged by another larger 1 : 1 Arnold tongue, which is unexpected, moreover, with one more 1 : 2 Arnold tongue inside, which is corresponding to the rainbow-like part in Fig. 5.5. In addition, the typical Arnold tongues are much smaller than the untypical Arnold tongues.

5.4.2 Synchronizations

Since the indirectly controlled sliding robot generates various locomotion, the detailed relationship is observed among frequency synchronization, horizontal velocity, as well as specific resistance through hysteresis plot. Here the wobbling amplitude is fixed to $A_m = 0.1$ [m] and the frequency of the wobbling motion is varied only. The gait descriptors f_r, V_x and $\log_{10}\mathrm{SR}$ are used to make evaluation the following process is conducted.

(C1) Set $f_c = 0.5$ (or 3) [Hz] and run the simulation with the initial conditions as Eq. (5.18).

(C2) After 100 [s] of locomotion, save f_r for 20 period of rotation and the averaged V_x, $\log_{10}\mathrm{SR}$.

(C3) Save the final state immediately after finishing the rotation period (local minimum).

(C4) Increase (or decrease) f_c by 0.01 [Hz] and run the next simulation by using the final state of (C3) as the initial state.

(C5) Repeat from (C2) to (C4) until $f_c = 3$ (or 0.5) [Hz].

The gait descriptors are therefore obtained through both backward and forward sweeping within the range of $f_c = 0.5 : 0.01 : 3$ [Hz]. The results are separated into 8 intervals as shown in Fig. 5.8, the interval (I) and (III) are desynchronized which could be ignored here. The interval (II) belongs to the small $1 : 1$ Arnold tongue, whereas the intervals (IV) and (VIII) belong to the large $1 : 1$ Arnold tongue. The interval (VI) belongs to the large $1 : 2$ Arnold tongue. (V) is the bistable interval which shows the existence of different steady locomotion in the same parametric space, extends 1:1 and 1:2 synchronization respectively. (VII) is the interval of bifurcation.

The discrepancy between the large and the small $1 : 1$ Arnold tongues can be observed from Fig. 5.9, different locomotion direction are generated. In addition, the locomotion velocity is very slow in the interval (II), even though it is $1 : 1$ synchronized, and the details are discussed later. The results in interval (V) of Fig. 5.9 show that by assigning different initial conditions, the robot can slide either backward or forward with the same physical and control parameters.

The logarithmic scaled specific resistance is shown in Fig. 5.10. A promising locomotion (SR = 0.62) was observed in the bistable interval, as an extension of $1 : 2$ synchronization. Neglect the bistability, the results indicate a possibility to generate a kind of new locomotion superior to walking on the slippery surface.

Since the sliding velocity is also equivalent to the averaged rotation frequency multiplies the sliding distance in one cycle:

$$V_x = \bar{f}_r \times L_s, \tag{5.21}$$

where L_s denotes the sliding distance in one cycle. L_s is further obtained via simply divide V_x by $\bar{f}_r$ as shown in Fig. 5.11. The results indicates that the propulsive force generated at the underactuated grounding point should be further strengthened to enlarge the sliding distance in one cycle.

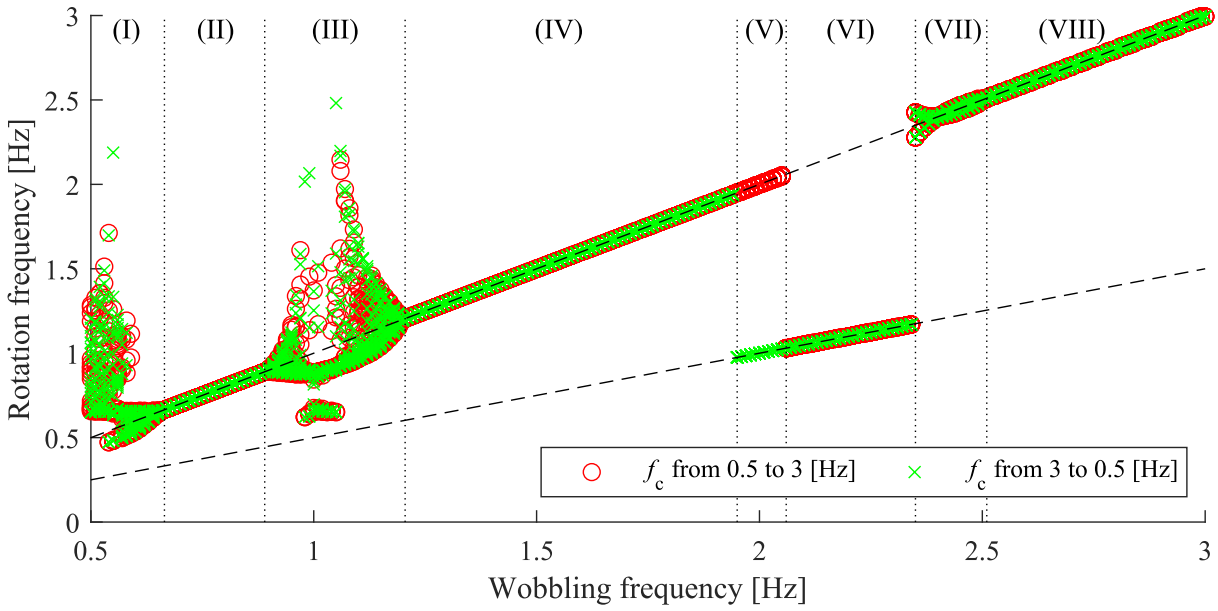

Figure 5.8: Hysteresis plot of rotation frequency with respect to wobbling frequency

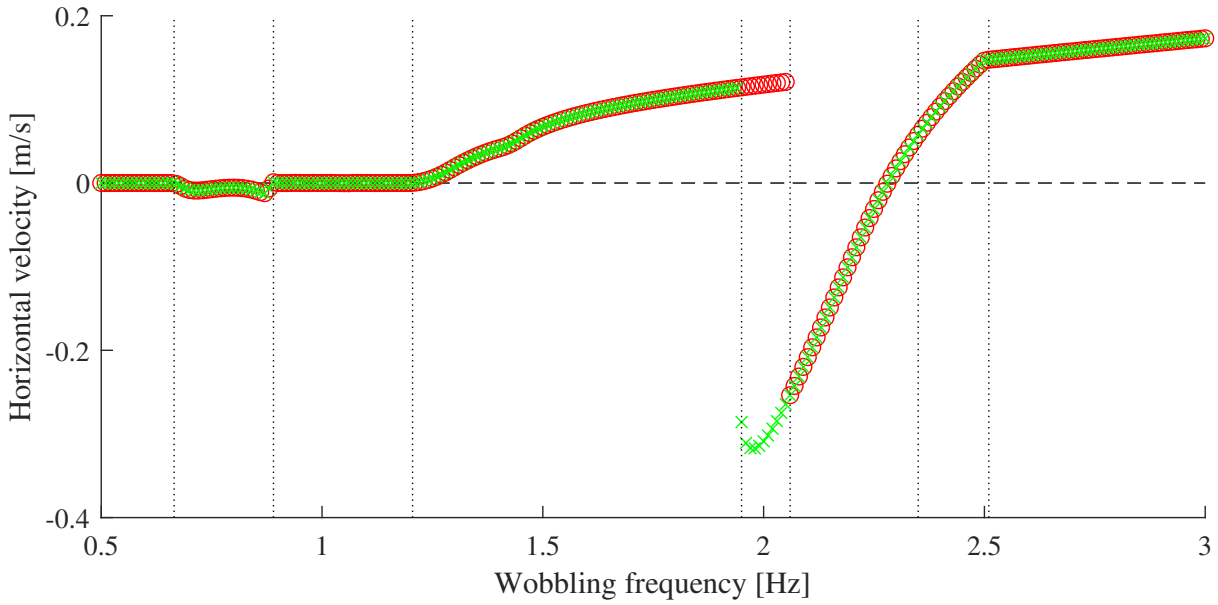

Figure 5.9: Hysteresis plot of horizontal velocity with respect to wobbling frequency

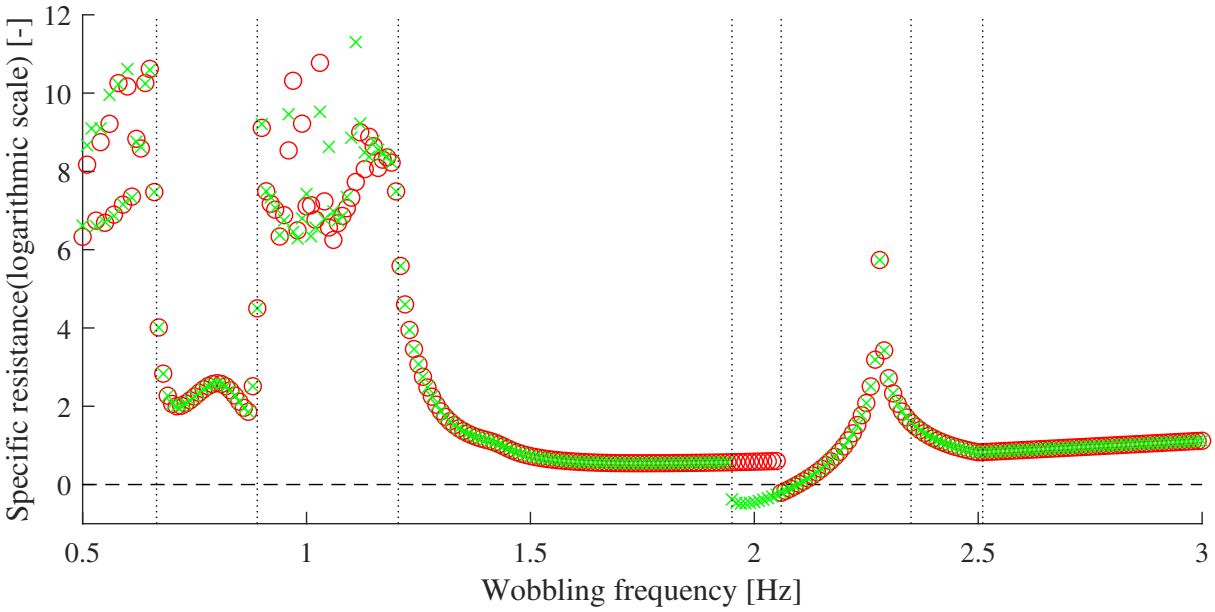

Figure 5.10: Hysteresis plot of logarithmic scaled specific resistance with respect to wobbling frequency

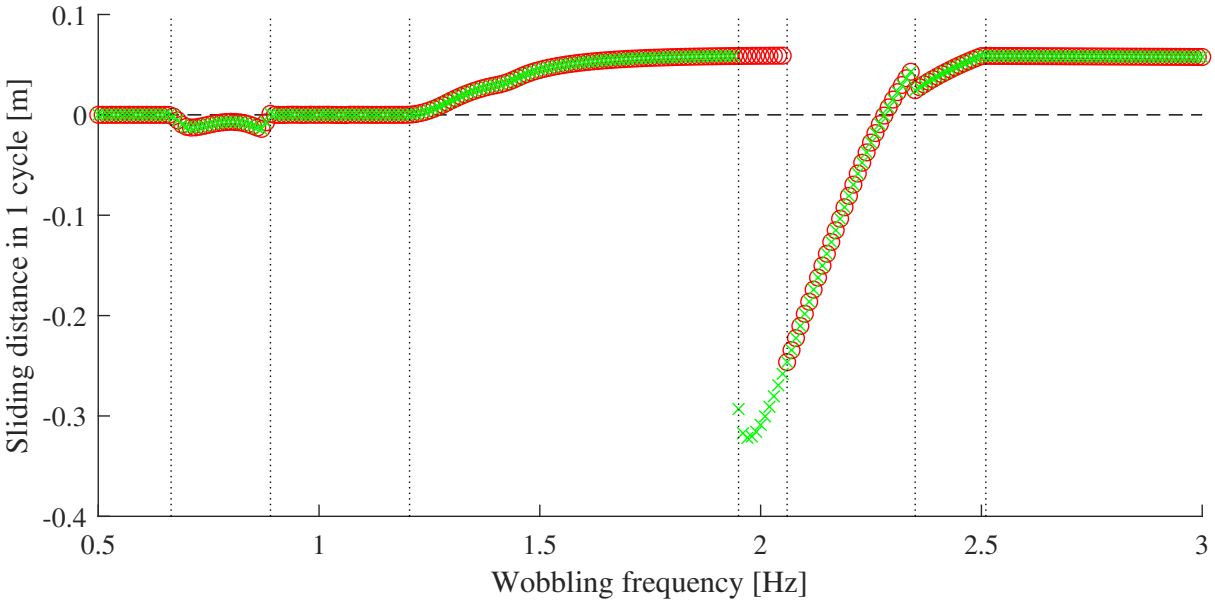

Figure 5.11: Hysteresis plot of sliding distance in one cycle with respect to wobbling frequency

5.4.3 Mechanical energy dissipation

There are two possibilities for inducing the entrained, however, inefficient locomotion:

- The locomotion is subjected to the rolling constraint, *i.e.*, sliding does not happen.
- The sliding directions are unconcentrated, therefore, the backward and forward sliding distances are canceled.

The reason is further investigated from mechanical energy dissipation point of view. The robot's total mechanical energy is given by

$$E = \frac{1}{2}\dot{\boldsymbol{q}}^{\mathrm{T}}\boldsymbol{M}(\boldsymbol{q})\dot{\boldsymbol{q}} + P(\boldsymbol{q}), \tag{5.22}$$

where $P(\boldsymbol{q})$ is the potential energy. The time-derivative of E becomes

$$\dot{E} = \dot{\boldsymbol{q}}^{\mathrm{T}}(\boldsymbol{J}^{\mathrm{T}}\lambda + \boldsymbol{J}_{\mu}^{\mathrm{T}}\lambda + \boldsymbol{S}u) = \dot{\boldsymbol{q}}^{\mathrm{T}}\boldsymbol{J}_{\mu}^{\mathrm{T}}\lambda + \dot{\boldsymbol{q}}^{\mathrm{T}}\boldsymbol{S}u = \boldsymbol{J}_{\mu}\dot{\boldsymbol{q}}\lambda + \dot{l_2}u, \tag{5.23}$$

since Eq. (5.6) holds. The first term in Eq. (5.23) is the mechanical energy consumed by friction force and the second term is the input power. In the case that Eq. (5.12) is used, the first term of Eq. (5.23) becomes:

$$\boldsymbol{J}_{\mu}\dot{\boldsymbol{q}}\lambda = -\mu_0\lambda|\dot{x} + R\dot{\theta_1}(\cos\theta_1 - 1)| \leq 0. \tag{5.24}$$

Consequently, sliding friction always dissipates mechanical energy. Then $\boldsymbol{J}_{\mu}\dot{\boldsymbol{q}}\lambda$ is integrated within one period of steady locomotion and focus on $1:1$ synchronization.

The results are shown in Fig. 5.12 and the gray boxes imply the areas out of 1:1 synchronization. By comparing Fig. 5.9 and 5.12, one can easily understand that, in most cases of the inefficient entrained locomotion, the inefficiency is due to the unconcentrated sliding direction, since considerable mechanical energy are consumed by sliding friction. For the special cases, around $f_c = 0.66,\ 0.89,\ 1.21$ [Hz], the locomotion is subjected to the rolling constraint, since mechanical energy is rarely consumed by sliding friction.

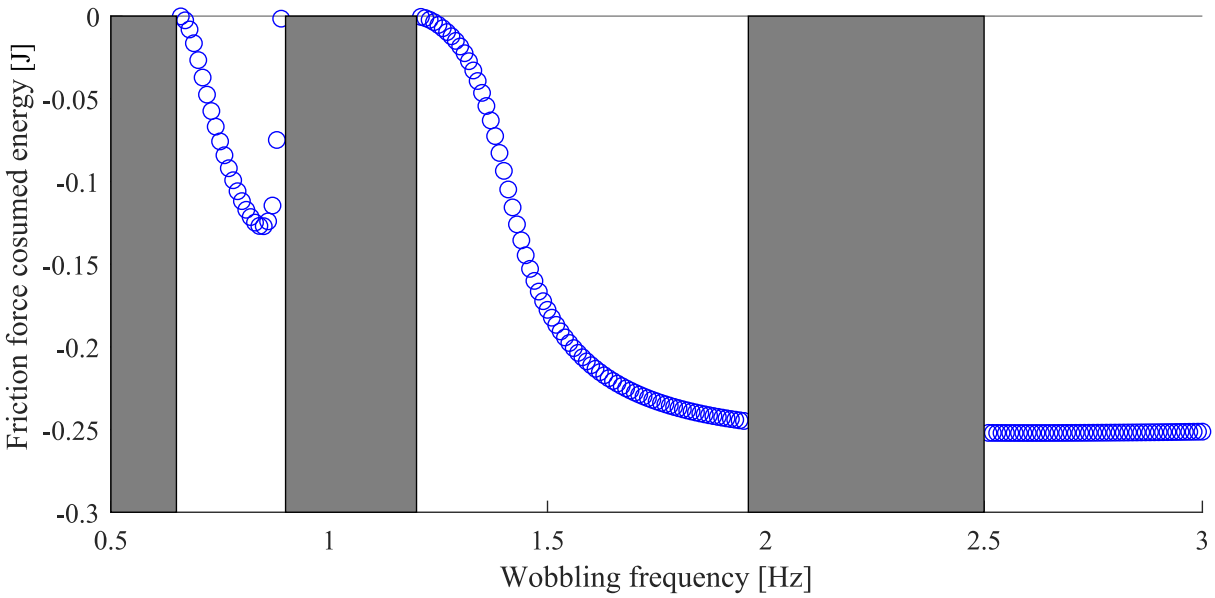

Figure 5.12: Mechanical energy consumed in one rotation period by sliding friction force

5.5 Summary and Discussions

The proposed indirectly controlled limit cycle robot generated sliding locomotion on level slippery surface successfully. The analysis above showed the high dependency of the indirectly controlled sliding locomotion on the entrainment effect. The conditions that induce the inefficient entrained locomotion have also been clarified. The performance can be improved from generally three aspects:

- Concentrate the instantaneous sliding direction instead of wandering backward and forward.
- Strengthen the propulsive force at the grounding point to increase the sliding distance in one cycle.
- Maximize the entrainment range to exclude inefficient locomotion with an optimal entrainment waveform [29] [38].

Further enhancement of this indirectly controlled limit cycle locomotion robot should be conducted based on the findings obtained from the theoretical analysis.

Chapter 6

High-speed Sliding Locomotion Generation of an Indirectly Controlled Locomotion Robot with Elastic Body

6.1 Introduction

The indirectly controlled seed-like robot proposed in the last chapter generates stable and efficient sliding locomotion on slippery level ground successfully. In contrast, the sliding velocity is not high enough. In this chapter, the original seed-like robot is modified into an arc-shaped base with an elastic body, which is modeled by spring and damper, to improve the sliding velocity from the three aspects mentioned in the last chapter. Through the theoretical analysis conducted in this paper, one can understand that not only the redundant energy is consumed by the damping force, but also the sliding stride is highly enlarged, benefit from the anti-phase oscillation between the elastic body and wobbling mass. Moreover, the entrainment effect is also strengthened, which is is one of the necessary condition for achieving stable and high performance for these indirectly controlled robots. The sliding velocity is, therefore, extremely improved by the proposed method.

This chapter is organized as follows. First, the equations of dynamics and control

is derived in Section 2. Second, typical sliding locomotion is numerically simulated in Section 3. Third, the effect of damper and spring are analyzed through mechanical energy consumption and parametric study respectively in Section 4. Fourth, nonlinear analysis is conducted in Section 5. Finally, Section 6 is devoted to summary and discussions.

6.2 Dynamics and Control

As illustrated in Fig. 6.1, The base of the indirectly controlled sliding locomotion robot is an arc-shaped frame with a length of l_0 [m], and the radius of it is R [m]. Above the base, an elastic body with a length of l_1 [m] and an actively controlled wobbling mass with a length of l_3 [m] controlled by input u [N] is connected by a rigid body with a length of l_2 [m]. Here, (x, z) is the position of the center of the bottom, θ_1 [rad] is the angular position of the base regard to vertical. θ_c [rad], which is a constant, denotes the angular position of the wobbling mass regard to vertical midline of the robot. In addition, the mass is of the base is m_0 [kg] and the inertial moment about it is I_0 [kg·m^2], the masses of the elastic body, the connection rigid body and the wobbling mass are m_1 [kg], m_2 [kg] and m_3 [kg] respectively, where the inertial moment are ignored.

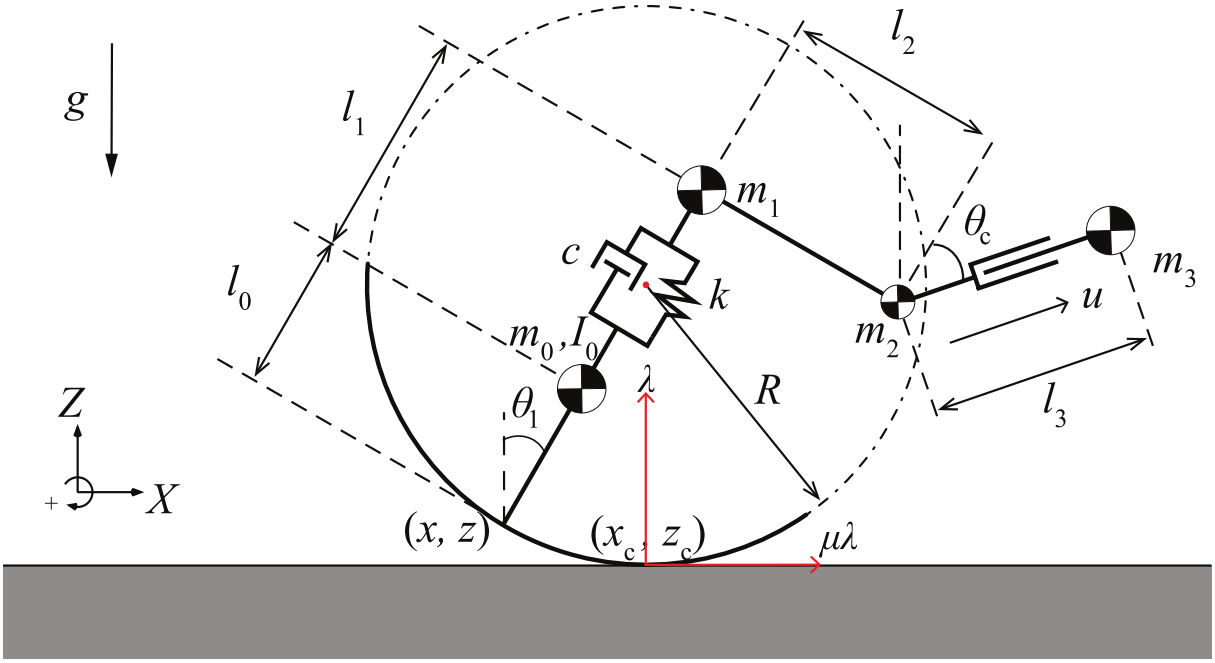

Figure 6.1: Indirectly controlled sliding locomotion robot with an elastic body

Let $\boldsymbol{q} = \begin{bmatrix} x & z & \theta_1 & l_1 & l_3 \end{bmatrix}^{\mathrm{T}}$ be the generalized coordinate vector. The robot equation of motion then becomes:

$$\boldsymbol{M}\ddot{\boldsymbol{q}} + \boldsymbol{h} = \boldsymbol{J}^{\mathrm{T}}\lambda + \boldsymbol{J}_{\mu}^{\mathrm{T}}\lambda + \tilde{\boldsymbol{S}}\tau + \boldsymbol{S}u, \tag{6.1}$$

$$[0 \quad 1 \quad -R\sin\theta_1 \quad 0 \quad 0]\dot{\boldsymbol{q}} = \boldsymbol{J}\dot{\boldsymbol{q}} = 0. \tag{6.2}$$

On the left-hand side of Eq. (6.1), $\boldsymbol{M}$ represents the inertia matrix, $\boldsymbol{h}$ represents the combination of centrifugal force, Coriolis force and gravity terms. On the right-hand side of Eq. (6.1), $\boldsymbol{J}^{\mathrm{T}}\lambda$ is the holonomic constraint, $\boldsymbol{J}_{\mu}^{\mathrm{T}}\lambda$ is the friction force term. The viscoelastic force that acts on the elastic body is modelled by the spring and damper term τ:

$$\tau = -k(l_1 - l_1^*) - c\dot{l_1}, \tag{6.3}$$

where k [N/m] is the elastic coefficient, c [N·s/m] is the viscosity coefficient, l_1^* [m] is the natural length of the elastic body, and

$$\tilde{\boldsymbol{S}} = \begin{bmatrix} 0 & 0 & 0 & 1 & 0 \end{bmatrix}^{\mathrm{T}}. \tag{6.4}$$

In addition, u is the control input which raises and drops the wobbling mass, and

$$\boldsymbol{S} = \begin{bmatrix} 0 & 0 & 0 & 0 & 1 \end{bmatrix}^{\mathrm{T}}. \tag{6.5}$$

By rearrange $\boldsymbol{h}$ and $\tilde{\boldsymbol{S}}\tau$ into:

$$\boldsymbol{H} := \boldsymbol{h} - \tilde{\boldsymbol{S}}\tau, \tag{6.6}$$

Eq. (6.1) is simplified into:

$$\boldsymbol{M}\ddot{\boldsymbol{q}} + \boldsymbol{H} = \boldsymbol{J}^{\mathrm{T}}\lambda + \boldsymbol{J}_{\mu}^{\mathrm{T}}\lambda + \boldsymbol{S}u, \tag{6.7}$$

which is similar to the equation of motion in Chap. 5. Using similar method, the second order derivative of $l_3(t)$ with respect to time becomes

$$\ddot{l_3} = \boldsymbol{S}^{\mathrm{T}}\ddot{\boldsymbol{q}} = \boldsymbol{S}^{\mathrm{T}}\boldsymbol{M}^{-1}\left(\boldsymbol{Y}(\boldsymbol{S}u - \boldsymbol{H}) - \hat{\boldsymbol{J}}^{\mathrm{T}}X^{-1}\dot{\boldsymbol{J}}\dot{\boldsymbol{q}}\right) = Au - B, \tag{6.8}$$

where

$$
\begin{aligned}
\lambda &= -X^{-1}\left(\boldsymbol{J}\boldsymbol{M}^{-1}(\boldsymbol{S}u-\boldsymbol{H})+\dot{\boldsymbol{J}}\dot{\boldsymbol{q}}\right),\\
X &:= \boldsymbol{J}\boldsymbol{M}^{-1}\hat{\boldsymbol{J}}^{\mathrm{T}},\\
\hat{\boldsymbol{J}} &:= \boldsymbol{J}+\boldsymbol{J}_{\mu},\\
\boldsymbol{Y} &:= \boldsymbol{I}_5-\hat{\boldsymbol{J}}^{\mathrm{T}}X^{-1}\boldsymbol{J}\boldsymbol{M}^{-1},\\
A &:= \boldsymbol{S}^{\mathrm{T}}\boldsymbol{M}^{-1}\boldsymbol{Y}\boldsymbol{S},\\
B &:= \boldsymbol{S}^{\mathrm{T}}\boldsymbol{M}^{-1}\left(\boldsymbol{Y}\boldsymbol{H}+\hat{\boldsymbol{J}}^{\mathrm{T}}X^{-1}\dot{\boldsymbol{J}}\dot{\boldsymbol{q}}\right).
\end{aligned}
$$

Consequently, the control input for enabling $l_3(t)$ to track $l_{3\mathrm{d}}(t)$ is defined as

$$u = A^{-1}(v+B), \tag{6.9}$$

$$v = \ddot{l}_{3\mathrm{d}}(t)+K_{\mathrm{D}}(\dot{l}_{3\mathrm{d}}(t)-\dot{l}_3)+K_{\mathrm{P}}(l_{3\mathrm{d}}(t)-l_3), \tag{6.10}$$

Since the time trajectory of a linear spring is harmonic, the desired trajectory of the wobbling mass is set to

$$l_{3\mathrm{d}}(t) = A_m\sin(2\pi f_c t), \tag{6.11}$$

for easily inducing entrainment phenomenon.

6.3 High-speed Locomotion Generation

Numerical simulation of the sliding locomotion is conducted using the parameters listed in Table 6.1, and the initial conditions are set to:

$$\boldsymbol{q}(0) = \begin{bmatrix} 0 & 0 & 0 & 0 & 0 \end{bmatrix}^{\mathrm{T}}, \dot{\boldsymbol{q}}(0) = \begin{bmatrix} 0 & 0 & 0 & 0 & 0 \end{bmatrix}^{\mathrm{T}}. \tag{6.12}$$

Fig. 6.2 shows the simulation results of sliding locomotion on slippery road surface. From Fig. 6.2(a), one can see that the underactuated robot moves forward successfully. The sliding direction is highly concentrated after a quick initialization as shown in Fig. 6.2(b). The rotation angle of the robot in Fig. 6.2(c) keeps positive, indicates that the grounding point is always on the right bottom of the arc-shaped base. Fig. 6.2(d) shows that the length of elastic body varies harmonically due to the oscillation of the spring. The oscillation amplitude of the spring is not decayed by the damper, resultant from the

Table 6.1: Physical and control parameters for sliding locomotion robot with elastic body

m_0	0.5	kg
m_1	0.5	kg
m_2	0.1	kg
m_3	0.4	kg
I_0	0.1	kg·m^2
l_0	0.3	m
R	0.8	m
l_2	0.4	m
θ_c	$\pi/6$	rad
l_1^*	0.2	m

g	9.81	m/s^2
K_D	40	s^{-2}
K_P	400	s^{-1}
k	100	N/m
c	20	N · s/m
μ_0	0.1	
s	20000	
A_m	0.2	m
f_c	2.5	Hz

sinusoidal wobbling motion as shown in Fig. 6.2(e). Moreover, positive ground reaction force is guaranteed during the sliding locomotion as shown in Fig. 6.2(f).

Fig. 6.3 shows the stick diagram of the locomotion, one can observe that the robot achieves high speed sliding locomotion without inducing violently rotation motion, benefited from the fact that the robot is promoted by oscillating the elastic body.

Fig. 6.4 shows the phase-plane plot of steady locomotion. Limit cycle sliding locomotion is generated, and it can be easily observed that the instantaneous sliding velocity in one cycle has a negative correlation with the angular velocity. During the anti-clockwise rotation ($\dot{\theta_1} < 0$) of the arc-shaped base, the robot maintains sliding forward. Although both forward and backward sliding take place during the clockwise rotation ($\dot{\theta_1} > 0$), the asymmetric instantaneous sliding velocity results in a high speed forward sliding in a whole cycle.

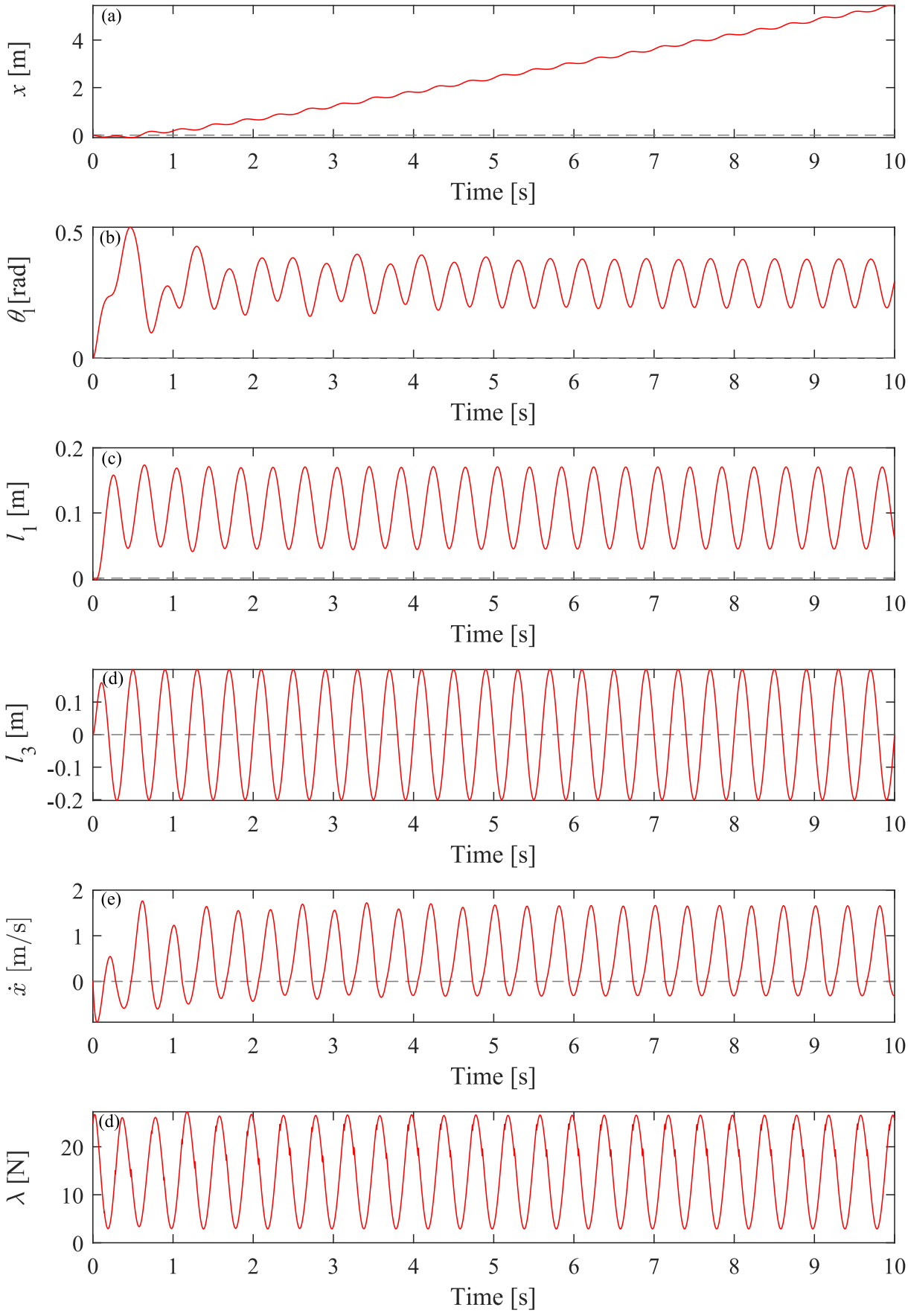

Figure 6.2: Motion generation of a sliding robot on slippery surface

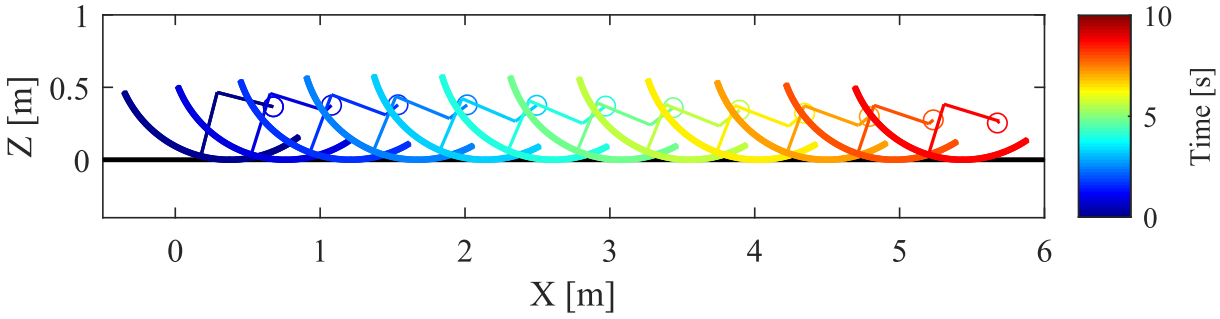

Figure 6.3: Stick diagram of a sliding robot on slippery surface

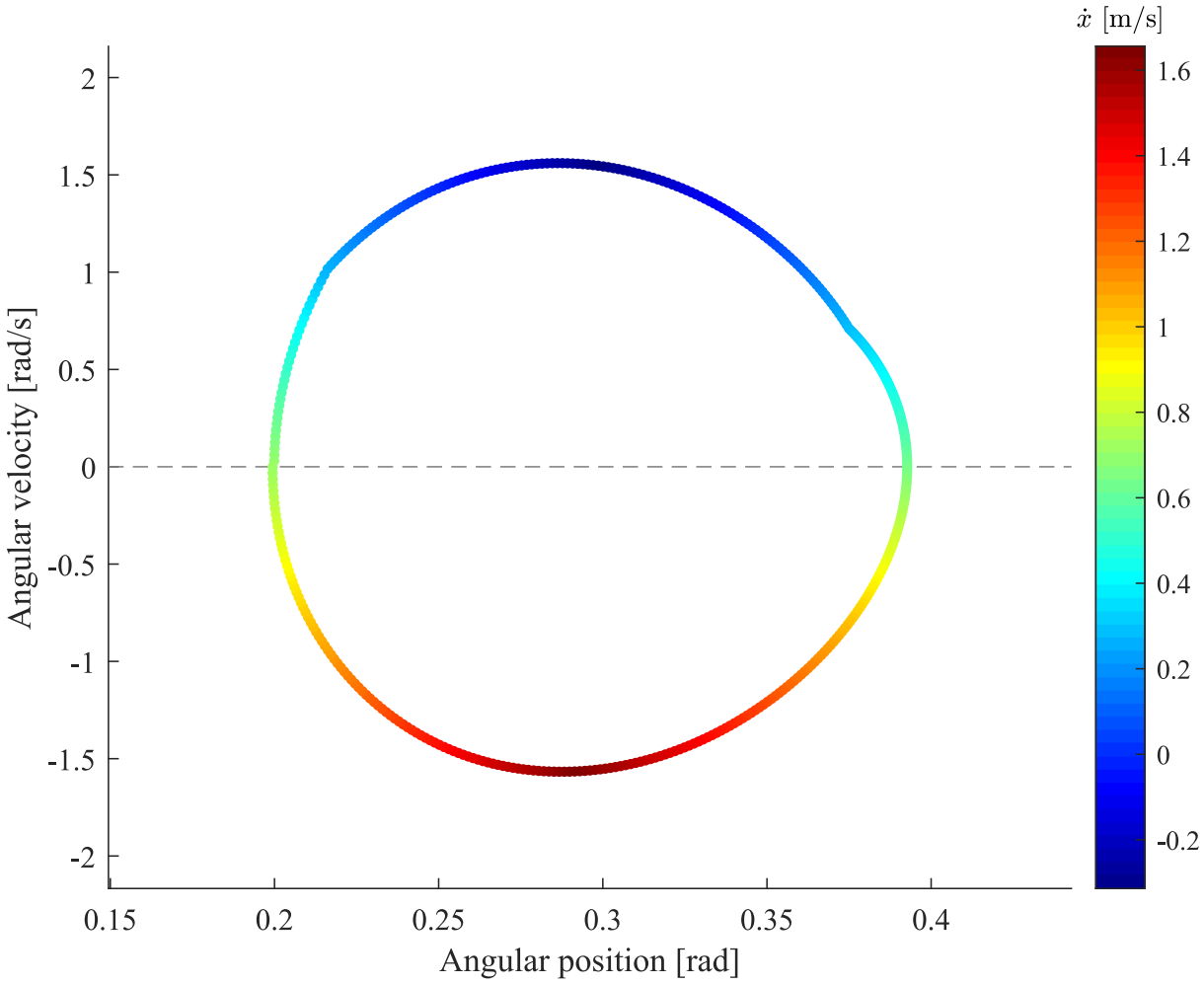

Figure 6.4: Phase-plane plot of steady sliding locomotion

6.4 Locomotion Analysis

6.4.1 Effect of damper

The simulation of typical locomotion shows that the asymmetricity of sliding is strongly increased, and the results are first analyzed from the energy consumption point of view. The robot's total mechanical energy is given by

$$E(\boldsymbol{q}, \dot{\boldsymbol{q}}) = \frac{1}{2}\dot{\boldsymbol{q}}^{\mathrm{T}}\boldsymbol{M}(\boldsymbol{q})\dot{\boldsymbol{q}} + P(\boldsymbol{q}), \tag{6.13}$$

$P(\boldsymbol{q})$ is the summation of position and elasticity energy:

$$P(\boldsymbol{q}) = \sum_{n=0}^{3} m_i g z_i + \frac{1}{2}k(l_1 - l_1^*)^2, \tag{6.14}$$

where z_i is the height of each mass and the second term is the elastic energy. The viscous dissipation function $R(\dot{\boldsymbol{q}})$ is given by

$$R(\dot{\boldsymbol{q}}) = \frac{1}{2}c\dot{l_1}^2. \tag{6.15}$$

The time-derivative of E becomes

$$\dot{E} = \dot{\boldsymbol{q}}^{\mathrm{T}}\left(\boldsymbol{S}u + \boldsymbol{J}^{\mathrm{T}}\lambda + \boldsymbol{J}_\mu^{\mathrm{T}}\lambda - \frac{\partial R(\dot{\boldsymbol{q}})}{\partial \dot{\boldsymbol{q}}^{\mathrm{T}}}\right) = \dot{\boldsymbol{q}}^{\mathrm{T}}\boldsymbol{S}u + \dot{\boldsymbol{q}}^{\mathrm{T}}\boldsymbol{J}_\mu^{\mathrm{T}}\lambda - \dot{\boldsymbol{q}}^{\mathrm{T}}\frac{\partial R(\dot{\boldsymbol{q}})}{\partial \dot{\boldsymbol{q}}^{\mathrm{T}}} = \dot{d}u + \boldsymbol{J}_\mu\dot{\boldsymbol{q}}\lambda - c\dot{l_1}^2. \tag{6.16}$$

The first term in Eq. (6.16) is input power, the second term is the mechanical energy consumed by friction force and the third term is the mechanical energy consumed by damping force. The robot slides backward/forward by friction force which dissipates the mechanical energy. The damping force, therefore, is expected to consume part of redundant mechanical energy that leads to backward sliding, results in a concentrated forward sliding.

To verify the analysis above, the viscosity coefficient is varied, and the performance is evaluated by sliding velocity of the locomotion and energy efficiency though V_x and SR defined as same as Chap. 5.

Follow process is conducted to obtain the data:

(A1) Set $c = 0$ [N·s/m] and run the simulation with the initial conditions as Eq. (6.12).

(A2) After 100 [s] of locomotion, save the averaged V_x, $\log_{10}\mathrm{SR}$.

(A3) Increase c by 0.1 [N·s/m] and run the next simulation with the same initial conditions.

(A4) Repeat from (A2) to (A3) until $c = 20$ [N·s/m].

Despite the signum, Fig. 6.5 shows that the sliding velocity is slow when $c < 4$ [N·s/m], and increase monotonically until $c = 14.5$ [N·s/m]. The result implies that part of the redundant energy can be consumed by damping effect via increasing the viscosity coefficient in a certain range, induces an increase of the averaged sliding velocity.

Fig. 6.6 shows that the specific resistance is high, when the sliding velocity is slow. Moreover, the overall efficiency is not improved compared with the original seed-like robot, due to the additional energy consumption term.

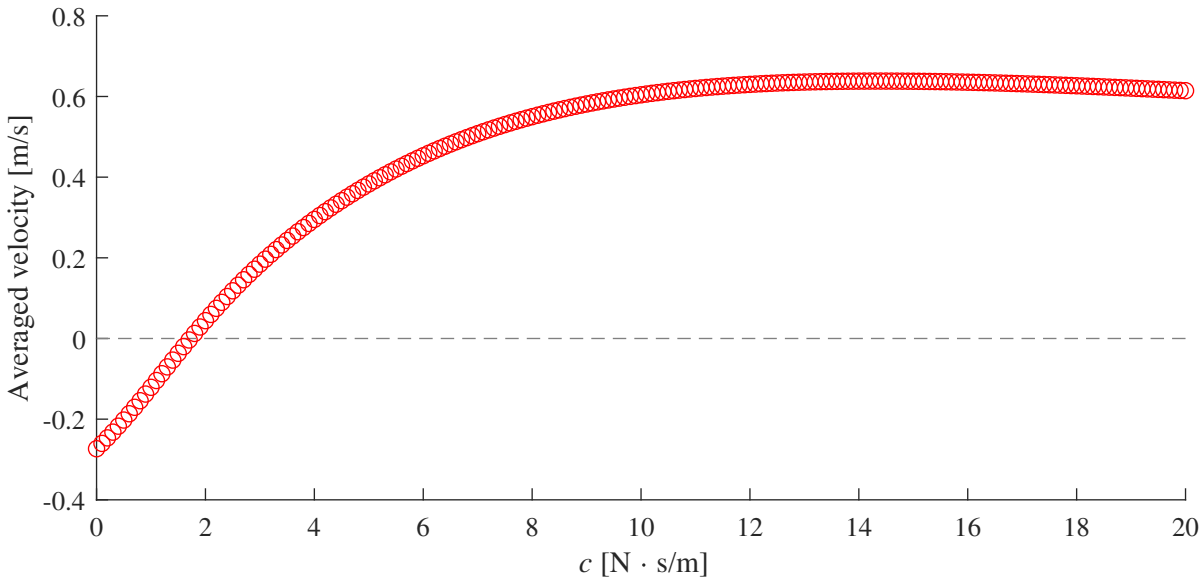

Figure 6.5: Sliding velocity with respect to viscosity coefficient

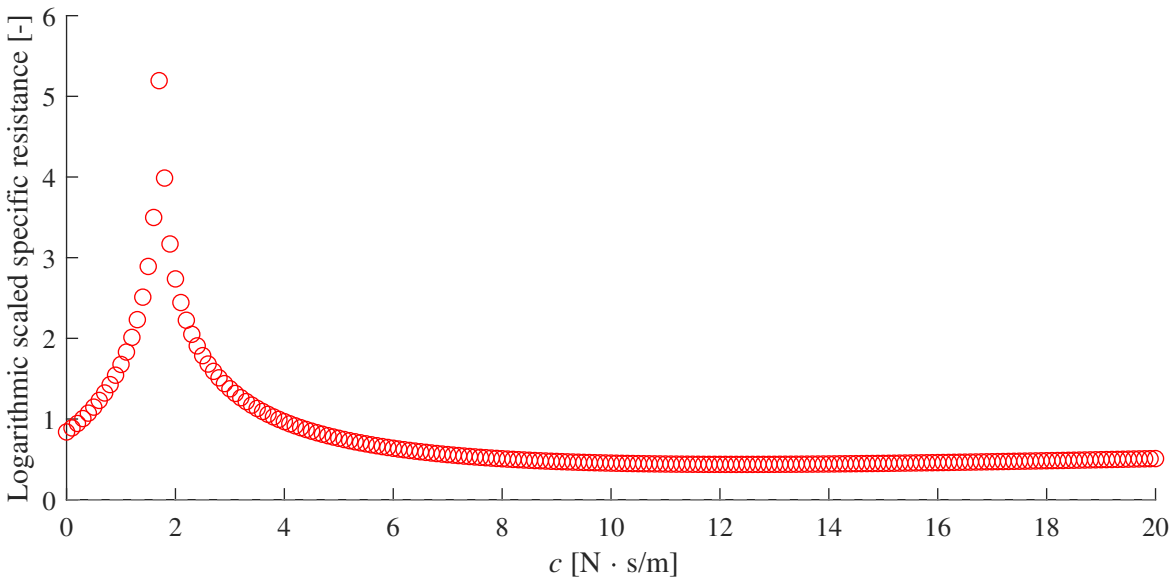

Figure 6.6: Specific resistance with respect to viscosity coefficient

6.4.2 Effect of spring

The oscillation of spring, which is indirectly powered by the wobbling mass, enhances shifting the CoM of the robot. It is therefore necessary to analyze the effect of spring by varying the wobbling frequency and the spring's natural frequency simultaneously, where the spring's natural frequency is calculated as:

$$f_{ns} = \frac{1}{2\pi}\sqrt{\frac{k}{m_1 + m_2}}. \tag{6.17}$$

Follow process is conducted to obtain the averaged sliding velocity and specific resistance:

(B1) Set the spring's natural frequency $f_{ns} = 1$[Hz].

(B2) Set the wobbling frequency $f_c = 1$ [Hz].

(B3) Run the simulation with the initial conditions as Eq. (6.12).

(B4) After 100 [s] of locomotion, average the V_x and $\log_{10}$SR in 20 periods.

(B5) Increase f_c by 0.1 [Hz]and run the next simulation.

(B6) Repeat from (B3) to (B5) until $f_c = 3$ [Hz].

(B7) Increase f_{ns} by 0.1 [Hz] and return to (B3).

(B8) Repeat from (B3) to (B7) until $f_{ns} = 3$ [Hz].

Fig. 6.7 shows the averaged sliding velocity. The white range indicates the ground reaction force are negative, where the edge constraint is satisfied in the whole range. The failed locomotion are, therefore, reduced by the harmonically oscillation of the spring. The velocity shows a positive correlation with the wobbling frequency, however, there is a boundary along the gray arrow, implies different locomotion mode on each side. The velocity inside the dashed square is affected by both wobbling frequency and the spring's natural frequency, the tendency is represented by the black arrow. In contrast, the velocity is affected mainly by the wobbling frequency outside the square.

The specific resistance is plotted in logarithm scale as shown in Fig. 6.8 in order to decrease the significance of high values. Results with high values, which indicate inefficient sliding locomotion, are represented in red and the contours in the figure are similar with

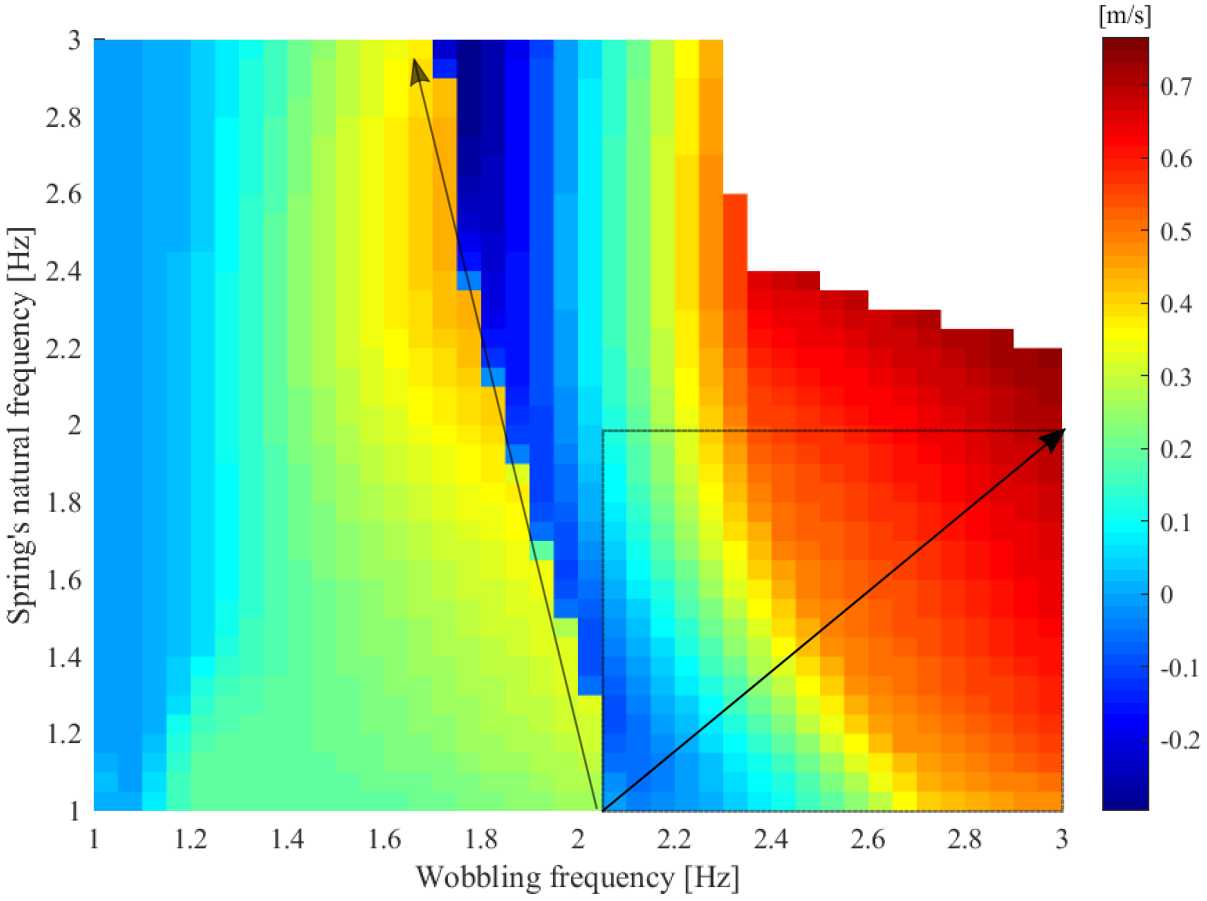

Figure 6.7: Sliding velocity with respect to wobbling frequency and spring's natural frequency

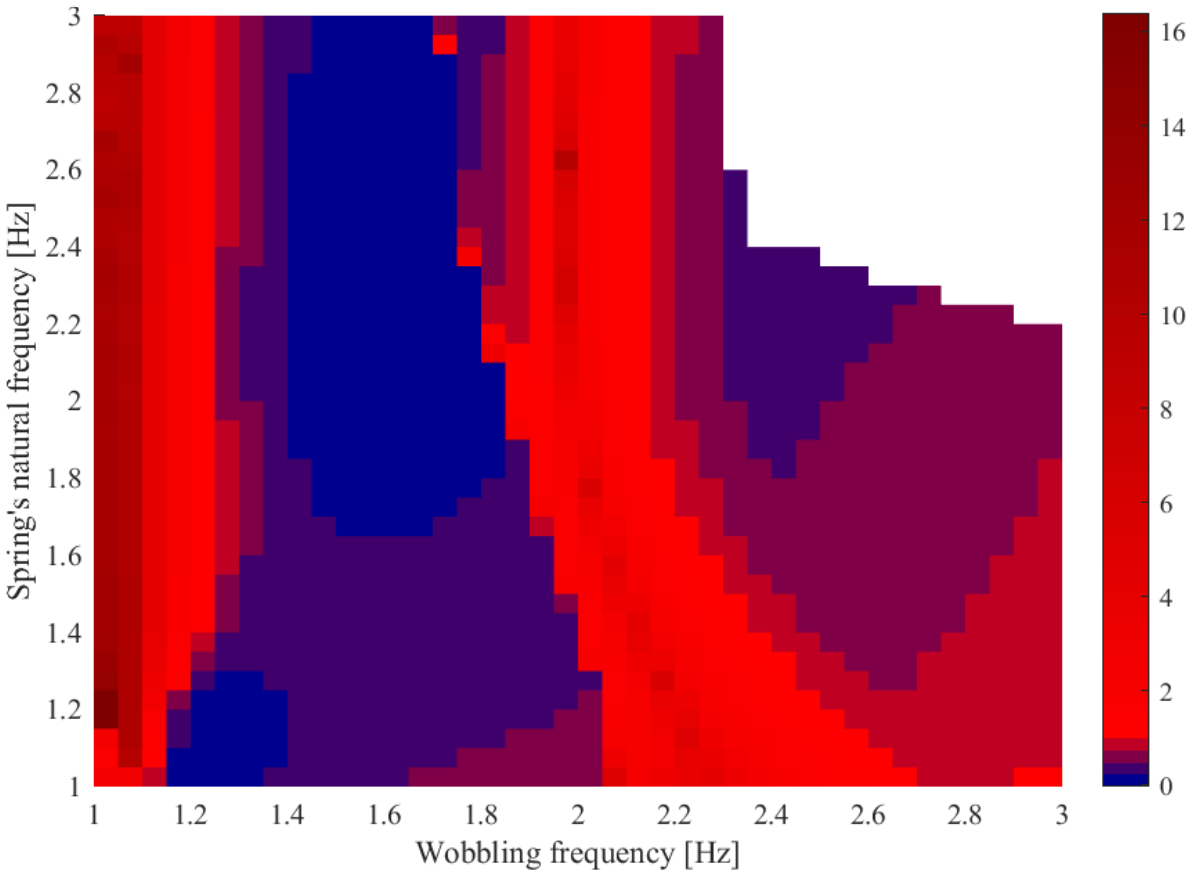

Figure 6.8: Logarithmic scaled specific resistance with respect to wobbling frequency and spring's natural frequency

Fig. 6.7. However, the effect of spring's natural frequency on specific resistance does not demonstrate a clear-cut tendency. Moreover, sliding velocity and energy efficiency are difficult to be guaranteed simultaneously since the increase in velocity is induced by consuming the energy by damping effect.

6.5 Nonlinear Analysis

Previous section shows complex structures of the locomotion, it is therefore necessary to conduct nonlinear analysis to observe the details.

Besides sliding velocity and specific resistance, three additional gait descriptors is used, *i.e.*, rotation frequency f_r, spring oscillation frequency f_s and phase difference ψ between

the elastic body and the wobbling mass, defined as follows:

$$f_r := \frac{1}{T_r}, \quad f_s := \frac{1}{T_s}, \quad \psi := \frac{2\pi(t_s - t_c)}{T_r}, \tag{6.18}$$

where T_r and T_s represent the periods of arc-shaped base rotation and spring's oscillation in steady locomotion respectively. As shown in Fig. 6.9, the period is defined as the duration between two local minimum. In addition, t_s denotes the timing, when the oscillation of the spring reaches local maximum. Similarly, t_c denotes the timing, when the length of the wobbling mass reaches local maximum in the rotation period.

Following process is conducted to obtain the gait descriptors with parameters in Tab. 6.1:

(C1) Set $f_c = 1$ [Hz] and run the simulation with the initial conditions to Eq. (6.12).

(C2) After 100 [s] of locomotion, save f_r, ψ for 20 period of rotation and the averaged V_x, $\log_{10}$ SR.

(C3) Increase f_c by 0.01 [Hz] and run the next simulation with the same initial conditions.

(C4) Repeat from (C2) to (C3) until $f_c = 3$ [Hz].

The rotation frequency and the spring's oscillation frequency are shown together in Fig. 6.10. Period 1 locomotion is generated at low frequency wobbling, since both the frequencies of the rotation and the oscillation overlap on the 1 : 1 synchronization dashed

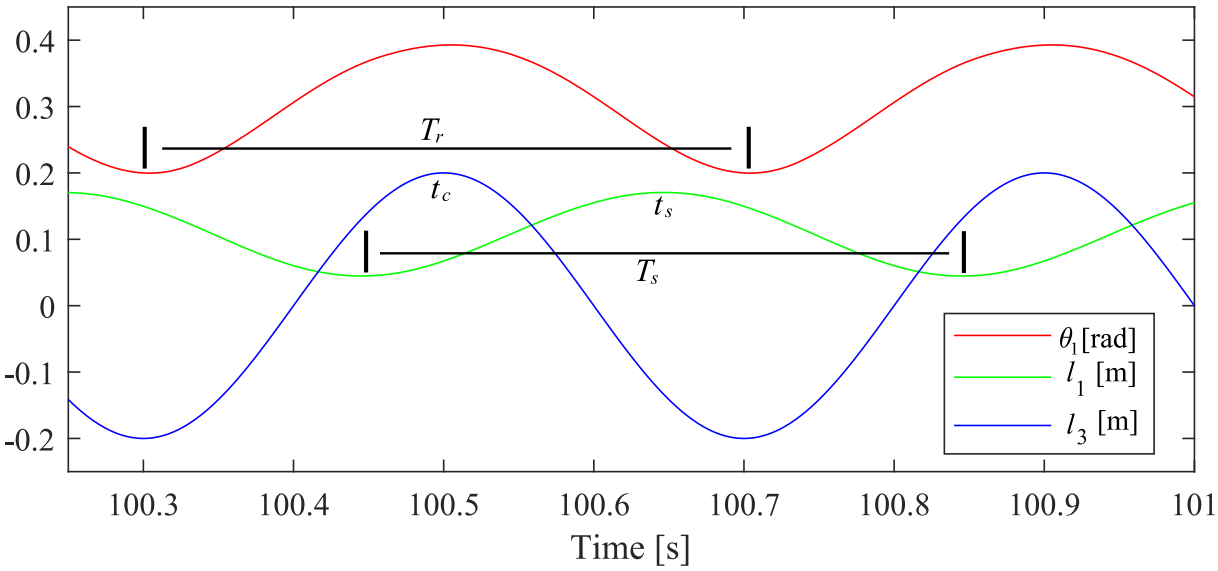

Figure 6.9: Phase difference between spring and wobbling mass

line ($f_r = f_s = f_c$). The Oscillation frequency bifurcates when the rotation frequency drop to 1 : 2 synchronization dashed line ($f_r = \frac{f_c}{2}$), due to wobbling around twice of the natural frequency of the rotation, which is estimated via fixing the wobbling mass at the attaching point by revising $\boldsymbol{J}$ and $\boldsymbol{J}_\mu$ to

$$\bar{\boldsymbol{J}} = \begin{bmatrix} \boldsymbol{J} & \\ \mathbf{0}_{1\times 4} & 1 \end{bmatrix}, \bar{\boldsymbol{J}}_\mu = \begin{bmatrix} \boldsymbol{J}_\mu \\ \mathbf{0}_{1\times 5} \end{bmatrix}. \tag{6.19}$$

With the increasing of the wobbling frequency, both the frequencies of the rotation and the oscillation reconverge to 1 : 1 synchronization, with bifurcation as a transition. The entrainment effect is strengthened compared with previous section, since only period 1 and period 2 locomotion are generated, where being entrained is one of the necessary condition for these robots to generate high performance locomotion.

Fig. 6.11 shows that the phase difference between the elastic body and the wobbling mass has a positive relationship with the wobbling frequency in period 1 locomotion, especially when wobbling with high frequency, the elastic body and the wobbling mass become almost anti-phase oscillation, *i.e.*, the phase difference tends to π. Since the masses move along almost opposite directions, this phenomenon leads to an effect which is similar with magnifying the amplitude of the rotation.

Fig. 6.12 shows that the sliding velocity of the locomotion with 1 : 2 synchronization is general slower than 1 : 1 synchronization, since the sliding locomotion occurs with the rotation of the arc-shaped base together, where the 1 : 2 synchronization indicates that during 2 cycles of wobbling, the rotation take place only 1 cycle. Similarly, result in high values in Fig. 6.13.

Moreover, L_s is obtained via dividing V_x by $\bar{f}_r$ as shown in Fig. 6.14. Despite the inefficient 1 : 2 synchronization locomotion, the result indicates that the sliding distance in one cycle is enlarged by increasing the wobbling amplitude and finally converges. Consistent with the results in Fig. 6.11, the sliding distance in one cycle is larger when the elastic body and the wobbling mass are anti-phase. The elasticity of the body, therefore, has a tendency to enhance the propulsive force at the underactuated grounding point.

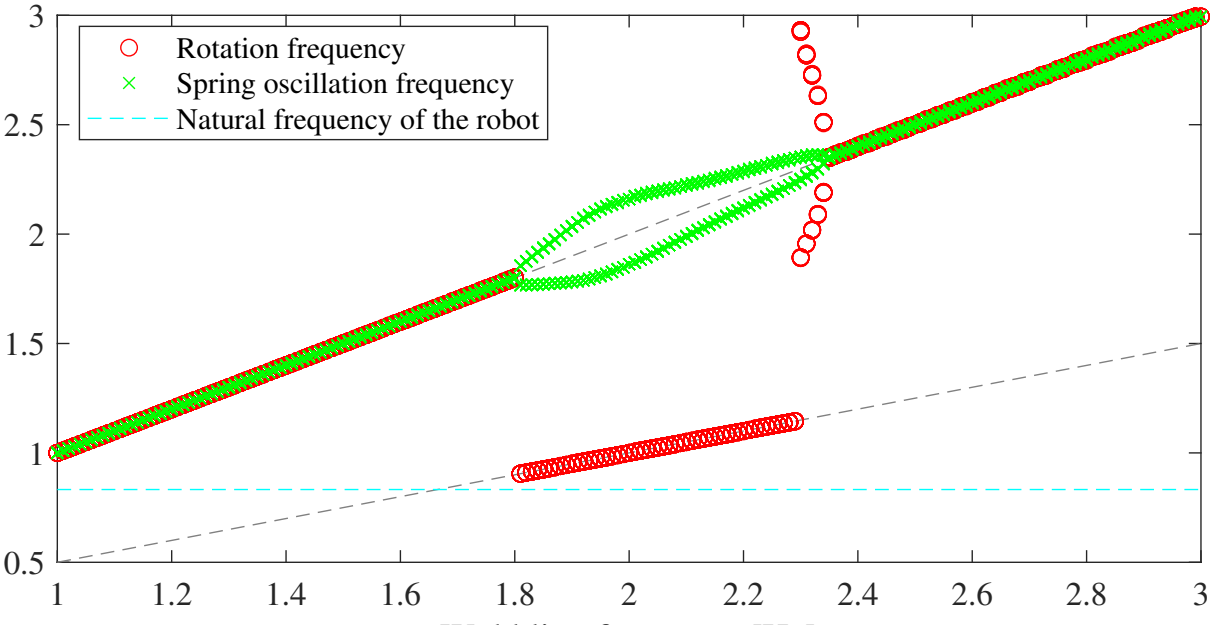

Figure 6.10: Rotation frequency and spring's oscillation frequency with respect to wobbling frequency

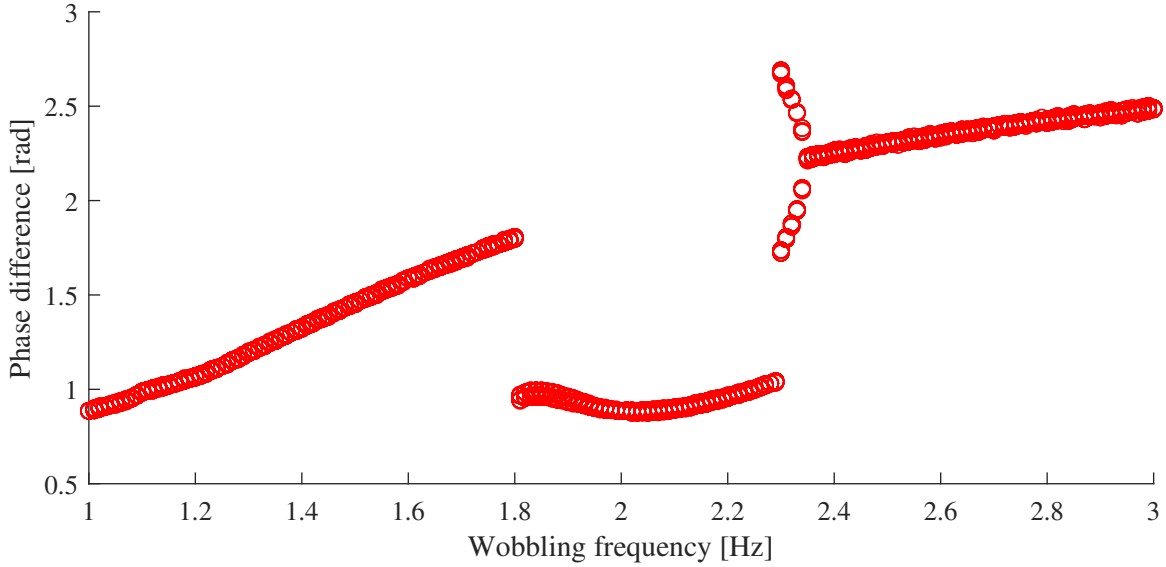

Figure 6.11: Phase difference with respect to wobbling frequency

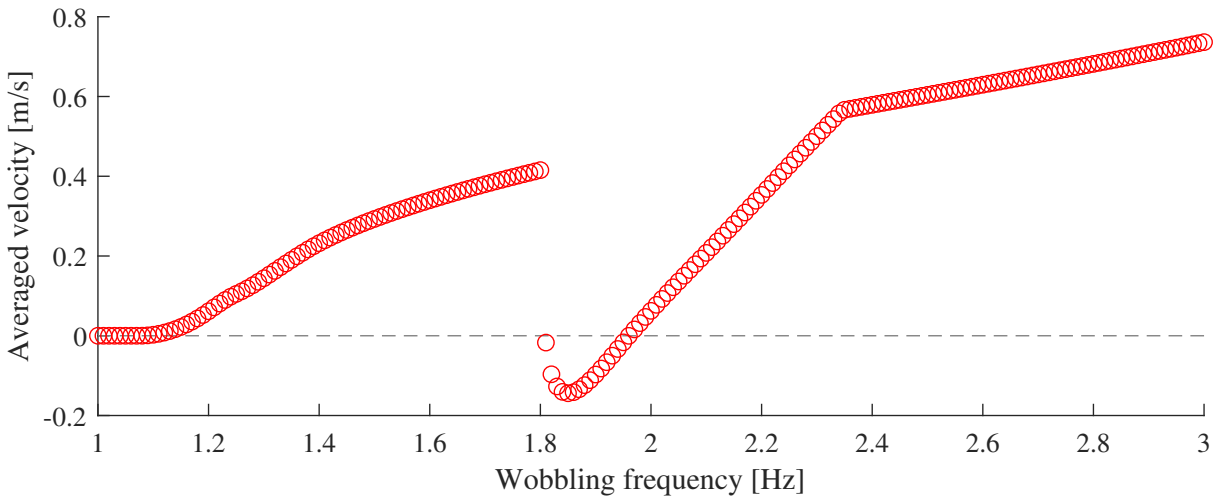

Figure 6.12: Sliding velocity with respect to wobbling frequency

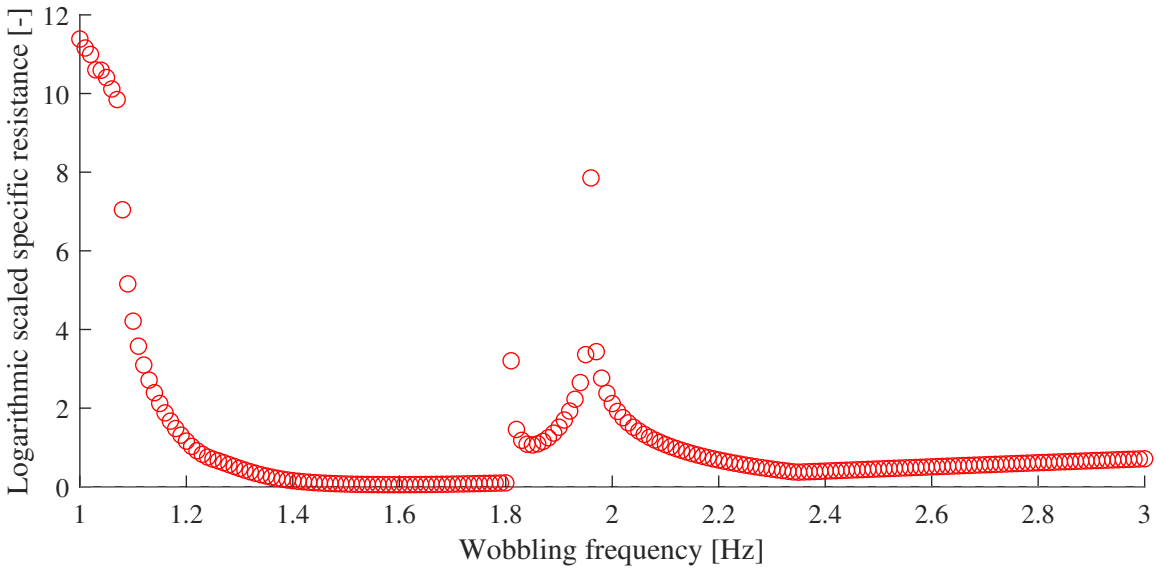

Figure 6.13: Logarithmic scaled specific resistance with respect to wobbling frequency

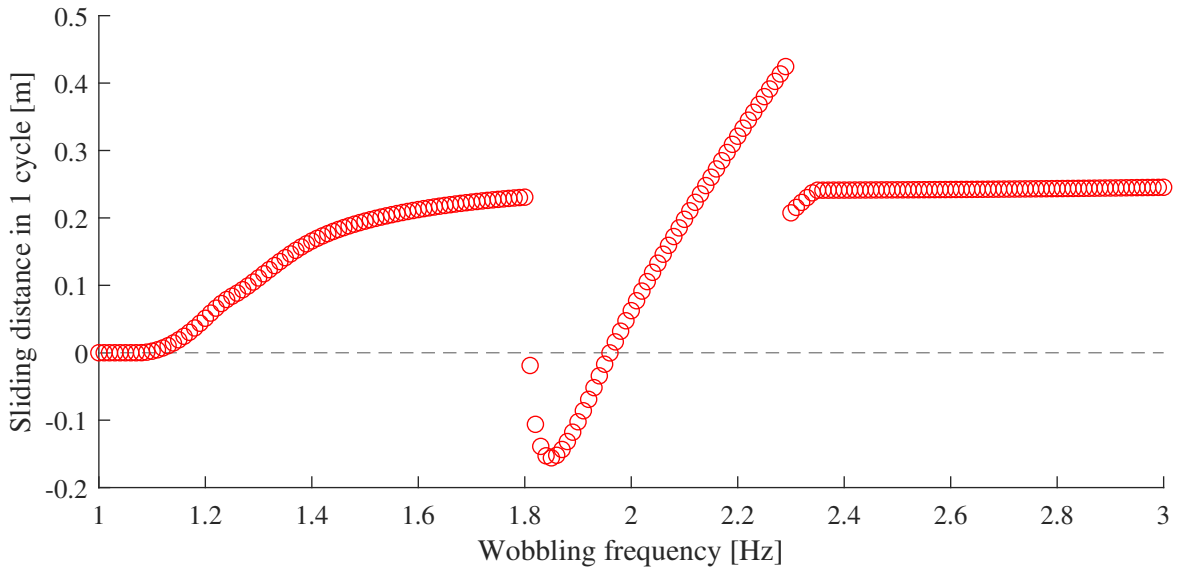

Figure 6.14: Sliding distance in 1 period with respect to wobbling frequency

6.6 Summary and Discussions

With the purpose of enhancing the performance of indirectly controlled sliding locomotion on slippery ground, the original seed-like robot is modified into an arc-shaped base with an elastic body introduced in this chapter. The velocity of the modified robot is highly increased from the three aspects discussed in last chapter:

- The instantaneous sliding direction is concentrated by the damping force.
- The propulsive force around the grounding point is increased by the anti-phase oscillation between the wobbling mass and the spring.
- The entrainment range is enlarged, benefited from the elasticity of the body. In this case, sine wave is the optimal entrainment waveform since the spring's oscillation is sinusoidal.

Chapter 7

Conclusion and Future Works

7.1 Summary

Towards achieving stable and efficient locomotion of underactuated robots on the slippery ground using the indirectly controlled mechanism, following works have been done in this dissertation:

- Analysis on nonlinear properties, *s.t.*, entrainment, bistability, synchronization and chaos, of indirectly controlled limit cycle locomotion robots is performed using CRW as an example.

- The overall entrainment effect is experimentally verified by means of Arnold tongue. The walking frequency is measured via accelerometer inspired by the collision equation.

- An optimal entrainment waveform for indirectly controlled limit cycle locomotion robots is analytically derived using CRW as a simple example based on the phase reduction theory. The phase response curve of it is numerically acquired by applying slight perturbations on different phases of a whole limit cycle.

- Based on the conclusions and findings of indirectly controlling mechanism obtained above, an active wobbling mass with up-and-down oscillation is attached to a seed-like underactuated robot which generates stable and efficient locomotion on slippery level ground. Theoretical analysis on velocity, efficiency, entrainment effect and mechanical energy consumption are performed for enhancement.

- The performance of indirectly controlled sliding locomotion robot is enhanced by modifying the original model into an arc-shaped base with an elastic body based on the theoretical analysis.

7.2 Conclusion

Locomotion robots can be forced into indirectly controlled limit cycle oscillation systems by attaching an active wobbling mass to it via entrainment effect. The dynamics of these indirectly controlled limit cycle locomotion robots are highly nonlinear. The optimization of the desired trajectory for the wobbling mass can be analytically derived by using phase reduction theory. The indirectly controlling mechanism can be applied for achieving stable and efficient locomotion of underactuated robots on complex terrains with appropriate design. In these cases, not only the optimization of entrainment effect, but also the strategies for overcoming the underactuation of the system should be carefully considered by positively utilizing the oscillation of it.

7.3 Contribution

This dissertation not only theoretically analyzed the indirectly controlling mechanism from nonlinear dynamics and mechanical engineering points of view, but also experimentally verified its practicability. Most importantly, enhancement and optimization for indirectly controlled locomotion robots are performed based on the theoretical analysis. Therefore, this indirectly controlling mechanism owns a potentiality to be applied into more complicated locomotion robots on rough terrains as well as manipulation systems based on the methods and findings of this dissertation. Moreover, the entrainment effect based gait frequency control can be applied to rehabilitation of Parkinson's disease and the device of walking support machine.

7.4 Future Works

Currently, locomotion robots proposed and investigated in the dissertation as individuals. Combination and cooperation [39] [40] [41] [42] among multiple robots with different

natural dynamics will be more interesting since they can be considered as multiple oscillators. On one hand, multiple robots could be affected by single wobbling mass, dominance relationship among them will be further investigated and discussed. On the other hand, multiple wobbling masses can be attached to locomotion systems. Kuramoto model [43], which represents the behavior of several coupled oscillators, will be further applied for analysis and control.

Bibliography

[1] M. W. Spong, "Energy based control of a class of underactuated mechanical systems," *Proceedings of the 1996 IFAC World Congress*, pp. 431–435, 1996.

[2] K. Kaneko, F. Kanehiro, S. Kajita, M. Morisawa, K. Fujiwara, K. Harada, and H. Hirukawa, "Slip observer for walking on a low friction floor," *Proceedings of the IEEE/RSJ International Conference on Intelligent Robots and Systems*, pp. 634–640, 2005.

[3] K. Kaneko, K. Harada, F. Kanehiro, G. Miyamori, and K. Akachi, "Humanoid robot hrp-3," *Proceedings of the IEEE/RSJ International Conference on Intelligent Robots and Systems*, pp. 2471–2478, 2008.

[4] M. Bloesch, C. Gehring, P. Fankhauser, M. Hutter, M. A. Hoepflinger, and R. Siegwart, "State estimation for legged robots on unstable and slippery terrain," *Proceedings of the IEEE/RSJ International Conference on Intelligent Robots and Systems*, pp. 6058–6064, 2013.

[5] N. J. Kohut, A. O. Pullin, D. W. Haldane, D. Zarrouk, and R. S. Fearing, "Precise dynamic turning of a 10 cm legged robot on a low friction surface using a tail," *Proceedings of the IEEE International Conference on Robotics and Automation*, pp. 3299–3306, 2013.

[6] M. Brandao, K. Hashimoto, J. Santos-Victor, and A. Takanishi, "Footstep planning for slippery and slanted terrain using human-inspired models.," *IEEE Transactions on Robotics*, vol. 32, no. 4, pp. 868–879, 2016.

[7] H. Poincaré, "Mémoire sur les courbes définies par une équation différentielle (i)," *Journal de mathématiques pures et appliquées*, vol. 7, pp. 375–422, 1881.

[8] T. McGeer *et al.*, "Passive dynamic walking," *The International Journal of Robotics Research*, vol. 9, no. 2, pp. 62–82, 1990.

[9] A. Goswami, B. Espiau, and A. Keramane, "Limit cycles and their stability in a passive bipedal gait," *Proceedings of the IEEE International Conference on Robotics and Automation*, vol. 1, pp. 246–251, 1996.

[10] F. Asano, M. Yamakita, N. Kamamichi, and Z.-W. Luo, "A novel gait generation for biped walking robots based on mechanical energy constraint," *IEEE Transactions on Robotics and Automation*, vol. 20, no. 3, pp. 565–573, 2004.

[11] Y. Ikemata, A. Sano, and H. Fujimoto, "A physical principle of gait generation and its stabilization derived from mechanism of fixed point," *Proceedings of the IEEE International Conference on Robotics and Automation*, pp. 836–841, 2006.

[12] D. G. Hobbelen and M. Wisse, "Limit cycle walking," *Humanoid Robots, Human-like Machines*, 2007.

[13] C. Azevedo, B. Espiau, B. Amblard, and C. Assaiante, "Bipedal locomotion: toward unified concepts in robotics and neuroscience," *Biological Cybernetics*, vol. 96, no. 2, pp. 209–228, 2007.

[14] L. C. Rome, L. Flynn, E. M. Goldman, and T. D. Yoo, "Generating electricity while walking with loads," *Science*, vol. 309, no. 5741, pp. 1725–1728, 2005.

[15] L. C. Rome, L. Flynn, and T. D. Yoo, "Biomechanics: Rubber bands reduce the cost of carrying loads," *Nature*, vol. 444, no. 7122, p. 1023, 2006.

[16] F. Asano and I. Tokuda, "Indirectly controlled limit cycle walking of combined rimless wheel based on entrainment to active wobbling motion," *Multibody System Dynamics*, vol. 34, no. 2, pp. 191–210, 2015.

[17] A. Pikovsky, M. Rosenblum, and J. Kurths, *Synchronization: a universal concept in nonlinear sciences*, vol. 12. Cambridge, U.K.: Cambridge university press, 2003.

[18] H. Nakao, "Phase reduction approach to synchronisation of nonlinear oscillators," *Contemporary Physics*, vol. 57, no. 2, pp. 188–214, 2016.

[19] M. Rosenblum and A. Pikovsky, "Numerical phase reduction beyond the first order approximation," *Chaos*, vol. 29, no. 1, p. 011105, 2019.

[20] B. Ermentrout, "Type i membranes, phase resetting curves, and synchrony," *Neural Computation*, vol. 8, no. 5, pp. 979–1001, 1996.

[21] P. Goel and B. Ermentrout, "Synchrony, stability, and firing patterns in pulse-coupled oscillators," *Physica D: Nonlinear Phenomena*, vol. 163, no. 3-4, pp. 191–216, 2002.

[22] B. Ermentrout, *Simulating, analyzing, and animating dynamical systems: a guide to XPPAUT for researchers and students*, vol. 14. Philadelphia, U.S.A.: Siam, 2002.

[23] W. Govaerts and B. Sautois, "Computation of the phase response curve: a direct numerical approach," *Neural Computation*, vol. 18, no. 4, pp. 817–847, 2006.

[24] P. L. Boyland, "Bifurcations of circle maps: Arnol'd tongues, bistability and rotation intervals," *Communications in Mathematical Physics*, vol. 106, no. 3, pp. 353–381, 1986.

[25] M. Matsugu, J. Duffin, and C.-S. Poon, "Entrainment, instability, quasi-periodicity, and chaos in a compound neural oscillator," *Journal of Computational Neuroscience*, vol. 5, no. 1, pp. 35–51, 1998.

[26] S. Aoi, T. Yamashita, and K. Tsuchiya, "Hysteresis in the gait transition of a quadruped investigated using simple body mechanical and oscillator network models," *Physical Review E*, vol. 83, no. 6, p. 061909, 2011.

[27] C. Grebogi, E. Ott, and J. A. Yorke, "Basin boundary metamorphoses: changes in accessible boundary orbits," *Physica D: Nonlinear Phenomena*, vol. 24, no. 1-3, pp. 243–262, 1987.

[28] A. Goswami, B. Thuilot, and B. Espiau, "Compass-like biped robot part i: Stability and bifurcation of passive gaits," tech. rep., INRIA, 1996.

[29] T. Harada, H. A. Tanaka, M. J. Hankins, and I. Z. Kiss, "Optimal waveform for the entrainment of a weakly forced oscillator," *Physical Review Letters*, vol. 105, no. 8, p. 088301, 2010.

[30] P. Buonocunto, A. Biondi, M. Pagani, M. Marinoni, and G. Buttazzo, "Arte: arduino real-time extension for programming multitasking applications," *Proceedings of the 31st Annual ACM Symposium on Applied Computing*, pp. 1724–1731, 2016.

[31] T. J. Allen, R. D. Quinn, R. J. Bachmann, and R. E. Ritzmann, "Abstracted biological principles applied with reduced actuation improve mobility of legged vehicles," *Proceedings of the IEEE/RSJ International Conference on Intelligent Robots and Systems*, vol. 2, pp. 1370–1375, 2003.

[32] A. Benini, A. Mancini, A. Marinelli, and S. Longhi, "A biased extended kalman filter for indoor localization of a mobile agent using low-cost imu and uwb wireless sensor network," *Proceedings of the 2012 IFAC Symposium on Robot Control*, vol. 45, no. 22, pp. 735–740, 2012.

[33] Y. Hanazawa, T. Hayashi, M. Yamakita, and F. Asano, "High-speed limit cycle walking for biped robots using active up-and-down motion control of wobbling mass," *Proceedings of the IEEE/RSJ International Conference on Intelligent Robots and Systems*, pp. 3649–3654, 2013.

[34] Y. Hanazawa, "Development of rimless wheel with controlled wobbling mass," *Proceedings of the IEEE/RSJ International Conference on Intelligent Robots and Systems*, pp. 4333–4339, 2018.

[35] F. Asano, T. Seino, I. Tokuda, and Y. Harata, "A novel locomotion robot that slides and rotates on slippery downhill," *Proceedings of the 2016 IEEE International Conference on Advanced Intelligent Mechatronics*, pp. 425–430, 2016.

[36] F. Guenther and F. Iida, "Energy-efficient monopod running with a large payload based on open-loop parallel elastic actuation," *IEEE Transactions on Robotics*, vol. 33, no. 1, pp. 102–113, 2017.

[37] F. Giardina and F. Iida, "Efficient and stable locomotion for impulse-actuated robots using strictly convex foot shapes," *IEEE Transactions on Robotics*, vol. 34, no. 3, pp. 674–685, 2018.

[38] H. A. Tanaka, "Optimal entrainment with smooth, pulse, and square signals in weakly forced nonlinear oscillators," *Physica D: Nonlinear Phenomena*, vol. 288, pp. 1–22, 2014.

[39] H. Adachi, N. Koyachi, T. Arai, A. Shimiza, and Y. Nogami, "Mechanism and control of a leg-wheel hybrid mobile robot," *Proceedings of the IEEE/RSJ International Conference on Intelligent Robots and Systems*, vol. 3, pp. 1792–1797, 1999.

[40] M. Takahaashi, K. Yoneda, and S. Hirose, "Rough terrain locomotion of a leg-wheel hybrid quadruped robot," *Proceedings of the IEEE International Conference on Robotics and Automation*, pp. 1090–1095, 2006.

[41] L. Bruzzone and G. Quaglia, "Locomotion systems for ground mobile robots in unstructured environments," *Mechanical Sciences*, vol. 3, no. 2, pp. 49–62, 2012.

[42] C. C. Phipps, B. E. Shores, and M. A. Minor, "Design and quasi-static locomotion analysis of the rolling disk biped hybrid robot," *IEEE Transactions on Robotics*, vol. 24, no. 6, pp. 1302–1314, 2008.

[43] Y. Kuramoto, *Chemical oscillations, waves, and turbulence*. Courier Corporation, 2003.

Publications

Journal Paper

[1] Longchuan Li, Isao Tokuda, Fumihiko Asano, "Nonlinear analysis of an indirectly controlled limit cycle walker," *Artificial Life and Robotics*, Vol. 23, pp. 508-514, 2018.

[2] Longchuan Li, Fumihiko Asano, Isao Tokuda, "High-speed sliding locomotion generation on slippery surface of an indirectly controlled robot with viscoelastic body," *The IEEE Robotics and Automation Letters (RA-L)* , accepted.

[3] Longchuan Li, Fumihiko Asano, Isao Tokuda, "Modeling, control, and analysis of indirectly-controlled semi-passive compass gait on slippery downhill," *Journal of Robotics and Mechatronics*, revising.

International Conference

[4] Longchuan Li, Fumihiko Asano and Isao Tokuda, "Nonlinear analysis of an indirectly controlled sliding locomotion robot," *Proceedings of the 2018 IEEE/RSJ International Conference on Intelligent Robots and Systems*, pp. 7454-7459, 2018.

[5] Longchuan Li, Isao Tokuda and Fumihiko Asano, "Optimal input waveform for an indirectly controlled limit cycle walker," *Proceedings of the 2018 IEEE/RSJ International Conference on Intelligent Robots and Systems*, pp. 4375-4380, 2018.

[6] Longchuan Li, Fumihiko Asano and Isao Tokuda, "High-speed and energy-efficient locomotion of a seed-like underactuated robot on level surface by utilizing asym-

metric wobbling effects," *Proceedings of the 2017 IEEE International Conference on Robotics and Biomimetics*, pp. 1014-1019, 2017.

[7] Longchuan Li, Isao Tokuda and Fumihiko Asano, "Nonlinear analysis of combined rimless wheel entrained to active wobbling motion," *Proceedings of the SWARM2017: The 2nd International Symposium on Swarm Behavior and Bio-inspired Robotics*, pp. 33-36, 2017.

[8] Longchuan Li, Masatsugu Nishihara, Omran Hindawi, Zhen Yang, Fumihiko Asano and Isao Tokuda, "Motion analysis of horizontal locomotion induced by active wobbling of a seed-like underactuated robot," *SICE Annuaul conference*, pp. 831-836, 2017.

[9] Masatsugu Nishihara, Longchuan Li, Omran Hindawi, Zhen Yang and Fumihiko Asano, "Motion analysis of crawling-like gait for underactuated locomotion robot utilizing 2-DOF wobbling effect on slippery level surface," *Proceedings of the SICE Annual Conference*, pp. 837-842, 2017.

Domestic Conference

[10] Longchuan Li, Cong Yan, Isao Tokuda and Fumihiko Asano "Experiment verification for an indirectly controlled limit cycle walker," *Proceedings of the 19th SICE Symposium on System Integration*, 1A4-05, pp. 157-161, 2018. (In Japanese)

[11] Longchuan Li, Fumihiko Asano, Isao Tokuda and Cong Yan "Indirectly controlled limit cycle walking on slippery downhill," *Proceedings of the 19th SICE Symposium on System Integration*, 1A4-05, pp. 162-165, 2018. (In Japanese)

[12] Longchuan Li and Fumihiko Asano, "Motion generation of a worm-like robot via asymmetric wobbling effect," *Joint conference of Hokuriku chapters of Electrical Society*, H-1, 2018.

[13] Longchuan Li, Kota Matsuura, Masatsugu Nishihara and Fumihiko Asano, "Motion generation and analysis of hybrid locomotion robot composed of rimless wheel and

seed-like robot on slippery downhill," *Proceedings of the 30th symposium on Robotics and Mechatronics*, pp. 1A1-M04(1)-1A1-M04(4), 2018. (In Japanese)

[14] Kota Matsuura, Longchuan Li, Masatsugu Nishihara, Seiya Kobayashi, Fumihiko Asano and Isao Tokuda, "Development of experimental combined rimless wheel with actively-controlled wobbling mass," *Proceedings of the 30th symposium on Robotics and Mechatronics*, pp. 1A1-M03(1)-1A1-M03(4), 2018. (In Japanese)

[15] Masatsugu Nishihara, Longchuan Li, Omran Hindawi, Zhen Yang and Fumihiko Asano, "Generation of forward motion on level surface for underactuated locomotion robot based on 2-DOF wobbling effect," *Proceedings of the 29th symposium on Robotics and Mechatronics*, pp. 2P2-H01(1)-2P2-H01(4), 2017. (In Japanese)